

The iPRES-W Coil:
Advancements in Wireless Technology for Magnetic Resonance Imaging

by

Jonathan David Cuthbertson

Graduate Program in Medical Physics
Duke University

Date: _____

Approved:

Allen W. Song

Trong-Kha Truong, Co-Supervisor

Dean Darnell, Co-Supervisor

Jeffrey Petrella

Lei Ren

Dissertation submitted in partial fulfillment
of the requirements for the degree of
Doctor of Philosophy in the Graduate Program in Medical Physics
in the Graduate School of
Duke University

2022

ABSTRACT

The iPRES-W Coil:
Advancements in Wireless Technology for Magnetic Resonance Imaging

by

Jonathan David Cuthbertson

Graduate Program in Medical Physics
Duke University

Date: _____

Approved:

Allen W. Song

Trong-Kha Truong, Co-Supervisor

Dean Darnell, Co-Supervisor

Jeffrey Petrella

Lei Ren

An abstract of a dissertation submitted in partial fulfillment
of the requirements for the degree of
Doctor of Philosophy in the Graduate Program in Medical Physics
in the Graduate School of
Duke University

2022

Copyright by
Jonathan David Cuthbertson
2022

Abstract

Purpose:

Integration of wireless data transfer in magnetic resonance imaging (MRI) would allow for the reduction of wired connections between the scanner subsystems and the control computers located outside the scanner room, which add to the cost and complexity of the scanner, reduce patient comfort, and impede the application of next-generation MRI technologies.

Methods:

In this dissertation, a novel RF coil design, termed the wireless integrated parallel reception, excitation, and shimming (iPRES-W) coil design, is further developed to remove some of these wired connections by offering a compact and easy-to-integrate MR-compatible wireless data transfer solution, which requires no scanner modifications or additional antenna systems in the bore. The iPRES-W coil design allows both a direct current (DC) and radio-frequency (RF) currents at the Larmor frequency and in a wireless communication band to flow on the same coil element to enable simultaneous MR image acquisition and wireless data transfer, which enables: wireless localized B_0 shimming; wireless peripheral system data transfer to augment imaging (e.g., respiratory tracking using a respiratory belt); wireless transfer of the scanner control signal to control on-coil electronics (e.g., Q-spoiling); and wireless power harvesting to power components of the iPRES-W system. To demonstrate the performance and utility

of the iPRES-W coil design in clinically relevant applications, this dissertation has four aims:

1. To develop an iPRES-W spine coil array to perform simultaneous MR imaging and wireless localized B_0 shimming of the spinal cord;
2. To develop a dual-stream iPRES-W head coil array for simultaneous MR imaging of the brain and multiple wireless data streams for control of separate peripheral systems, specifically, wireless localized B_0 shimming and respiratory tracking using a respiratory belt;
3. To further develop an integrated RF/wireless coil design for wireless transfer of the scanner trigger signal to perform the Q-spoiling required for MR image acquisition;
4. To design a wireless power harvesting system to convert the high-energy RF energy emitted by the scanner during the transmit cycle into a DC voltage to charge the batteries to power in-bore electronics and B_0 shim currents.

Results:

The results from this dissertation demonstrate that the iPRES-W coil modifications did not degrade the signal-to-noise ratio (SNR) when implemented onto different radio-frequency coil structures (e.g., a conventional RF coil element and novel adaptive imaging receive (AIRTM) coil element). Wireless localized B_0 shimming with the iPRES-W spine array and dual-stream iPRES-W head coil array substantially reduced the B_0 root-

mean-square-error (RMSE) by 70.1% and -41.2% in the spinal cord and frontal brain region, which corresponded to reduced DTI and EPI distortions, respectively. The wireless performance of the iPRES-W and iRFW coil elements measured in an anechoic chamber were minimally impacted by the introduction of a saline phantom representing tissue or during wireless Q-spoiling, respectively. The power harvesting experiments performed showed that the 4-channel power harvesting coil array could convert RF energy from the scanner into a DC voltage for recharging MR-compatible batteries for various scan parameters and imaging sequences.

Conclusions:

The iPRES-W and iRFW coil designs can be integrated into different coil structures and arrays to perform simultaneous imaging, wireless localized B_0 shimming, and wireless transfer of peripheral device data (e.g., respiratory tracking with a respiratory belt), with no SNR degradation, minimal change in wireless performance, and without scanner modifications or additional antenna systems within the scanner bore. Additionally, the power harvesting array can supply wireless power to charge MR-compatible batteries for various scan types and parameters.

Dedication

“If I have seen further, it is by standing on the shoulders of Giants”. To those who have held me up, this dissertation is dedicated you.

To my wife and friend, Katie, “what a privilege it is to love you, a great honor to hold you up”. My greatest accomplishment will always be marrying you.

To my parents, David and Elizabeth, for always singing the Ant Song, sending me post cards from Kenya, and being my biggest encouragement.

Contents

Abstract.....	iv
List of Figures.....	xii
List of Abbreviations.....	xv
Acknowledgments.....	xvii
1. An Introduction to MRI.....	1
1.1 Barriers to Technological Development in MRI.....	2
1.2 The Future is Wireless.....	5
1.2.1 Reduced Cost and Complexity.....	6
1.2.2 Increased Safety and Comfort.....	8
1.2.3 Enabling the Next Generation of MR Technologies.....	9
1.3 Implementing Wireless Data Transfer in MRI.....	11
1.3.1 The MR Receive Chain.....	11
1.3.2 Localized B ₀ Shimming.....	16
1.3.3 Peripheral Device Management.....	21
1.3.4 Control and Trigger Signals	23
1.3.5 On-coil Power Supply.....	24
1.4 Research Goals.....	28
2. RF Coil Design and Measurement Tools.....	31
2.1 Receive RF Coil Elements and Arrays.....	32
2.2 Evaluating the RF Coil Performance.....	36

2.2.1 Vector Network Analyzer.....	37
2.2.2 Image Quality and Signal-to-Noise-Ratio.....	39
2.2.3 Anechoic Chamber.....	42
3. Aim 1: The iPRES-W Spine Coil Array.....	44
3.1 Introduction.....	44
3.2 iPRES-W Coil Design Implementation.....	46
3.3 Battery Pack Design and Implementation.....	49
3.4 Experimental Setup and Tests.....	54
3.4.1 Temperature Measurements.....	54
3.4.2 SNR Measurements.....	55
3.4.3 DTI of the Cervical Spinal Cord with Wireless Localized Shimming..	55
3.4.4 iPRES-W Coil Wireless Antenna Performance.....	57
3.4.5 iPRES-W Coil Battery Power Consumption.....	59
3.5 Results.....	60
3.5.1 Temperature Measurements.....	60
3.5.2 SNR Measurements.....	62
3.5.3 DTI of the Cervical Spinal Cord with Wireless Localized Shimming..	63
3.5.4 iPRES-W Coil Wireless Antenna Performance.....	66
3.5.5 iPRES-W Coil Battery Power Consumption.....	68
3.6 Discussion.....	68

4. Aim 2: The Dual-Stream iPRES-W Head Coil Array.....	72
4.1 Introduction.....	72
4.2 RF Coil Modifications	74
4.2.1 iPRES Coil Design Implementation.....	74
4.2.2 iPRES-W Coil Design Implementation.....	78
4.3 Experimental Setup and Tests.....	80
4.3.1 SNR Measurements.....	80
4.3.2 MR Imaging with Wireless Shimming and Respiratory Tracking.....	81
4.3.3 Simulated B_0 Performance.....	82
4.4 Results.....	84
4.4.1 SNR Measurements.....	84
4.4.2 MR Imaging with Wireless Shimming and Respiratory Tracking.....	85
4.4.3 Simulated B_0 Performance.....	86
4.5 Discussion.....	87
5. Aim 3: The iRFW Coil Design and Wireless Q-Spoiling.....	89
5.1 Introduction.....	89
5.2 iRFW Coil Design Implementation.....	90
5.3 Experimental Setup and Tests.....	91
5.3.1 Wireless Q-Spoiling and SNR Measurements.....	91
5.3.2 Wireless Performance During Q-Spoiling.....	92
5.4 Results.....	93

5.4.1 Wireless Q-Spoiling and SNR Measurements.....	93
5.4.2 Wireless Performance During Q-Spoiling.....	94
5.5 Discussion.....	95
6. Aim 4: The 4-Channel Power Harvesting Coil Array.....	96
6.1 Introduction.....	96
6.2 Harvesting Coil Array: Construction and Implementation.....	97
6.3 Experimental Setup and Tests.....	99
6.3.1 Wireless Power Harvesting and Scan Parameters.....	99
6.3.2 Wireless Power Harvesting and MR Pulse Sequences.....	99
6.4 Results.....	100
6.4.1 Wireless Power Harvesting and Scan Parameters.....	100
6.4.2 Wireless Power Harvesting and MR Pulse Sequences.....	102
6.5 Discussion.....	103
7. Conclusion.....	105
References.....	107

List of Figures

Figure 1.1 CT versus MRI image of the brain.....	1
Figure 1.2: B_0 field strength and image SNR.....	3
Figure 1.3: Gradient field strength and image resolution.....	4
Figure 1.4: Conventional RF-receive coil arrays.....	6
Figure 1.5: Localized B_0 inhomogeneities and shim coils.....	7
Figure 1.6: Example RF receive arrays with increasing coil density.....	8
Figure 1.7: Novel next generation RF coil arrays.....	10
Figure 1.8: Block diagram for a conventional and wireless MR receive chain.....	12
Figure 1.9: Wireless data transfer via inductive coupling.....	13
Figure 1.10: Wireless data transfer via 60 GHz TX and RX antennas.....	14
Figure 1.11: Photo and schematic of iRFW coil array	15
Figure 1.12: Magnetic susceptibilities and B_0 inhomogeneities.....	17
Figure 1.13: B_0 inhomogeneities cause distortions and signal.....	17
Figure 1.14: Schematic and photo of multi-coil shim array.....	18
Figure 1.15: Diagram and photo of the iPRES head coil array.....	19
Figure 1.16: Combined RF/shim coil array and required cabling.....	21
Figure 1.17: Wireless power transfer system.....	24
Figure 1.18: Wireless power harvesting system.....	26
Figure 1.19: Harvested DC voltage pulses.....	28
Figure 2.1: Diagram for a conventional RF coil element.....	33

Figure 2.2: Critical overlap between adjacent RF coil elements.....	34
Figure 2.3: Photo of VNA.....	37
Figure 2.4: Various VNA setup configurations.....	38
Figure 2.5: Calibration diagram of VNA.....	39
Figure 2.6: Example image of water phantom and SNR masks.....	40
Figure 2.7: Example B_0 maps for evaluation of MRI compatibility.....	42
Figure 2.8: Anechoic chamber setup and calibration.....	43
Figure 3.1: Image and critical overlap graph of the AIR TM coil element.....	45
Figure 3.2: Photo and diagram of the 4-channel iPRES-W coil array.....	47
Figure 3.3: Schematic of an AIR TM coil modified into an iPRES-W coil element.....	47
Figure 3.4: Schematic of the wireless battery pack.....	50
Figure 3.5: Various PWM duty cycles.....	51
Figure 3.6: Frequency components for various PRM signals.....	52
Figure 3.7: DC current linearity graph for the wireless battery pack outputs.....	52
Figure 3.8: Temperature measurement setup and results.....	54
Figure 3.9: Anechoic chamber setup.....	58
Figure 3.10: SNR maps acquired in a water phantom.....	61
Figure 3.11: Anatomical images and SNR of the cervical spinal cord.....	61
Figure 3.12: Basis ΔB_0 maps for the iPRES-W coil array.....	63
Figure 3.13: ΔB_0 maps for each subject before and after shimming.....	64
Figure 3.14: DTI images for each subject before and after shimming.....	65

Figure 3.15: Wireless performance of the iPRES-W coil design.....	66
Figure 3.16: Battery consumption of the iPRES-W coil design.....	67
Figure 4.1: 48-channel head coil array.....	75
Figure 4.2: Schematic for an unmodified, iPRES, and iPRES-W coil element.....	75
Figure 4.3: Basis ΔB_0 maps for the iPRES-W head coil array.....	76
Figure 4.4: Simulation results for optimal iPRES coil elements.....	77
Figure 4.5: Schematic of the dual-stream iPRES-W head coil array.....	77
Figure 4.6: Setup diagram of the dual-stream iPRES-W head coil array.....	79
Figure 4.7: Wireless frequency bands for each iPRES-W coil element.....	80
Figure 4.8: SNR maps acquired in a water phantom.....	83
Figure 4.9: ΔB_0 maps and EPI images before and after shimming.....	84
Figure 4.10: The wirelessly transmitted respiratory signal.....	85
Figure 4.11: Simulated B_0 shim results using additional iPRES coil elements.....	86
Figure 5.1: The iRFW coil design for MR imaging and wireless Q-spoiling.....	90
Figure 5.2: Wired versus wirelessly transmitted scanner trigger signal.....	92
Figure 5.3 Image quality for wired versus wireless Q-spoiling.....	93
Figure 5.4: Wireless performance during Q-spoiling.....	94
Figure 6.1: The 4-channel harvesting coil array.....	98
Figure 6.2: DC voltage pulses applied for wireless battery charging.....	101
Figure 6.3: Harvested energy during various MR pulse sequences.....	102
Figure 6.4: Energy applied to the battery over a 10 minute duration.....	103

List of Abbreviations

ADC	Analog-to-digital converter
AIR	Adaptive image receive
AP	Access point
CT	Computerized tomography
DC	Direct current
DTI	Diffusion tensor imaging
DUT	Device under test
EPI	Echo-planar imaging
FA	Fractional anisotropy
fMRI	Functional magnetic resonance imaging
FOV	Field of view
FSE	Fast spin-echo
GPIO	General-purpose input/output
GRE	Gradient echo
iPRES	Integrated parallel reception, excitation, and shimming
iRFW	Integrated RF/wireless
LiPo	Lithium polymer
LNA	Low-noise amplifier
MD	Mean diffusivity
MRI	Magnetic resonance imaging

Op-amp	Operational amplifier
PCB	Printed circuit board
PIN	Positive-intrinsic-negative
PWM	Pulse-width-modulated
RF	Radio-frequency
RMSE	Root-mean-square error
ROI	Region of interest
SNR	Signal-to-noise ratio
SH	Spherical harmonic
TCP/IP	Transmission control protocol/internet protocol
TE	Echo time
TR	Repetition time
TSNR	Temporal signal-to-noise ratio
VNA	Vector network analyzer
WPH	Wireless power harvesting
WPT	Wireless power transfer

Acknowledgments

Thank you to my advisors, Trong-Kha and Dean, for your support, guidance, and encouragement for the last six years. Both of you have been excellent advisors and I truly appreciate the sacrifices you made to make me a better engineer and individual.

Thank you to my committee chair, Allen Song, and the entire BIAC community for providing an outstanding research lab to support my research. Thank you to my committee members, Jeffrey and Lei, for your time, support, and sacrifice. Finally, thank you to Fraser Robb for your kindness and investment in our lab and my research, none of this would have been possible without you.

1. An Introduction to MRI

Few scientific discoveries have revolutionized the field of medicine more than the ability to non-invasively see inside the human body using magnetic resonance imaging (MRI). The birth of MRI in 1973, pioneered by Paul Lauterbur, has led to countless breakthroughs for medical diagnostics, treatment monitoring, and research by providing three dimensional detailed anatomical images with excellent contrast between various soft tissues of the body. For example, in the brain, MRI is well suited to differentiate between gray and white matter (Fig. 1.1) and can be used to diagnose and monitor a variety of conditions such as tumors, damage caused by injury or stroke, cysts, infections, or other structural abnormalities in the tissue. In addition to structural imaging, functional magnetic resonance imaging (fMRI) can be used to determine brain activity or activation during different cognitive tests (e.g., reading or memory

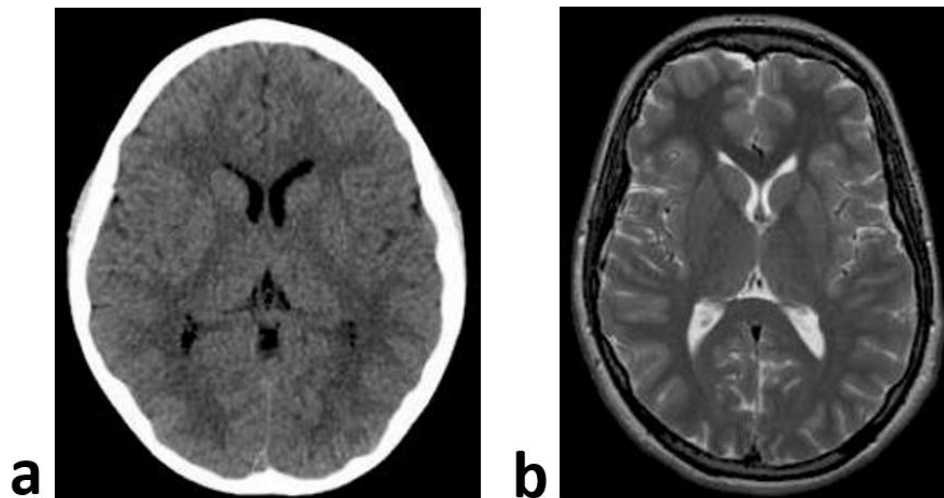


Figure 1.1: Difference between a CT scan (a) and MRI scan (b), which have excellent contrast between bone/tissue or gray/white matter in the brain, respectively.

recollection), which could potentially be used to diagnose or differentiate neurological disorders such as autism spectrum disorder (Dichter (2012)), attention deficit hyperactivity disorder (ADHD) (Paloyelis (2007)), depression (Boadie (2017)), or general anxiety disorder (Mochcovitch (2014)). Finally, since MRI does not rely on ionizing radiation, like X-ray or computerized tomography (CT), it is ideal for monitoring the treatment or progression of a disease when frequent imaging is required. As a result of its diverse imaging applications, MRI has become one of the most important advancements in medicine over the last 50 years and its impact will continue to grow due to its complex interdisciplinary framework, ever-expanding research avenues, and novel technological developments.

1.1 Barriers to Technological Development in MRI

Research focused on technological development in MRI, while diverse in application and approach, should always strive to provide better healthcare for individuals by either: improving image quality, reducing examination time, or increasing patient comfort and care. Since MRI is routinely implemented for clinical use, the human element cannot be overlooked. For example, ultra-high-resolution images to enable early cancer detection are unrealistic if the subject is expected to lay completely still during a two-hour scan. As such, research has pushed MRI scanner hardware to extreme engineering marvels, but human physiological limitations often restrict what

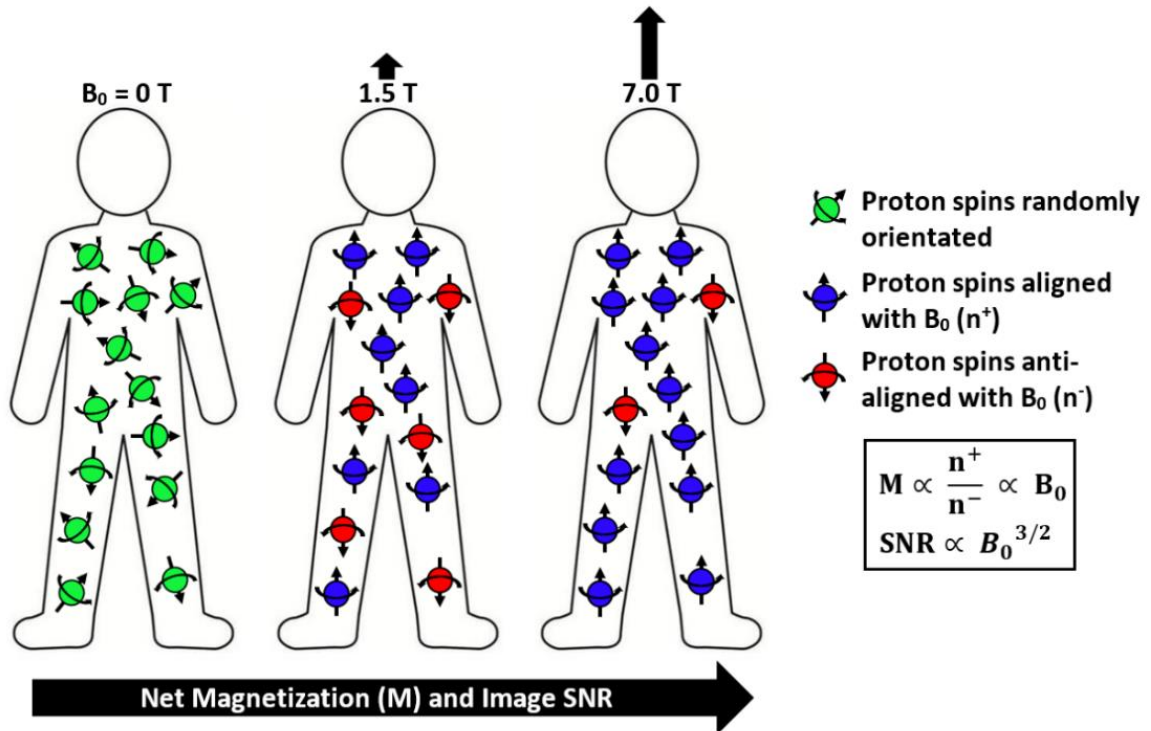


Figure 1.2: As B_0 increases, the protons in water are more likely to have their magnetic spin aligned with B_0 versus anti-aligned, which results in a greater net magnetization per voxel and subsequently improved image SNR.

can be practically implemented. For example, to improve the MR image quality, there has been a constant development of MR scanners with higher static magnetic field strengths (B_0) (Fig. 1.2) and stronger gradient coils (Fig. 1.3) to improve the image signal-to-noise ratio (SNR), spatial resolution (Moser (2017)), or to provide shorter examination times. While most clinical scanners today have a static field strength of 1.5 T, 3T, or 7T with a maximum gradient strength of ~50 mT/m, researchers have developed MRI scanners with an 11.7 T field strength (Beaujoin (2018)) or a 300 mT/m gradient strength. However, such scanners are unlikely to be widely implemented due to causing subject discomfort such as vertigo, nausea, dizziness, or peripheral nerve stimulation (PNS). In

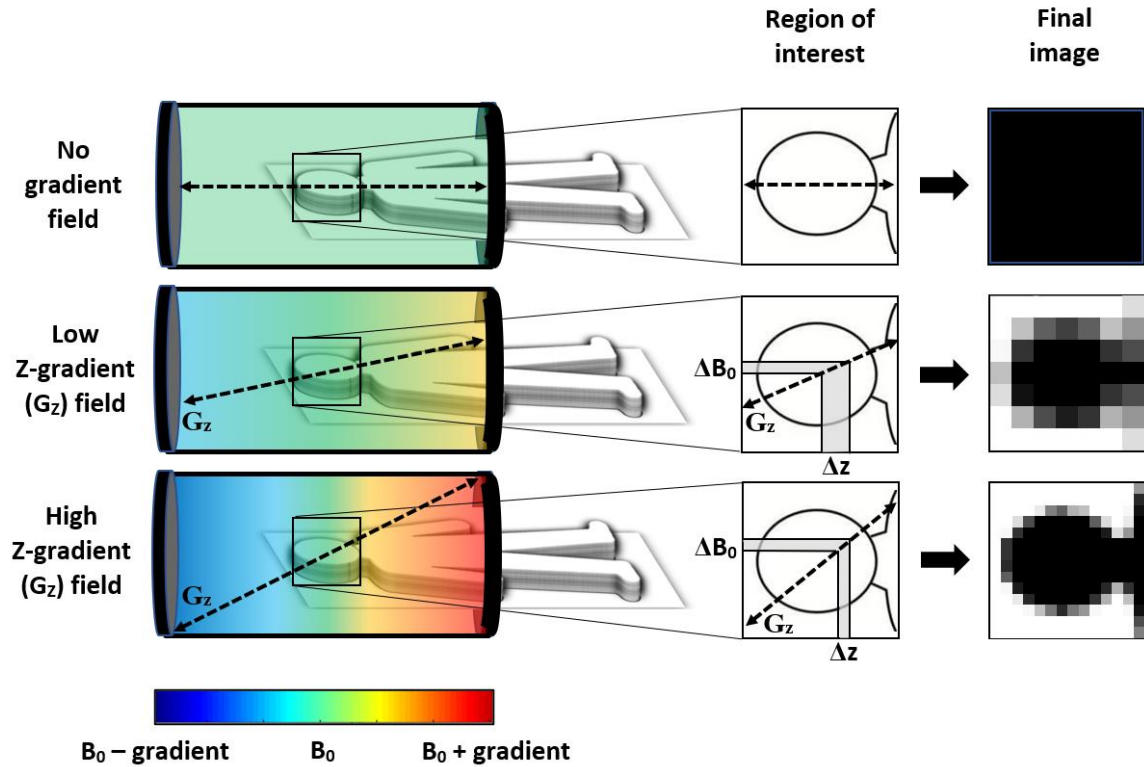


Figure 1.3: Stronger x, y, and z gradient fields (G_X , G_Y , and G_Z) result in improved image resolution (Δx , Δy , and Δz) due to greater spatial variation produced in the total magnetic field amplitude ($B_0 \pm \text{gradient}$).

addition to physiological limitations, other barriers can also arise, such as increased design cost and complexity, which can halt a previously advancing technological research trend. For example, MR scanners with stronger static field strengths also require specialized shielded MRI scanner rooms and heavy main magnets, which would require unfeasible infrastructure changes to existing scanner rooms and are too expensive for most hospitals to purchase. The 10.5 T scanner at the University of Minnesota requires ~600 tons of iron (e.g., the weight of four Statues of Liberty) to shield the \$13-million 110-ton magnet (Nowogrodzki (2018)), and because of this added complexity and cost, many hospitals will never upgrade their scanner despite the image

quality benefits provided. When these physiological or engineering barriers arise, new or parallel technologies emerge and fill the void to continue moving the field of MRI forward.

1.2 The Future is Wireless

One such emerging research trend that would improve image quality (e.g., by improving patient comfort and reducing motion artifacts), accessibility, and affordability for MRI is the transition from wired to wireless data transfer, the impact of which can be seen in numerous other areas of technology. For example, in telecommunications, before cell phones became widely available, telephone calling was restricted to a 10-foot radius inside the home by a springy, tangled cord, which limited mobility and prevented access for individuals in regions where establishing a wired infrastructure was not possible. The introduction of the cell phone (e.g., iPhone) addressed these limitations but also had profound and unexpected contributions for other areas such as information access, entrepreneurship, and global connectivity. Similarly, the transition to wireless data transfer in MRI would have countless impacts in the field of healthcare, the three most immediate being: 1) a reduction in the cost and complexity of the MRI scanner and peripheral systems, 2) an improvement in patient comfort and safety, and 3) the enabling of next-generation MR technologies such as flexible, lightweight, and wearable radio-frequency (RF) receive coil arrays or other MR-compatible devices.

1.2.1 Reduced Cost and Complexity

The first benefit of enabling wireless data transfer in MRI is a reduced system cost and complexity. MRI scanners in both a clinical and research setting require data to be transferred between the scanner subsystems, such as the RF (Fig. 1.4) or shim coils (Fig. 1.5); or peripheral systems, such as a respiratory belt for respiratory monitoring or a projector to provide a stimulus for fMRI, and the control computers located outside the scanner room. Currently, this data transfer requires a complex network of wired connections, which must be carefully routed inside the scanner room and requires additional electronics such as RF filters, baluns, and cable traps to maintain data integrity and MR image quality. The RF receive coil arrays used for image acquisition

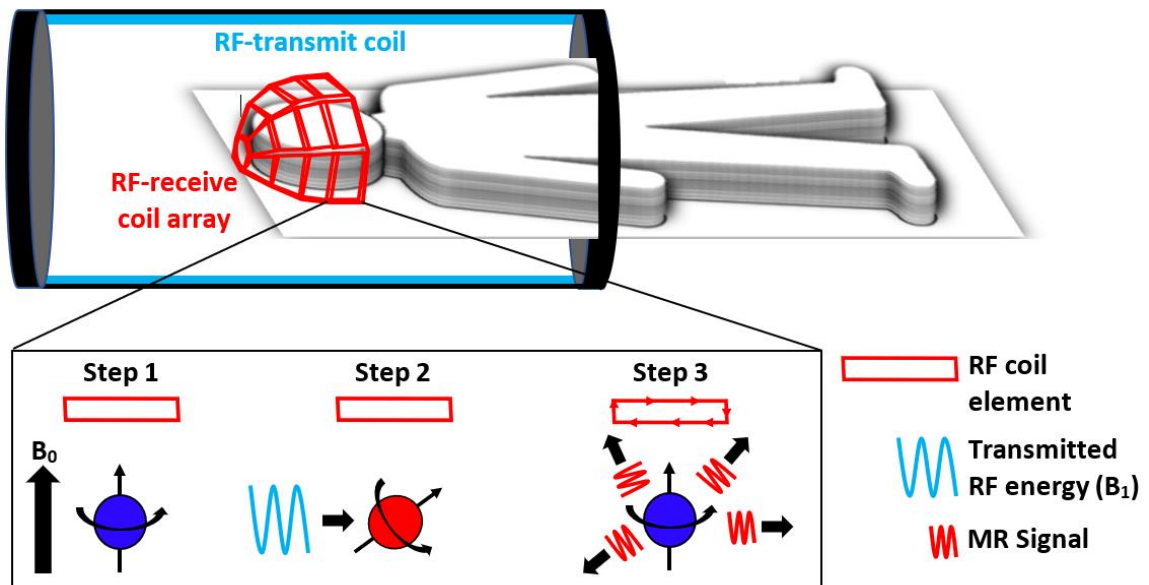


Figure 1.4: Traditional RF-receive coil arrays consist of many coil elements arranged inside a rigid frame, which closely surround the subject's anatomy. During image acquisition, protons are excited by the B_1 field from the RF-transmit coil (light blue) and are tipped out of alignment with B_0 . As the protons relax, they emit energy (red) which is collected by the RF coil elements and used to generate the image.

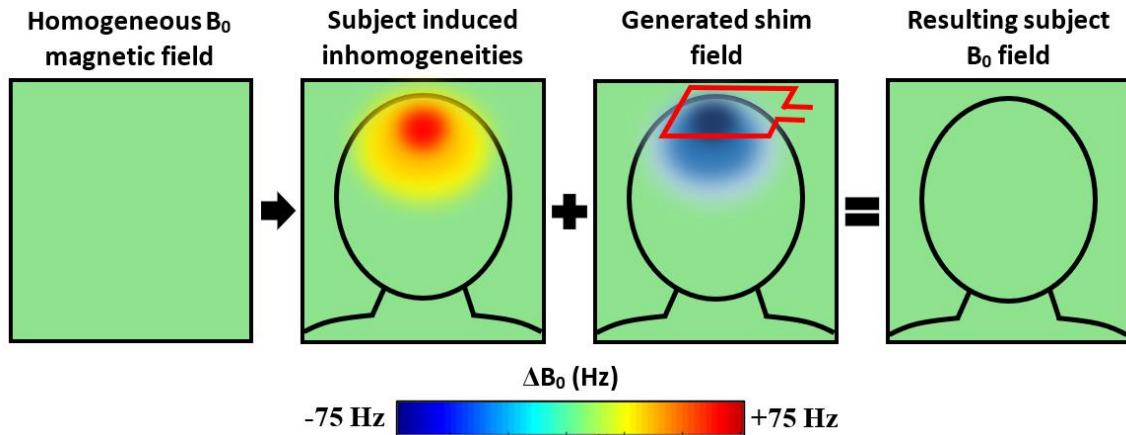


Figure 1.5: Unwanted inhomogeneities (red) in the main magnetic B_0 field are corrected for by applying a secondary shim magnetic field (blue) of equal and opposite polarity, which is generated by the shim coils (red loop).

integrity and MR image quality. The RF receive coil arrays used for image acquisition are also becoming more complex with a larger number of coil elements to provide better image quality and shorter examination times through parallel imaging (Sodickson (1997) and Pruessmann (1999)) (Fig. 1.6). As such, each coil element of the high-density coil arrays requires 1) an RF coaxial cable to transfer the acquired RF signal outside the scanner room for image reconstruction and 2) a direct current (DC) cable to provide power to the onboard electronics (e.g., preamplifiers and detuning PIN diodes). These numerous cables, and the previously mentioned additional electronics required for each cable, drastically increase the system's cost and complexity.

The same concerns also apply to other MRI subsystems such as: localized B_0 shimming (e.g., multi-coil (Juchem (2011a) and Juchem (2011b)) and integrated parallel reception, excitation, and shimming (iPRES) (Truong (2014)) coil arrays), peripheral devices (e.g., respiratory and cardiac monitoring), and a wide array of other applications



Figure 1.6: Photos of RF receive head coil arrays with increased coil density (i.e., more coil elements placed close to the imaging field of view)¹.

(e.g., NMR probes and fMRI stimuli). Alternatively, replacing the complex wired cabling network with a wireless network interface could lead to RF coil arrays and in-bore peripheral systems that are more cost-effective and easier to setup and install.

1.2.2 Increased Safety and Comfort

The second benefit wireless data transfer in MRI would provide is increased comfort and safety for the patient. A traditional clinical or research MRI scanner bore has an inner diameter between 60 – 70 cm (23.6 – 27.6 in) and provides limited room to accommodate the subject, RF-receive coil array, and any additional in-bore electronics (e.g., physiological monitoring devices, shim coil arrays, etc.). This tight space often means that the wires and cables for the RF receive coil array and peripheral devices must be placed across or next to the subject's body, which can cause claustrophobia or anxiety in certain individuals and can cause burns or local tissue heating due to currents

¹ Image Credit: <https://www.umass.edu/ials/hmrc>

induced on the cables during the RF-transmit phase or fast gradient switching (Armenean (2004)), respectively. A report in 2019 by the US Food and Drug Administration (FDA) provided a 10-year overview of the adverse events for MR systems and found that of the 1568 reports, thermal injuries were the most common, making up 906 of the reports (59%) (Delfino (2019)). Baluns, RF cable traps, and filters can reduce this risk of thermal injury but add to the weight and bulkiness of the RF-receive coil arrays, making them potentially intimidating and ill-fitting for patients and difficult to lift and position for the technologists. The transition to wireless data transfer would greatly reduce the risk of thermal injury, free up additional space inside the scanner bore, and reduce physical strain on the clinical technologists during setup.

1.2.3 Enabling the Next Generation of MR Technologies

The third benefit of wireless data transfer in MRI is its ability to enable the next generation of MR technologies. The use of wires and RF coaxial cables is one of the major bottlenecks to developing ultra-lightweight (McGee (2018) (Fig. 1.7a)), flexible (Corea (2016) (Fig. 1.7b), Frass-Kriegel (2018), and Mehmman (2019)), or wearable RF-receive coil arrays (Zhang (2018) (Fig. 1.7c) and Cogswell (2021)) as the cable, assemblies, required baluns, filters, and cable traps are the heaviest and most rigid components, which reduce the effectiveness and durability of these novel RF coil designs. Additionally, wireless data transfer within the MR scanner bore would enable the

integration of multiple physiological monitoring devices into these novel RF coil arrays. For example, the wearable MR glove coil array shown in Figure 1.7c could be equipped with a heart rate monitor, blood pressure monitor, or oximeter, following a similar integrated trend of the modern smartwatch. This integration would not be possible using traditional wired connections without the concern of signal cross talk and coupling between the closely adjacent cables, which could decrease image quality or data integrity.

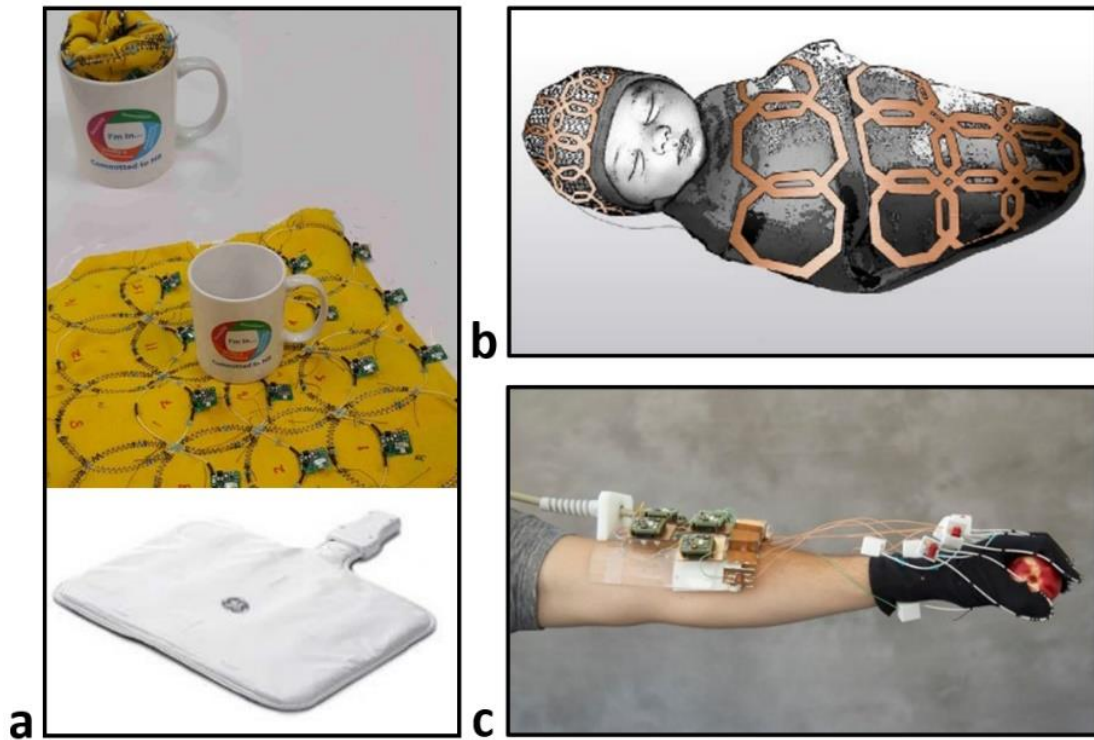


Figure 1.7: Images showing the flexible and ultra-lightweight Adaptive Image Receive (AIRTM) coil technology (a), flexible screen-printed infant blanket (b), and wearable MR glove coil array for imaging of the hand (c).

1.3 Implementing Wireless Data Transfer in MRI

The transition to wireless data transfer in MRI requires five MR scanner subsystems to undergo significant changes, specifically, 1) MR receive signal chain, 2) B_0 shimming, 3) control signals for on-coil triggering (e.g., Q-spoiling), 4) peripheral device interface, and 5) on-coil power supply and management. The following sections will introduce these subsystems in more detail and previous research done to implement wireless data transfer for each respective subsystem. The final section will introduce the goals and significance of this dissertation work to further develop an integrated, cost effective, and easy-to-implement wireless antenna system for MRI.

1.3.1 The MR Receive Chain

The first subsystem, the MR receive chain, is responsible for conditioning and processing the acquired MR signal for image reconstruction and display (Fig. 1.8). In a traditional wired setup (Fig. 1.8a), the MR signal is first acquired by the RF receive coil array (Fig. 1.8, red) before being transferred to the gain amplifiers (Fig. 1.8, green), which has a wide input voltage range and adjustable gains to accommodate different MR scan types. For example, the incoming MR signal amplitude can have a dynamic range of ~90 dB and up to ~120 dB for high-resolution 3D image acquisitions (Behin (2005)). The adjustable gains ensure that the MR signal is at the correct voltage level before it is digitized by the analog-to-digital converter (ADC) (Fig. 1.8, dark blue). Finally, the digitized MR signal passes through a filter to reduce noise (Fig. 1.8, purple)

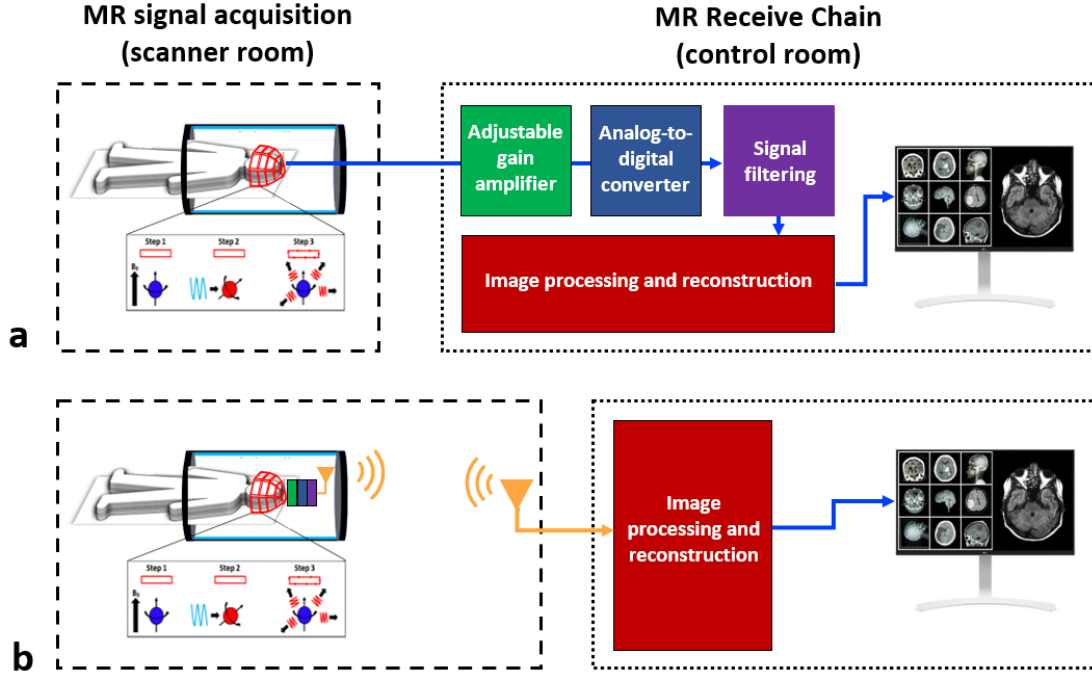


Figure 1.8: Block diagram of the MR signal acquisition and MR receive chain for a traditional wired (a) versus wireless (b) setup, which consists of the adjustable gain amplifiers (green), ADC (blue), and filters (purple).

before being processed and reconstructed (Fig. 1.8, dark red) for display. To enable wireless data transfer of the MR signal, the MR signal conditioning, digitization, and filtering circuits must be moved from the control room and integrated onto the RF coil array (Fig. 1.8b). Additionally, transmit and receive antennas are integrated into the scanner bore and along the scanner room wall, respectively, (Fig. 1.8, orange) to wirelessly transfer the digitized MR signal to the adjacent control room for image processing and reconstruction. Previous work has demonstrated the feasibility of wirelessly transmitting the MR signal during image acquisition using various wireless protocols (Aggarwal (2017), Vassos (2019), and Ko (2019)); however, these proof-of-concept implementations have focused primarily on the wireless antenna systems and

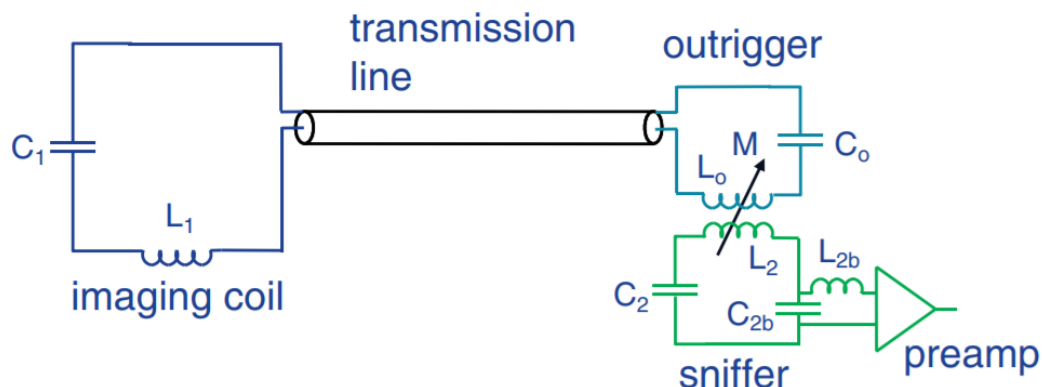


Figure 1.9: Circuit diagram for wireless data transfer via inductively coupled outrigger and sniffer coils².

achievable data rates and require further development before a digital RF receive coil array is able to be interfaced with a wireless transmit/receive antenna system.

One such system eliminates the RF cabling between the RF coil array and scanner by wirelessly transferring the MR signal data via a set of inductively coupled coils (Bulumulla (2015)). The MR signal data acquired by each RF coil element is transferred from an outrigger coil to a secondary “sniffer” coil placed within close proximity (Fig. 1.9), before being sent to the console room for image reconstruction. However, the use of inductive coupling for MR signal data is not optimal as SNR can be decreased for even slight misalignments between the two coils. Additionally, the complexity and cost of this design is proportional to the number of RF coil elements and peripheral devices since each independent data stream would require a separate outrigger and sniffer coil, which would significantly increase setup time, slow down the clinical workflow, and take up valuable space within the scanner bore.

² Image credit: Bulumulla (2015)

A second previously proposed wireless system utilizes a high-frequency (60 GHz) transmit (TX) and receive (RX) antenna for wireless transmission of the acquired MR signal (Fig. 1.10) (Aggarwal (2017)). For this design, the acquired MR signal is first digitized via an on-coil ADC and then transmitted wirelessly between the TX and RX antennas. The data received by the RX antenna is then sent out of the scanner bore and to the console room for image reconstruction via a plastic optical fiber (POF). One advantage of using a 60-GHz setup is higher throughput rates (200 Mb/s – 2.5 Gb/s) compared to conventional WiFi data rates at 2.4 GHz 802.11 (b/g/n) (1 Mb/s – 72.2 Mb/s), which is beneficial for the large quantity of data obtained during MR image acquisition. However, limitations of using such a high-frequency signal are that the wireless data rate and quality are highly dependent on the TX and RX antenna alignment and

Figure 1.10: Block diagram showing the 60 GHz wireless antenna setup inside the MRI room at a distance of 25 cm, 50 cm, and 65 cm³.

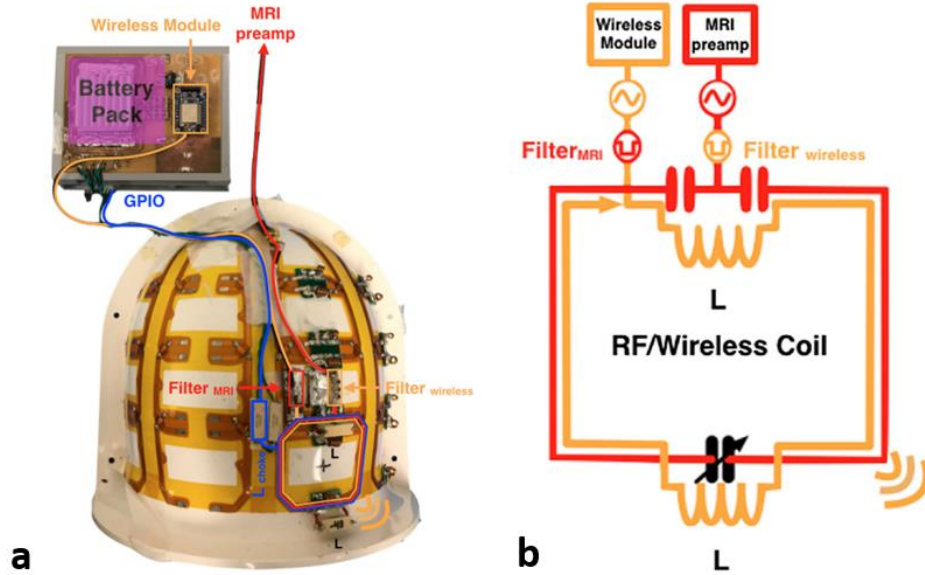


Figure 1.11: Image of the iRFW coil array (a) where an RF coil element is modified to allow an RF current at the Larmor frequency (red) and an RF current in a wireless communication band (orange) to flow on the coil for MR imaging and wireless data transfer, respectively (b).

separation, due to high antenna directivity (i.e., the amount of energy concentrated in a single direction relative to an isotropic radiator) and signal path loss (i.e., the amount of signal attenuation as it travels through air). In addition, this complex setup adds a significant amount of hardware inside and outside the scanner bore and does not easily allow for bidirectional wireless data transfer (i.e., data sent from the scanner to console room and vice versa) to support other peripheral devices. The high data rate may also be less of an advantage for this design with the release of more recent WiFi protocols such as 2.4 GHz 802.11ac (866 Mb/s) or 5 GHz 802.11ax (2.4 Gb/s).

To address these limitations, an innovative RF coil design, termed the integrated RF/wireless (iRFW) coil design, was developed to perform wireless data transfer using the existing coil elements of an RF coil array (Darnell (2019)) (Fig. 1.11). As such, this

design enables simultaneous MR image acquisition and wireless data transfer without requiring any additional antenna systems inside the scanner bore. As a first application, the iRFW coil design was used to wirelessly control a localized B_0 shim current.

However, this design can also be used to wirelessly transfer other data types (e.g., MR signals, physiological monitoring, etc.) and since it utilizes only a single pre-existing RF coil element, multiple iRFW coil elements can be implemented per RF coil array to enable multiple independent data streams.

1.3.2 B_0 Shimming

The second subsystem is responsible for providing the necessary B_0 shimming during image acquisition. Regardless of the B_0 uniformity achieved within the scanner bore during installation, distortions of the magnetic field lines can occur with the introduction of outside materials with different magnetic susceptibilities (Fig. 1.12). Susceptibility differences at air/tissue interfaces within the human body (e.g., frontal sinus cavity and auditory canals near the brain) lead to local B_0 inhomogeneities, which if left uncorrected, can produce geometric distortions (Fig. 1.13a) and signal loss (Fig. 1.13b) in MR images. To correct for these B_0 inhomogeneities, most clinical and research scanners come pre-installed with spherical harmonic (SH) shim coils (Golay (1958)), which are built into the scanner bore and produce either static (Kim (2002)) or dynamic (e.g., for multislice image acquisition) corrective fields (de Graaf (2003)). In theory, any localized B_0 inhomogeneity expanded into an infinite series of SH terms can be corrected

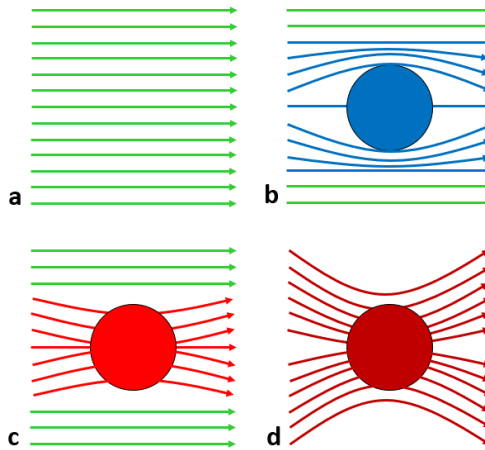


Figure 1.12: Materials with different magnetic susceptibilities distort the uniform B_0 field (a), which cause inhomogeneities. Diamagnetic materials (b) repel the magnetic lines, while paramagnetic (c) and ferromagnetic (d) materials attract the field lines.

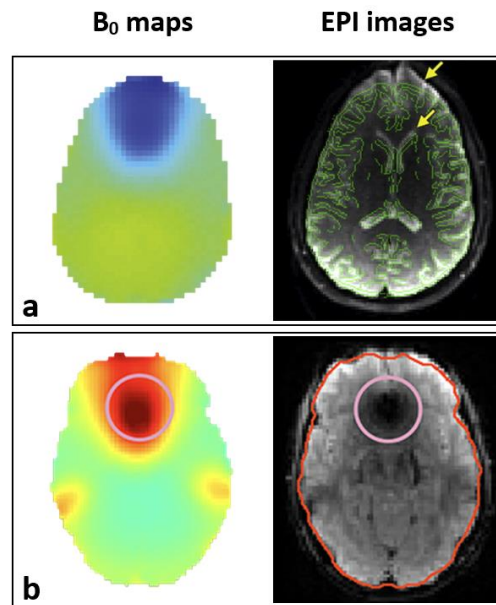


Figure 1.13: In regions where the change in B_0 is large due to localized B_0 inhomogeneities and magnetic susceptibility differences, there are resulting geometric distortions⁴ (a) (yellow arrows), and signal loss⁵ (b) (pink circle) in the acquired echo-planar images (EPI).

⁴ Image credit: Truong (2014)

⁵ Image credit: Willey (2021)

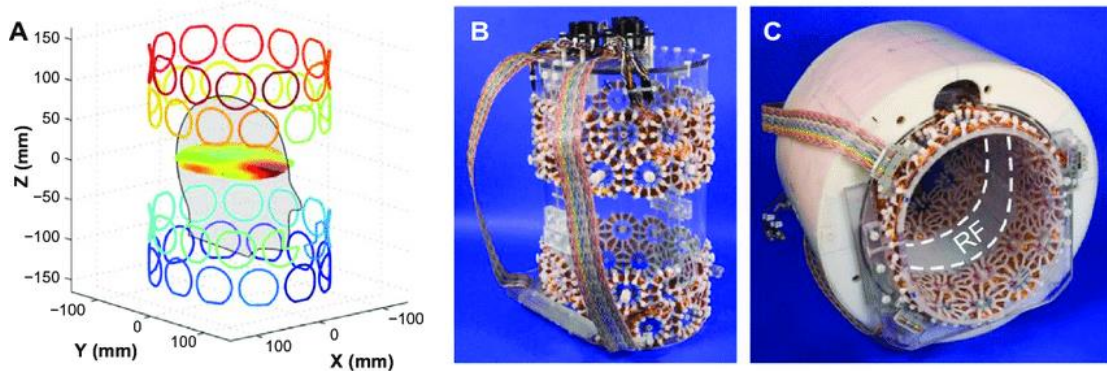


Figure 1.14: Schematic (A) and images (B and C) of a 48-loop multi-coil shim array for the brain⁶.

for; however, engineering constraints, cost, and system complexity limit most scanners to second or third order terms, which cannot effectively shim strong localized B_0 inhomogeneities (e.g., prefrontal cortex) or large regions of interest (ROI) (e.g., abdomen). In addition, the SH shim coils reduce the overall diameter of the bore and require expensive shim current amplifiers located outside the scanner room, which require wired connections to the shim coils and add to the system cost and complexity (Stockmann (2016)).

To address these limitations, single coil and multi-coil (MC) shimming attempts to provide improved field homogeneity by using small shim coils placed close to the body to generate local magnetic fields via independently controlled DC currents. The single coil shimming method targets a specific region of the body (e.g., cervical spine) and provides a general corrective offset (Biber (2021)), while MC shimming utilizes an array of coils (Fig. 1.14) to target multiple localized B_0 inhomogeneities over a larger ROI

⁶ Image credit: Juchem (2011b)

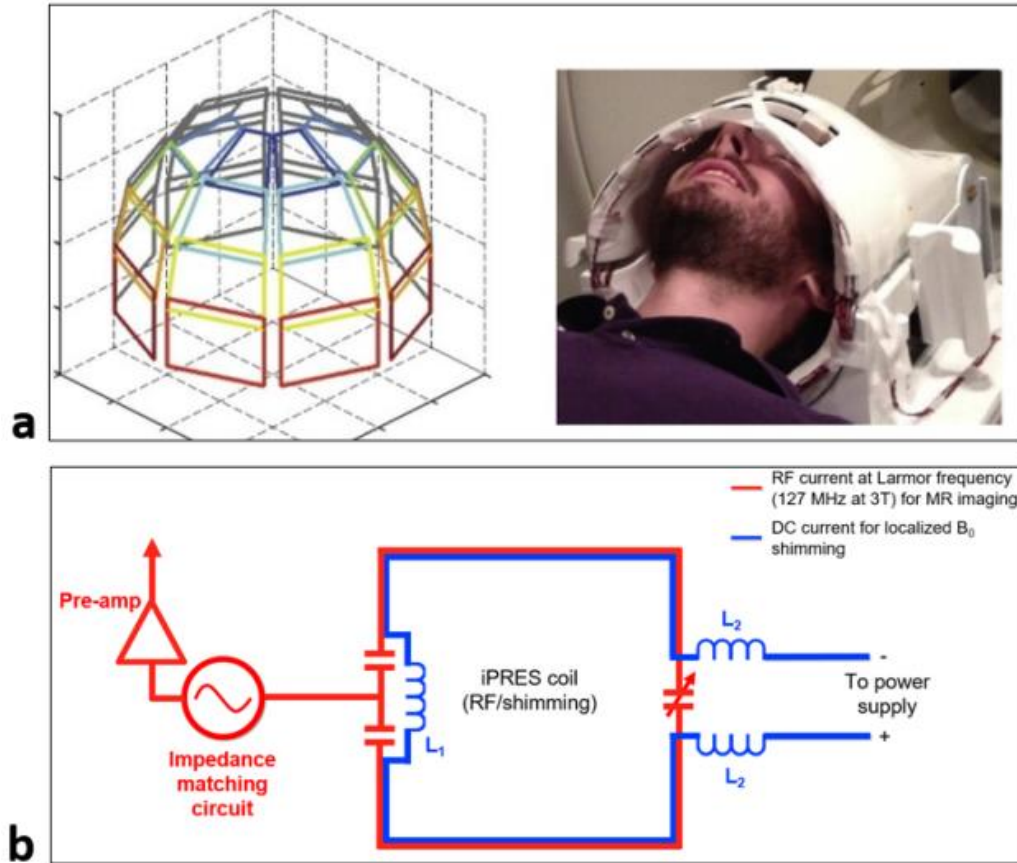


Figure 1.15: Diagram and photo of the 32-channel iPRES head coil array (a)⁷. The schematic (b) shows how an RF coil element (red) is modified into an iPRES coil element by adding inductive chokes (L_2), DC wires, a DC power supply, and a bypass inductor (L_1) (blue) to allow a DC current to flow along the loop.

(e.g., brain and abdomen) and has shown improved shim results compared to third-order SH shimming (Juchem (2012), Juchem (2015), and Aghaeifar (2018)). In addition, MC shim arrays allow for 1) faster current switching (i.e., shorter scan times) due to their small size and low inductance, 2) power supplies that have lower voltage and cost since there is less resistive loss, and 3) high efficiency B_0 shimming since the coils are placed close to the subject (Stockmann (2015)). Implementing MC shimming, however, can be

⁷ Image credit: Truong (2014)

difficult when there are multiple shim coils on a single array since the shim coils compete with the RF coil array elements for space within the bore, which can potentially result in a decrease in image SNR, transmit RF efficiency, or shimming performance.

The integrated parallel reception, excitation, and shimming (iPRES) coil design solves the integration limitation of MC shimming by combining the shim and RF coil arrays onto a single unified system (Han (2013)). In this design, both an RF and DC current flow on the same coil element to enable simultaneous MR image acquisition and localized B_0 shimming, respectively (Fig. 1.15), with no degradation in SNR. This iPRES coil design has been used to effectively shim localized B_0 inhomogeneities and improve the image quality in the human brain (Truong (2014), Stockmann (2016), Willey (2021), and Stockmann (2018)), abdomen (Darnell (2017) and Darnell (2018)), breast (Ma (2018)), and spinal cord (Topfer (2018a), Rios (2019), and Topfer (2019)). Like other shimming methods (e.g., SH and MC shimming), iPRES or integrated RF/shim coil arrays require numerous wired connections to power supplies located outside the scanner room and additional electronics such as cable traps, baluns, and filters, to maintain image quality.

To eliminate the wired connections required for shimming, the iPRES coil design was previously combined with the iRFW coil design (section 1.3.1), yielding the wireless iPRES (iPRES-W) coil design, which allows an RF current at the Larmor frequency, RF currents in a wireless communication band, and a DC current to flow on the same coil element, thereby enabling simultaneous MR image acquisition and wireless localized B_0 shimming (Darnell (2019)). Specifically, the iPRES-W coil design allows data to be

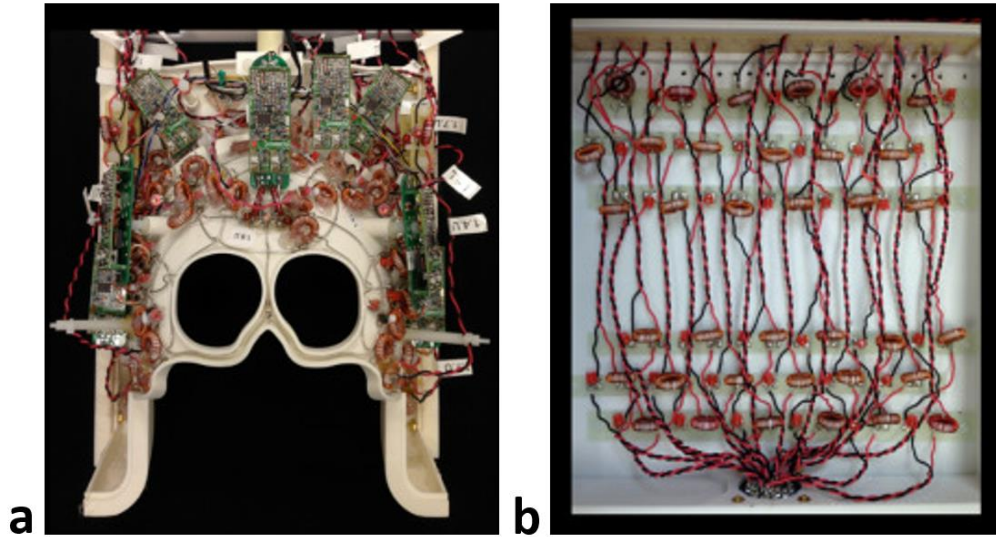


Figure 1.16: Photo of a combined RF/shim array (a) and required network of cable traps, baluns, and filters (b)⁸.

wirelessly transmitted between a computer in the console room and the coil element to adjust the DC current for shimming, which is supplied from a battery within the scanner bore. Previously, only proof-of-concept experiments were conducted with a single iPRES-W coil to demonstrate its ability to wirelessly shim localized B_0 inhomogeneities in a phantom.

1.3.3 Peripheral Device Management

The third MRI subsystem encompasses the numerous peripheral devices added within the scanner bore during image acquisition, which include 1) physiological monitoring devices such as a heart rate monitor, oximeter, or respiratory belt to ensure

⁸ Image credit: Stockmann (2016)

patient safety or provide cardiac/respiratory gated MR image acquisition (Dietrich (2022)), 2) probes or sensors to provide system feedback and aid with image acquisition and reconstruction, such as NMR probes for continuous magnetic field monitoring (Dietrich (2016)), or 3) monitoring devices for motion tracking, such as cameras for optical tracking and real-time motion correction (Zaitsev (2006) and Schulz (2012)). As the number of devices added within the MRI scanner bore increases, so does the number of cables, which can increase the risk of thermal injury to the subject and reduce the SNR (section 1.2.2). To enable wireless data transfer for peripheral device data, previous work has primarily focused on a specific wireless application or device, rather than a wireless system for multiple independent devices and data streams. For example, wireless motion correction in the brain using a wireless RF-triggered acquisition device (WRAD) has been previously demonstrated; however, the system simply used an external 2.4 GHz transmitter within the scanner bore and receiver along the scanner room wall to provide the wireless data link (Niekerk (2022)). As such, additional peripheral devices would need a separate external wireless transmitter, which would take up valuable space within the scanner bore and result in possible signal cross talk and interference depending on the antenna positions within the scanner bore. Similarly, the previously proposed wireless systems for MRI (section 1.3.1) cannot easily provide a wireless link for multiple applications as each device and independent data stream would require either an additional high frequency Tx/Rx antenna setup (Aggarwal (2017)) or

inductively coupled outrigger/sniffer coil set (Bulumulla (2015)), which would increase the amount of hardware required within the scanner bore.

1.3.4 Control Signals and Q-Spoiling

To fully remove the cables in MRI, the fourth subsystem that must be made wireless is the MR control and trigger signal system. The conventional connectors and cable assemblies between the RF coil array and scanner are commonly bidirectional and responsible for 1) transferring the received MR signal to the control room for image construction (section 1.3.1) and 2) receiving signals from the scanner control unit to the coil array, which are distributed to the coil electronics for various functions such as clock synchronization and triggering. For example, one of these functions is active detuning or Q-spoiling, where a DC voltage is turned on for the duration of each of the scanner transmit cycles in order to detune the coil element, thereby providing RF protection to the MRI preamplifier. After each transmit cycle, the DC voltage must be quickly turned off so that the coil element is ready to receive the MR signal from the subject. To enable wireless transmission of the control signals for Q-spoiling, previous bench-top measurements of multiple antenna designs used to transmit the trigger signals suggest that a reflected coil loop could provide the best wireless connection for Q-spoiling (Lu (2018)). Additionally, the ability to perform wireless Q-spoiling has been previously demonstrated using trigger signals transmitted via a 418 MHz antenna during MR image acquisition (Lu (2017)). However, both of these wireless Q-spoiling

implementations would require additional antenna systems within the scanner bore and modifications to be made to the scanner, increasing the cost and complexity.

1.3.5 On-coil Power Supply

In addition to data transmission, the conventional wired connections in an MRI scanner provide the required electrical power to the RF coil array (e.g., for preamplification and Q-spoiling), shim coils (e.g., SH, MC, or iPRES), and peripheral systems such as on-patient physiological monitoring devices (e.g., respiratory belt and cardiac monitor) and in-bore/on-coil monitoring or feedback devices (e.g., NMR field

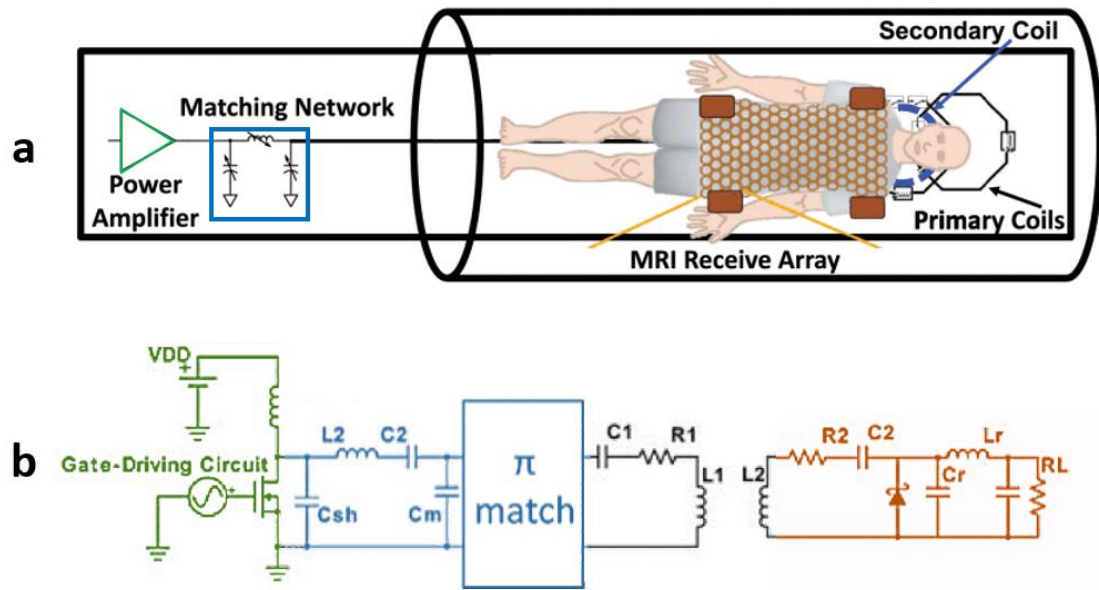


Figure 1.17: The wireless power transfer (WPT) system integrated into the MRI scanner bore (a) and circuit diagram showing power amplifier (green), matching network (blue), primary (L_1) and secondary (L_2) inductively coupled coils, and signal rectifier/filter (orange)⁹.

⁹ Image credit: Byron (2019a)

probes and fMRI stimuli). To provide wireless power for these systems, the use of MR-compatible lithium polymer (LiPo) batteries has been an attractive solution for applications such as: localized B_0 shimming (Cuthbertson (2019) and Cuthbertson (2020)), physiological monitoring (Chen (2017), Wiley (2020), and Cuthbertson (2020)), and Q-spoiling (Lu (2017) and Cuthbertson (2021)) as they are relatively inexpensive (e.g., \$15 - \$45), thin (e.g., 5 – 5.8 mm), and lightweight (e.g., 11 – 108 g) while providing a large energy storage capacity (e.g., 600 – 6000 mAH) (PowerStream, Orem, UT). However, battery charge time or regularly swapping in new batteries can limit patient scan time and interrupt the clinical workflow. Additionally, high-power consuming applications (e.g., a 48-channel RF coil array) would require a significant increase in the number of in-bore batteries, which would add additional weight and limit the flexibility of a device, take up valuable space within the scanner bore, and increase the risk of image artifacts due to eddy currents induced on the outer aluminum foil case of the battery. To address these limitations, two wireless power delivery methods have been previously investigated, specifically, wireless power transfer (WPT) and wireless power harvesting (WPH).

WPT employs a single (Byron (2017)) or multiple (Byron (2018) and Byron (2019a)) WPT “primary” coils embedded in the MRI patient table and an inductively coupled “secondary” coil placed nearby and connected to the device being powered. Specifically, RF power (e.g., at 10 MHz) is generated by a power amplifier (Fig. 1.17, green), located outside the scanner room, and transferred between the inductively

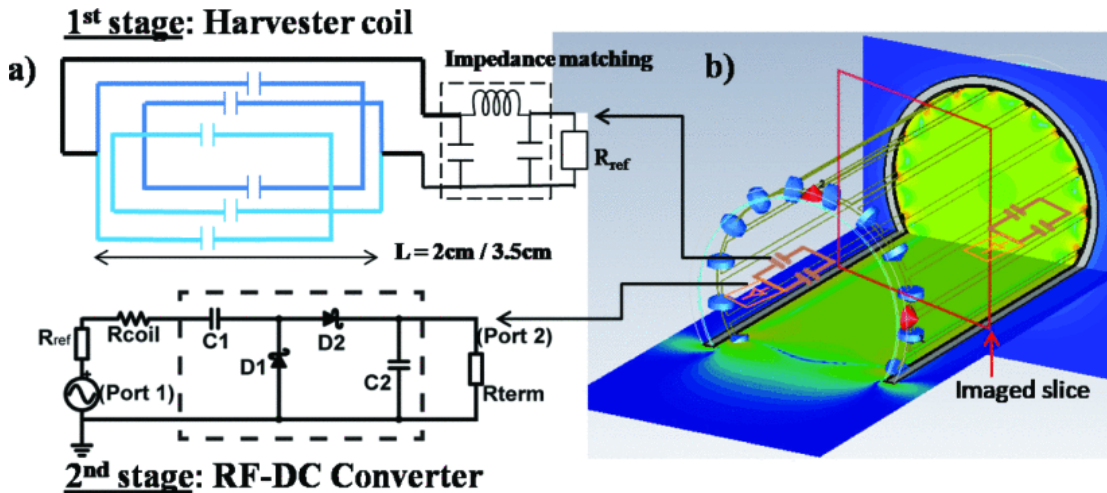


Figure 1.18: The 1st and 2nd stage of the WPH design consisting of the harvester coil and matching circuit and the AC-DC converter, respectively (a). The harvesting coil was placed within the scanner bore and near the RF coil array and imaged phantom (b)¹⁰.

coupled primary and secondary coils (Fig. 1.17, L_1 and L_2) before being rectified (Fig. 1.17, orange) and applied to the wireless device (Fig. 1.17, MRI receive array). While this method is capable of providing a significant amount of wireless power ($\sim 13\text{W}$), a major limitation is that it cannot be easily integrated into the scanner room or bore, as 1) wired connections must be established between the power amplifier and primary coils; and 2) scanner modifications are required to embed the primary coils into the patient table, which subsequently limits the mobility of the patient table and increases the difficulty of subject positioning.

To reduce the system complexity and the number of wired connections, WPH has been suggested as a promising alternative, where energy from the MRI transmit B_1 field is converted into DC power using inductive coupling in resonant “harvesting”

¹⁰ Image credit: Venkateswaran (2020)

loops (Höfflin (2013), Bryon (2019a), and Venkateswaran (2020)), which requires no scanner modifications. Specifically, WPH utilizes “harvesting” coils to capture the transmit B_1 RF energy from the scanner and an AC-DC converter to rectify the acquired voltage signal (Fig. 1.18). The amplitude of the acquired voltage (V_{acq}) signal in a harvesting coil with area, A , is determined by

$$V_{acq} = \omega N A (\vec{B}_1 \cdot \hat{n}), \quad (1.1)$$

where ω is the Larmor frequency, N is the number of turns in the harvesting coil, and $\vec{B}_1 \cdot \hat{n}$ is the magnetic flux through the coil. Unlike WPT, where the amplitude of the acquired voltage can be controlled via the power amplifier, WPH depends on the amplitude of the transmit B_1 field, which changes for different MR scan parameters to achieve the necessary flip angle (α), given by

$$\alpha = \gamma \frac{MHz}{T} (B_1 t_p), \quad (1.2)$$

Where γ is the gyromagnetic ratio, t_p is the duration of the B_1 pulse. Additionally, the wirelessly harvested power is acquired only during the scanner transmit cycle, which is repeated every TR, resulting in a high temporal variation in V_{acq} (Fig. 1.19, left).

Unfortunately, applying the rectified DC voltage directly to wireless devices is challenging due to the amplitude and smoothness (i.e., temporal stability) dependence on the MR scan type and parameters (Byron (2019) and Venkateswaran (2020)). The rectified DC voltage can be smoothed (i.e., increase the temporal stability) with additional electronics or filtering; however, voltage fluctuations cannot be fully eliminated for long-TR scans (Fig. 1.19, right), whereas over-smoothing would reduce

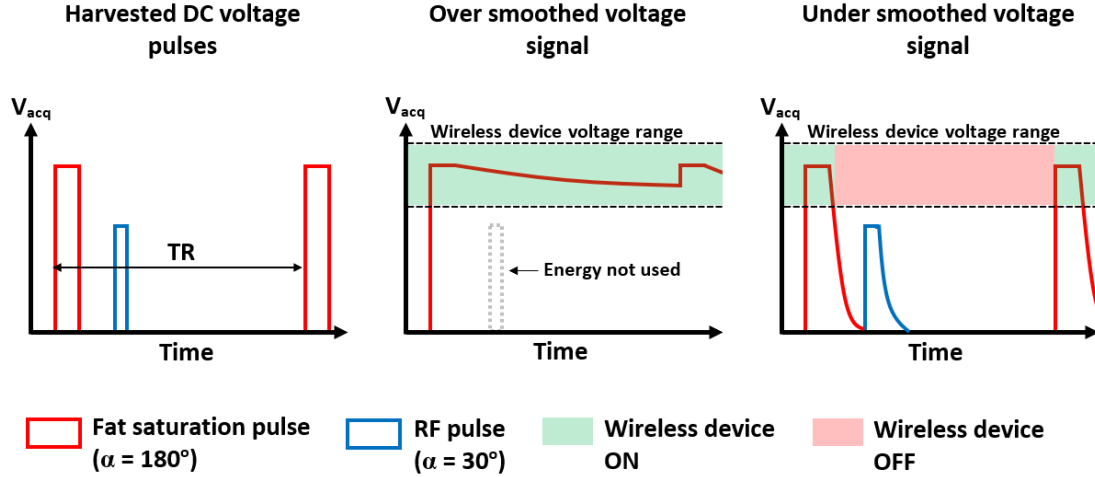


Figure 1.19: Example of acquired RF pulses after passing through an AC-DC converter (left) for a pulse sequence consisting of 180° fat saturation pulses (red) and 30° RF pulses (blue), repeated for every TR. Over or under smoothing the acquired voltage results in low efficiency and unused energy (middle) or high temporal variation (right).

the amount of harvested power for short-TR scans or low-amplitude transmitted B_1 pulses (Fig. 1.19, middle), which could shutoff or damage wireless devices and reduce efficiency, respectively.

1.4 Research Goals

To reduce the number of wired connections in MRI, the novel iRFW coil design (section 1.3.1) was previously proposed and as a first application, combined with the iPRES coil design (section 1.3.2) resulting in the iPRES-W coil design (section 1.3.2). However, an initial proof-of-concept implementation of this coil design showed a limited shimming performance in phantom experiments using a single iPRES-W coil because it only had a single iPRES-W coil element with a limited range (0 mA to 360

mA) and resolution (90 mA) for the DC current used for B_0 shimming, which was insufficient to shim subject-specific localized B_0 inhomogeneities in vivo. Additionally, the MR-compatible battery that provided the shim currents to the prototype iPRES-W coil was not optimized for shimming, resulting in a significant power consumption and requiring the battery to be recharged often (~2-hour constant runtime). Finally, initial experiments only demonstrated the ability of the iPRES-W coil design to wirelessly control the shim currents but did not consider other wireless applications such as peripheral system data acquisition (e.g., respiratory tracking using a respiratory belt) or control of on-coil electronics (e.g., detuning diodes for Q-spoiling).

To address these limitations, this dissertation has four goals: **Aim 1)** to develop a 4-channel iPRES-W spine coil array for simultaneous MR imaging and wireless localized B_0 shimming and demonstrate its ability to correct for distortions in diffusion tensor images (DTI) of the spinal cord in vivo; **Aim 2)** to implement the iPRES-W coil design onto a 48-channel head coil array to enable simultaneous MR imaging and two independent wireless data streams for multiple applications, specifically, to wirelessly control the B_0 shim currents and perform wireless respiratory tracking with a respiratory belt; **Aim 3)** to further develop the iRFW coil design for wireless transfer of the scanner trigger signal to perform the Q-spoiling required for MR image acquisition; **Aim 4)** to design a wireless power harvesting system to convert the high-energy radiofrequency energy emitted by the scanner during the transmit cycle into a DC voltage to charge the batteries used to power the in-bore electronics and B_0 shim currents. In this dissertation,

the analog MR signals for imaging (1st MRI subsystem; section 1.3.1) were still digitized and transferred via the conventional MR receive chain and wired connections of the scanner. While the iRFW and iPRES-W coil designs could be applied for wireless transmission of the MR signal in future work, the development of an on-coil receiver, ADC, and clock synchronization system for the MR signal is beyond the scope of this dissertation.

2. RF Coil Design and Measurement Tools

To acquire an MR image, electromagnetic fields must be generated and received at the Larmor (i.e., resonant) frequency of the water protons within the static B_0 field (e.g., 127 MHz for a 3T scanner). Specifically, transmit RF coils send electromagnetic energy into the body, which is absorbed by the water protons and perturbs their magnetic spins out of alignment with B_0 . After the RF transmit pulse ends, the protons begin to relax and realign with the B_0 field by releasing their absorbed electromagnetic energy back into the environment. This released energy is detected by a receive RF coil placed close to the subject, which generates a current, and therefore a voltage, in response to the changing magnetic fields. The voltage signal generated in the receive RF coil is the raw MR signal and is sent to the console computer to be processed and reconstructed into an image. The image quality depends on both the transmit and receive RF coils, as poor construction of either can reduce the amplitude of the acquired MR signal, increase signal noise, or induce image artifacts. In the work presented in this dissertation, modifications are made to the receive RF coils required for the iRFW, iPRES, or iPRES-W coil designs. As such, it is important to ensure that the modifications do not change the electrical characteristics or resonant frequency of the receive RF coil, which would degrade SNR and image quality.

2.1 Receive RF Coil Elements and Arrays

Each receive RF coil element is designed to resonate (i.e., listen) at a specific frequency to couple the RF signal from the water proton spins to the scanner electronics. A conventional RF coil element is a single-loop inductor-capacitor (LC) circuit constructed out of a loop of copper wire with several capacitors evenly placed around the circumference (Fig. 2.1, red). As the MR signal interacts with the RF coil element, it induces a current, which quickly charges and discharges the capacitors, generating an oscillating current. The rate at which the LC coil structure generates this oscillating current is its resonant frequency, which must be tuned to match the Larmor frequency to maximize the amplitude of the induced MR signal voltage. The impedance (Z) of this coil structure at a given frequency can be calculated by

$$Z = \sqrt{R^2 + (X_L - X_C)^2}, \quad (2.1)$$

and depends on the resistance (R) and inductive reactance (X_L) of the wire and added capacitive reactance (X_C) from the lumped components about the coil perimeter. The coil impedance must be matched to the impedance of the receiving pre-amplifier (i.e., low-noise amplifier (LNA)) to maximize the amplitude of the MR signal transferred to the scanner (Fig. 2.1, green). The impedance is “matched” when the load resistance ($R_{\text{pre-amplifier}}$) and source resistance (R_{coil}) are equal, and the load reactance ($X_{\text{pre-amplifier}}$) is equal to the negative of the source reactance ($-X_{\text{coil}}$). The circuit reactance depends on frequency, therefore circuits which are impedance matched at one frequency may not be matched if the frequency is changed. Impedance matching over a bandwidth is required

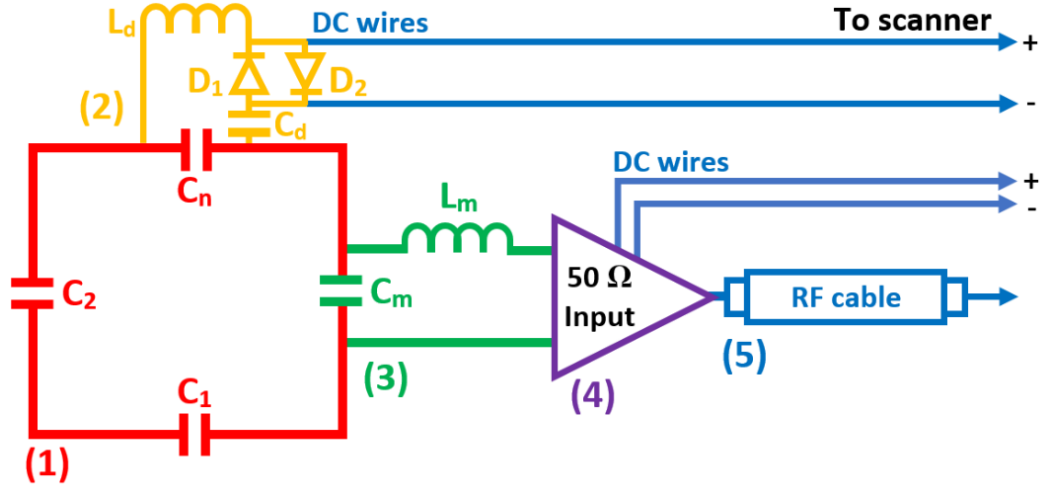


Figure 2.1: A conventional RF coil element consists of the 1) copper loop (red), 2) detuning circuit (orange), 3) match circuit (green), 4) preamplifier (purple), and 5) RF and DC cables (blue) which connect to the scanner.

for RF coils in MRI to account for variations in the proton's Larmor frequency, which arise due to spatial variations in the B_0 field caused by either the gradient coils or localized B_0 inhomogeneities.

The coil resonates at the frequency (f_{coil}) for which the impedance has a completely real value ($Z = R$ and $X_L = X_C$ in Eq. 2.1) and can be calculated by

$$f_{coil} = \frac{1}{2\pi\sqrt{LC}}, \quad (2.2)$$

where L and C are the coil inductance and capacitance, respectively.

Next, an additional capacitor (C_d) is used with an inductor (L_d) to form the detuning circuit for Q-spoiling (Fig. 2.1, orange). The detuning circuit behaves as a transmit/receive switch by activating the PIN diodes (D_1 and D_2) during the scanner transmit phase, which drastically changes the impedance and resonant frequency of the coil element to protect the sensitive receive electronics. DC wires connect between the

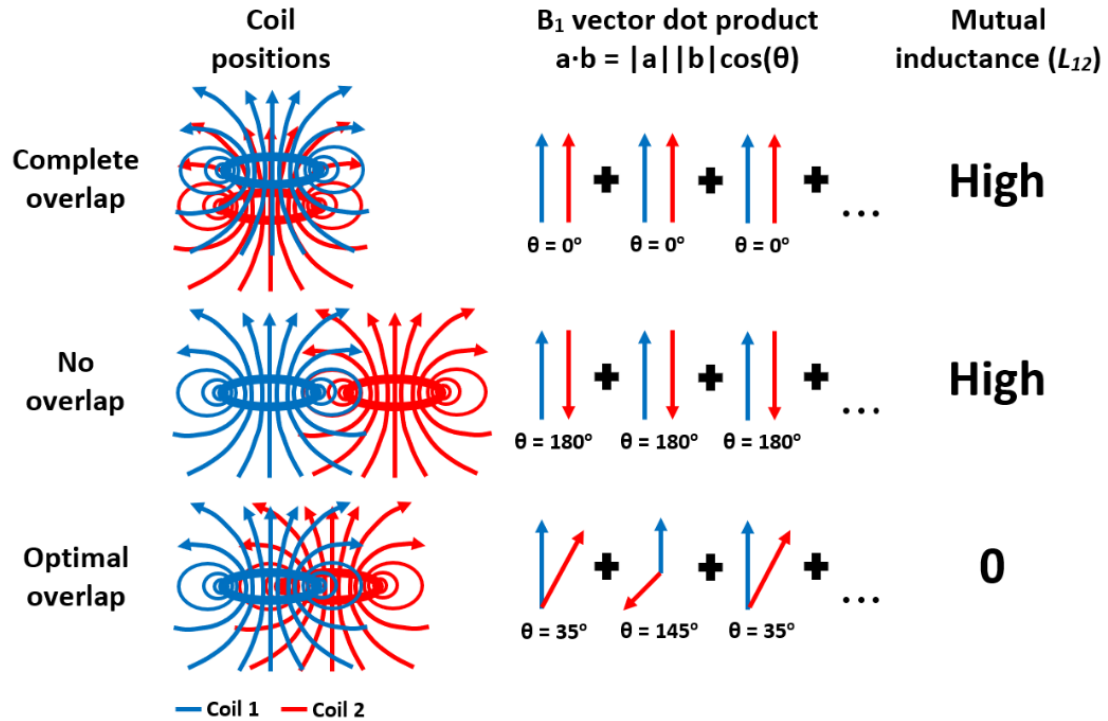


Figure 2.2: RF coil elements that have too much or not enough overlap with each other have a high mutual inductance (L_{12}). In contrast, RF coil elements that are optimally overlapped (or orthogonal, not shown) have a small or 0 mutual inductance as dot product values will combine and cancel out when integrated over the volume.

detuning circuit and MR scanner to supply the required activation voltage (Fig. 2.1, blue).

Before the acquired MR signal is transferred to the scanner for reconstruction, it passes through the LNA, which increases the MR signal amplitude without introducing additional noise or significantly degrading the SNR (Fig. 2.1, purple). The LNA is often placed close to the RF coil element and impedance matching circuit to minimize signal loss. Its output connects to an RF cable, which transfers the MR signal to the console room computers for image reconstruction (Fig. 2.1, blue).

The MR signal amplitude received by an RF coil element depends on the distance between the coil element and the tissue where the signal is generated. As such, the signal intensity is highest at the surface of the tissue, closest to the RF coil element, and gradually decreases further away (e.g., laterally or at deeper tissue depths). To provide high sensitivity over a larger VOI, multiple RF coil elements are arranged in an overlapping pattern to create a phased or RF coil array. Additionally, the use of multiple RF coil elements allows for shorter examination times by decreasing the number of phase-encoding steps required for spatial localization of the MR signal (Pruessmann (1999)). However, when two adjacent RF coil elements are brought together they couple to one another, which shifts the resonant frequency of each coil element and reduces SNR. The signal coupling (k) between two RF coil elements can be expressed by

$$k = \frac{L_{12}}{L_{coil_1}L_{coil_2}}, \quad (2.3)$$

where L_{12} is the mutual inductance between the two coil elements, and can be estimated by

$$L_{12} = \frac{1}{\mu} \int \mathbf{B}_{1,coil_1} \cdot \mathbf{B}_{1,coil_2} dV. \quad (2.4)$$

To minimize the coupling coefficient, k , and the mutual inductance, L_{12} , the RF coil elements must be overlapped such that the magnetic flux through coil 1 cancels out the magnetic flux through coil 2, produced by the magnetic fields of coils 2 and 1, respectively, and represented by the dot product ($\mathbf{B}_{1,coil_1} \cdot \mathbf{B}_{1,coil_2}$). The optimal position of the coil elements where the magnetic flux from the coils cancels out is known as the

critical overlap point (Fig. 2.2) (Roemer (1990)). However, this makes the positioning of the coils difficult when designing an RF coil array as it restricts the positioning and number of RF coil elements.

2.2 Evaluating the RF Coil Performance

Mathematical formulas and approximations are useful during the initial design phase of an RF coil element, however, numerous outside factors (e.g., parasitic inductance or capacitance, material compositions, amount of solder, etc.) can impact the resonant frequency or acquired MR signal amplitude by changing the inductance, capacitance, or impedance (e.g., mismatch to the LNA) of the coil. These outside factors make designing an RF coil array or adding the modifications required for an iRFW, iPRES, and iPRES-W coil array nearly impossible using mathematical formulas alone, as mutual inductance between numerous coil elements cannot be easily calculated. As such, four key measurement tools are utilized throughout this dissertation to evaluate the RF coil element performance and the DC circuits for the wireless battery pack in a controlled and repeatable manner, specifically, 1) a vector network analyzer (VNA) to measure the RF circuits, 2) an MRI scanner for image quality and SNR, 3) an anechoic chamber to evaluate wireless performance, and 4) an oscilloscope for DC and low-frequency RF circuits.

2.2.1 Vector Network Analyzer

The resonant frequency of an RF coil element, RF filter and impedance matching circuits, and coil coupling can all be evaluated experimentally using a VNA (Fig. 2.3) by measuring the reflected and/or transmitted power of the device under test (DUT) attached to the instrument. Specifically, each port of a VNA generates a signal (Fig. 2.4, f_{test}) and measures the percent of the signal that is either reflected or transmitted to another active port (i.e., S-parameters). For example, 1) the gain of an LNA can be measured by the percent increase in the transmitted signal between ports 1 and 2 (S_{12}), 2) the isolation provided by an RF filter can be measured by the percent decrease in the transmitted signal between ports 1 and 2 (Fig. 2.4, S_{12}), or 3) the resonant frequency of an RF coil element can be determined by looking at where the impedance is matched (e.g., 50 ohms) and the percent of reflected signal (Fig. 2.4, S_{11}) is minimal, since the energy is transmitted into the environment rather than reflected to the VNA. As such,



Figure 2.3: Photo of the 4-port VNA (ZNB 4) used for evaluation and verification of the iRFW, iPRES, and iPRES-W coil designs¹¹.

¹¹ Image credit: <https://www.rohde-schwarz.com>

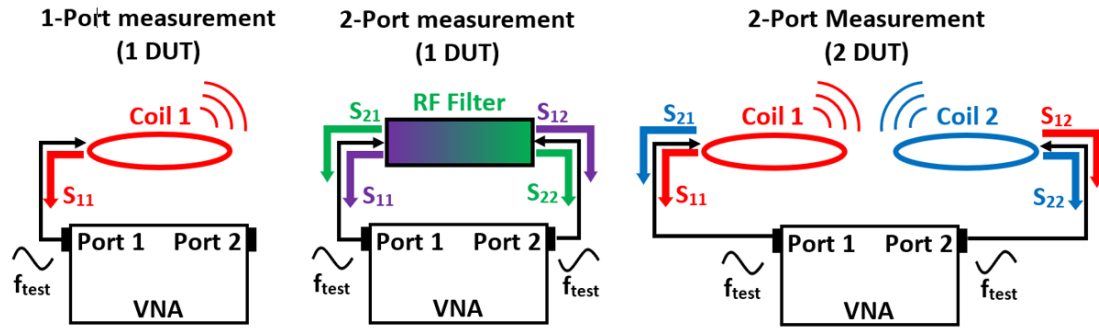


Figure 2.4: Various setup configurations for a 2-port VNA, which depend on the devices under test and required S-parameter measurements.

interpretation of the S-parameter measurements depend on the experimental setup and DUTs involved.

S-parameter measurements acquired with a VNA have an amplitude and phase component, which are drastically impacted by small or unaccounted changes in the setup (e.g., adding a cable connector or extra cable). To ensure correct S-parameter measurements, a calibration process is performed to account for all phase or amplitude losses associated with the VNA setup. The calibration is performed by presenting three different impedance values at the calibration reference plane (Fig. 2.5, red line), specifically, short (low impedance), match (50 Ohm load matched to the transmission line impedance), and open (high impedance), which accounts for all possible impedances measured by the VNA. Additionally, for a multi-port VNA, the isolation between each port is measured to determine the insertion loss of the setup. After this, the calibration process is complete and the VNA measurements are accurate assuming that the DUT is connected to the calibration reference phase plane. However, in practice

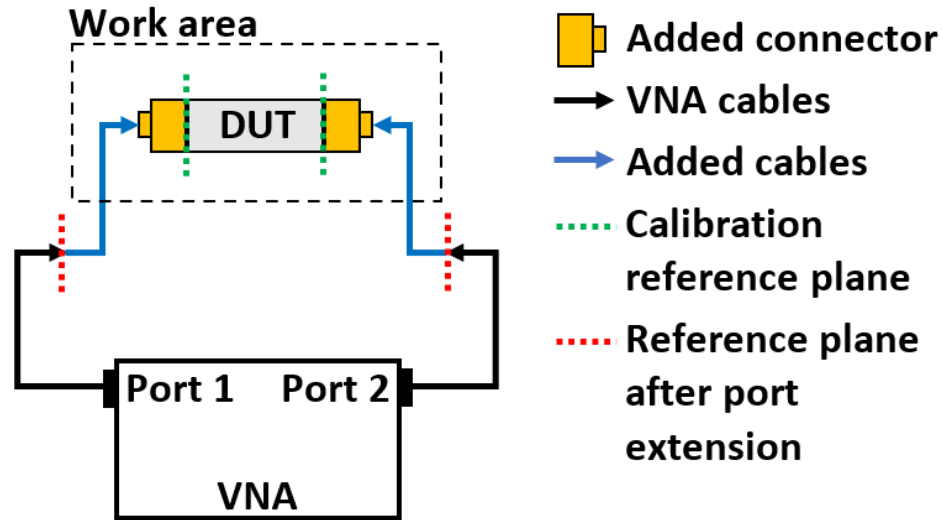


Figure 2.5: The VNA is calibrated and port extended to account for any phase shifts and losses associated with the setup or added connectors and cables.

this is often not possible, as additional connectors (Fig. 2.5, gold) and cabling (Fig. 2.5, blue) must often be added between the DUT and calibration reference plane. The added phase and loss must be corrected for by port extending the VNA calibration to the reference phase plane after any added cables or connectors (Fig. 2.5, green). After the port extension has been completed and the DUT connected, the calibration process is complete and the VNA is ready for use.

2.2.2 Image Quality and Signal-to-Noise-Ratio

Designing and engineering devices, such as the wireless battery pack and wireless module, to operate inside the MR scanner bore can be extremely difficult because the strong magnetic fields inside the bore can quickly break a component of device via high induced RF voltages, mechanical vibrations, or torque caused by eddy

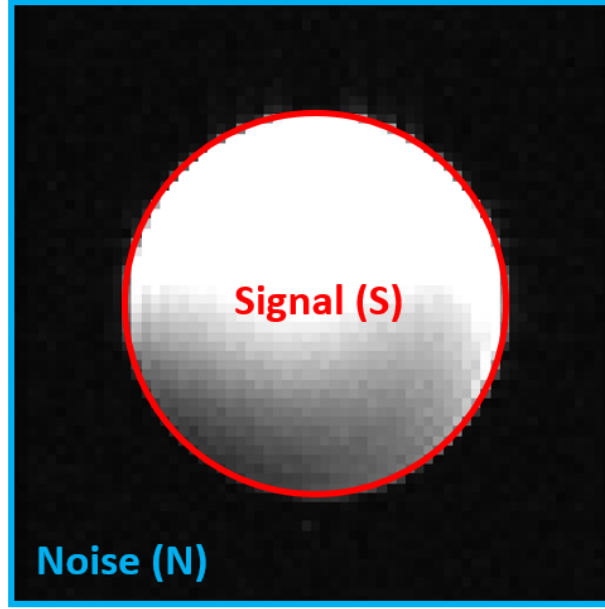


Figure 2.6: Example image of a water phantom where the signal (S) and noise (N) are calculated from the pixels inside or outside of the mask (red), respectively.

currents. Additionally, it is vital that the device electronics do not degrade SNR, add a source of RF noise, or introduce image artifacts. Image quality and the MR-compatibility can be evaluated quantitatively by measuring 1) the SNR to evaluate changes in the MR signal or RF noise levels from the iPRES-W coil modifications or 2) the B_0 root-mean-square error (RMSE) to evaluate the MR-compatibility of device electronics.

To measure the SNR, the signal and noise must be measured independently, which is typically performed on a uniform water phantom by acquiring images over the entire volume of the phantom. After image reconstruction, a mask is applied to encircle the phantom and the SNR is calculated by

$$SNR = \frac{S}{N} = \frac{\frac{1}{n_{inside}} \sum I(x_{in}, y_{in})}{\sqrt{\frac{\sum (I(x_{out}, y_{out}) - \mu)^2}{n_{out}}}} \quad (2.7)$$

where the signal, S , is measured as the mean pixel intensity inside the mask ($I(x_{in}, y_{in})$) and the noise (N) is the standard deviation of pixel intensity from air outside the mask ($I(x_{out}, y_{out})$) (Fig. 2.6). This is performed over the 3D phantom and the average SNR over the entire phantom is reported. SNR can be calculated for either individual RF coil elements or for the combined signal from an entire RF coil array.

The second quantitative image quality measurement is the B_0 RMSE, which is useful to evaluate the MR-compatibility of device electronics as magnetic material inside the parts can disrupt the uniform B_0 field and cause strong localized B_0 inhomogeneities. First, a baseline B_0 map is acquired on a uniform water phantom (i.e., a map of the relative magnetic field strength inside the phantom). Next, the component or device is placed next to the phantom and a second B_0 map is acquired. The B_0 RMSE is calculated as

$$B_0 \text{ RMSE} = \sqrt{\frac{\sum (B(x_{first}, y_{first}) - B(x_{sec}, y_{sec}))^2}{n}} \quad (2.8)$$

where $B(x_{first}, y_{first})$ and $B(x_{sec}, y_{sec})$ are the B_0 values in the first and second B_0 maps, respectively. Ideally, the B_0 RMSE should be zero or very small, meaning that the introduced component causes no significant localized B_0 inhomogeneities, which can otherwise cause image distortions or signal loss (Fig. 2.7). If the B_0 RMSE is nonzero, the component or device should be replaced with a suitable non-magnetic option or moved far enough away from the image ROI to not degrade image quality.

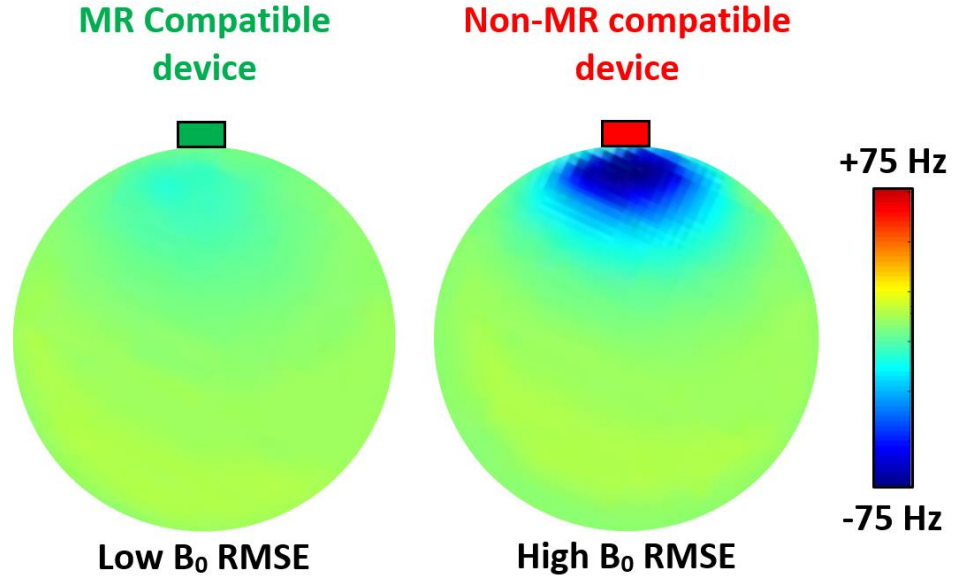


Figure 2.7: B₀ maps showing how a magnetic or non-MR compatible device (red) can cause localized B₀ inhomogeneities and a high B₀ RMSE, while an MR-compatible device (green) has little to no impact on B₀.

2.2.3 Anechoic Chamber

An anechoic chamber is a specially designed room that completely absorbs electromagnetic waves radiated from a device under test (DUT) and also provides isolation from any external noise to the DUT while radiated measurements are being performed. In this dissertation, a 2.5 x 1.5 x 1.6 m anechoic chamber lined with cone shaped foam RF absorbers (operational frequency range: 900 MHz – 6 GHz) was used to evaluate the wireless performance of either the iRFW or iPRES-W coil elements, apart from any external factors such as RF interactions with the MRI scanner bore, subject anatomy, or the scanner room layout. To ensure accurate measurements, the chamber is calibrated using a three-antenna extrapolation method, where three sets of S-parameter

measurements are performed to obtain three gain product equations (Fig. 2.8) (Xiao (2019)). These equations are then solved to determine the gain of each calibration antenna individually (G_{cal}). Next, one of the calibration antennas is chosen to be the receive antenna and S_{12} measurements (P_r) are acquired using the DUT. The gain of the DUT (G_{DUT}) is solved for by using

$$P_r = P_t G_{DUT} G_{cal} \left(\frac{\lambda}{4\pi R} \right)^2 \quad (2.9)$$

where P_t is the known transmit power, R is the distance between the two antennas, and λ is the frequency wavelength being measured.

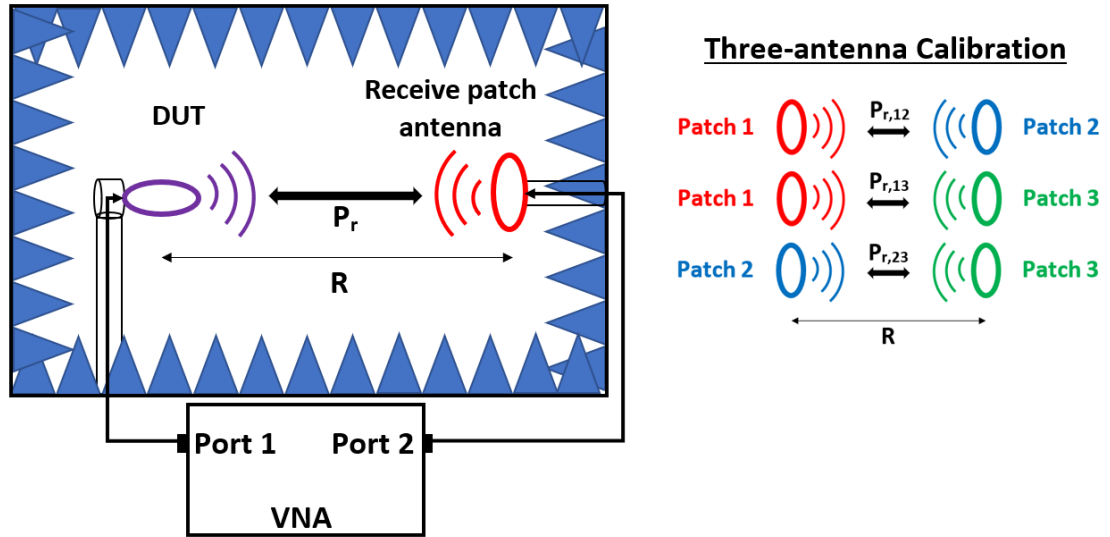


Figure 2.8: The DUT (purple) and receive patch antenna (red) are each connected to a VNA port and placed on opposite ends of the anechoic chamber, separated by a distance R . During the three-antenna gain measurement calibration, the DUT is removed, and measurements are acquired using the three sets of patch antennas (red, blue, and green).

3. Aim 1: The iPRES-W Spine Coil Array

3.1 Introduction

The first aim of this dissertation is to remove the cables for the localized B_0 shimming subsystem and enable wireless localized B_0 shimming, specifically for improved image quality in the spinal cord, without requiring any additional antenna systems or scanner modifications. Diffusion-weighted imaging and diffusion tensor imaging (DTI) of the spinal cord can help distinguish between benign and malignant tumors (Smith (2006)), enable the early detection of spinal cord infraction (Thurnher (2006)), and detect changes in white matter integrity through fiber tracking to provide additional information for spinal cord diseases (Rajasekaran (2012)) (e.g., multiple sclerosis (Avadhani (2010))). Additionally, spinal cord fiber pathways can be used as a minimally invasive conduit to the brain to deliver electrical stimulation and treat various brain disorders (e.g., Parkinson's disease (Fuentes (2009) and Souza (2017))). However, DWI and DTI are affected by image artifacts such as geometric distortions and incomplete fat suppression caused by localized B_0 inhomogeneities near air/tissue interfaces (e.g., esophagus, trachea, lungs) and bone/tissue interfaces (e.g., vertebrae) near the spinal cord, which can drastically reduce the image quality.

Since these localized B_0 inhomogeneities cannot be effectively shimmed using whole-body 2nd order SH shim coils (Topfer (2016)), several alternative methods to shim the spinal cord have been previously investigated, which use either one (Biber (2012)) or two (Walter (2019)) local shim coils or a larger 24-channel MC shim array (Topfer (2016))

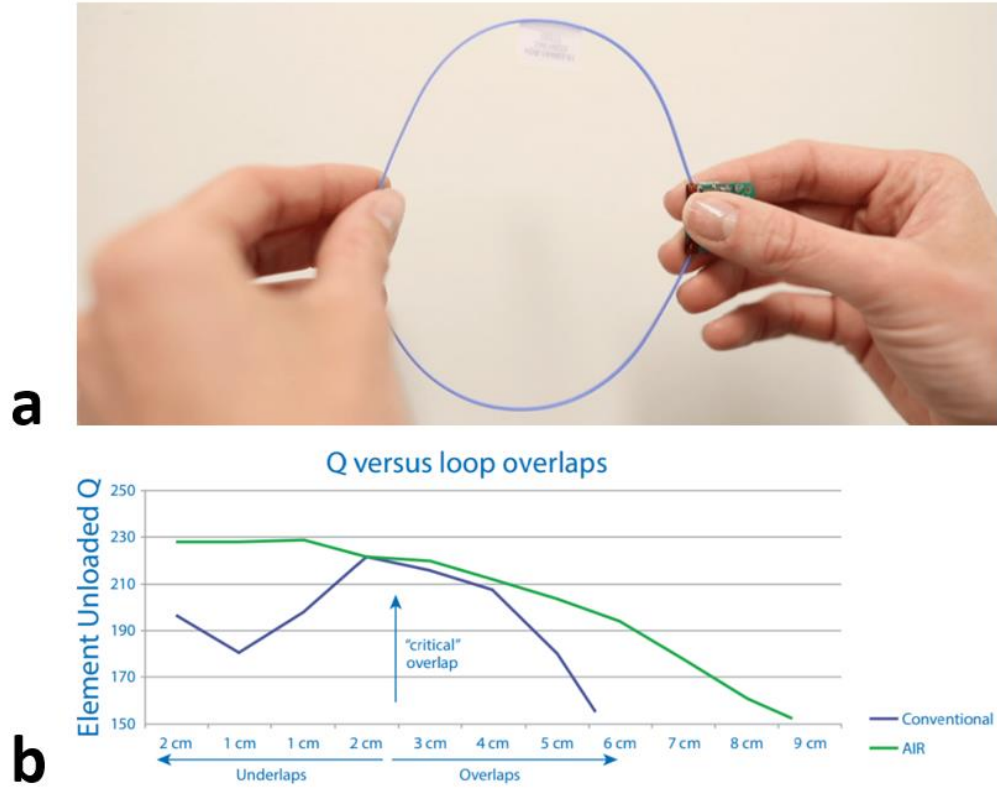


Figure 3.1: Image of the AIR™ coil element (a) and comparison of the critical overlap region (b) between an AIR™ coil (green) and conventional RF coil (purple), which allows a wider range of overlap between two neighboring coil elements without degrading SNR.¹²

and Topfer (2018b)). However, these methods require separate RF and shim coil arrays and therefore require additional DC wires, RF filters, and cable traps for operation, which take up space in the MR scanner bore and can degrade either SNR or shimming performance. In this work, we address these limitations and reduce the number of wired connections by further developing the iPRES-W coil design for wireless localized B_0 shimming in vivo. Specifically, the iPRES-W coil design is integrated onto a 4-channel adaptive image receive (AIR™) RF coil array (McGee (2018) and Collick (2020)), which

¹² Image credit: Stormont (2017)

has two advantages over conventional RF coils. First, the AIR™ coil elements (Fig. 3.1a) use a distributive capacitance around the loop, rather than lumped capacitors placed around the perimeter of traditional RF coil designs. As such, no additional bypass inductors are required to allow a DC current to flow for shimming, which significantly simplifies the iPRES-W coil design. Second, the AIR™ coil elements have a larger critical overlap range, which allows them to be positioned more freely and easily within the array without degrading the SNR (McGee (2018)) (Fig. 3.1b). To demonstrate the ability to wirelessly shim localized B_0 inhomogeneities in the cervical spinal cord in vivo, DTI experiments are performed. Additionally, antenna performance and power consumption measurements are performed with the iPRES-W coil in an anechoic chamber to evaluate its wireless performance and battery runtime for wireless data transfer. Preliminary results have been presented in abstract form (Cuthbertson (2018) and Cuthbertson (2019)) and published in Magnetic Resonance in Medicine (Cuthbertson (2022b)).

3.2 iPRES-W Coil Design Implementation

First, a 4-channel coil array was constructed by attaching four AIR™ coil elements (McGee (2018) and Collick (2020)) (11-cm diameter) onto a rigid 3D-printed frame to comfortably support the subject's head (Fig. 3.2b). These coils were made from a thin (0.6-mm diameter) conductive link resonant structure where the length of each conductor was less than $1/10^{\text{th}}$ of the wavelength of the RF field at the Larmor frequency

to ensure that the resonator acts as a lumped element circuit rather than a transmission line (McGee (2018)). This resonant loop was connected to a printed circuit board (PCB) module (5855633, GE Healthcare, Waukesha, WI), which provided an impedance matching circuit, an LNA, and an RF choke (Fig. 3.3, dashed black box). In this work, the DC shim currents were wirelessly controlled, but the analog RF signals for MR image acquisition were still digitized and transferred via conventional wired connections to the MR receiver. Additionally, the DC bias for coil detuning were transferred to the coil array via wired connections to the scanner. The coil elements were secured to the frame using a cyanoacrylate adhesive (Loctite 414, bond strength > 1,745 psi) to ensure that they would not deform or vibrate during imaging due to Lorentz forces generated by the DC currents used for shimming (maximum torque of 0.04 Nm experienced when a maximum DC current of 1.3A flows on an iPRES or iPRES-W coil element parallel to B_0).

Next, all four coil elements were modified into iPRES coil elements by adding inductive chokes ($L_{\text{choke}}^{127 \text{ MHz}} = 820 \text{ nH}$, $R_{\text{DC}} = 0.02 \Omega$) between each coil element and an MR-compatible battery pack placed inside the scanner bore, which provided the four adjustable DC currents for B_0 shimming (Fig. 3.2, blue). These chokes prevented the RF currents at 127 MHz from flowing into the battery pack ($S_{21}^{127 \text{ MHz}} = -25 \text{ dB}$), which would reduce the MR signal amplitude and thus the SNR.

Next, one of the iPRES coil elements was further modified into an iPRES-W coil element by inserting a low-loss high impedance ($Z^{127 \text{ MHz}} > 1 \text{ k}\Omega$, $S_{21}^{2.4 \text{ GHz}} = -0.6 \text{ dB}$) bandstop filter tuned to resonate at 127 MHz (Fig. 3.2, orange, coil 4) between this coil

element and the 50- Ω transmission line of a wireless module (ESP8266, Adafruit, New York, NY). This bandstop filter prevented the RF current at 127 MHz from flowing into the wireless module, which would degrade SNR. Similarly, a second low-loss high-impedance ($Z^{2.4 \text{ GHz}} > 1 \text{ k}\Omega$, $S_{21}^{2.4 \text{ GHz}} = -0.3 \text{ dB}$) bandstop filter tuned to resonate at 2.4 GHz (Fig. 3.2, red, coil 4) was placed between this coil element and the MRI preamplifier. This bandstop filter prevented RF currents within the wireless communication band (2.412-2.472 GHz) from flowing into the preamplifier, which would decrease the radiated power from the iPRES-W coil element. Additionally, the same bandstop filter was added into the remaining iPRES coil elements (Fig. 3.2, red, coils 1-3) to provide -56, -45, and -40 dB of isolation at 2.4 GHz between each respective preamplifier and the iPRES-W coil element. Finally, inductive chokes ($L_{\text{choke}}^{2.4 \text{ GHz}} = 27 \text{ nH}$, LQW2BAN27NG00L, Murata Manufacturing, Kyoto, Japan) were added to provide -20 dB of isolation at 2.4 GHz between each of the four coil elements and the battery pack. These chokes prevented the RF currents within the wireless communication band from flowing into the battery pack, which would degrade the radiated power amplitude and wireless performance.

3.3 Battery Pack Design and Implementation

The initial proof-of-concept iPRES-W implementation (Darnell (2019)) provided limited B_0 shim current values (80, 160, 250, or 360 mA) and was unable to correct for subject-specific localized B_0 inhomogeneities in vivo. To address this limitation, a wireless battery pack was developed with an adjustable high-resolution (3 mA) current

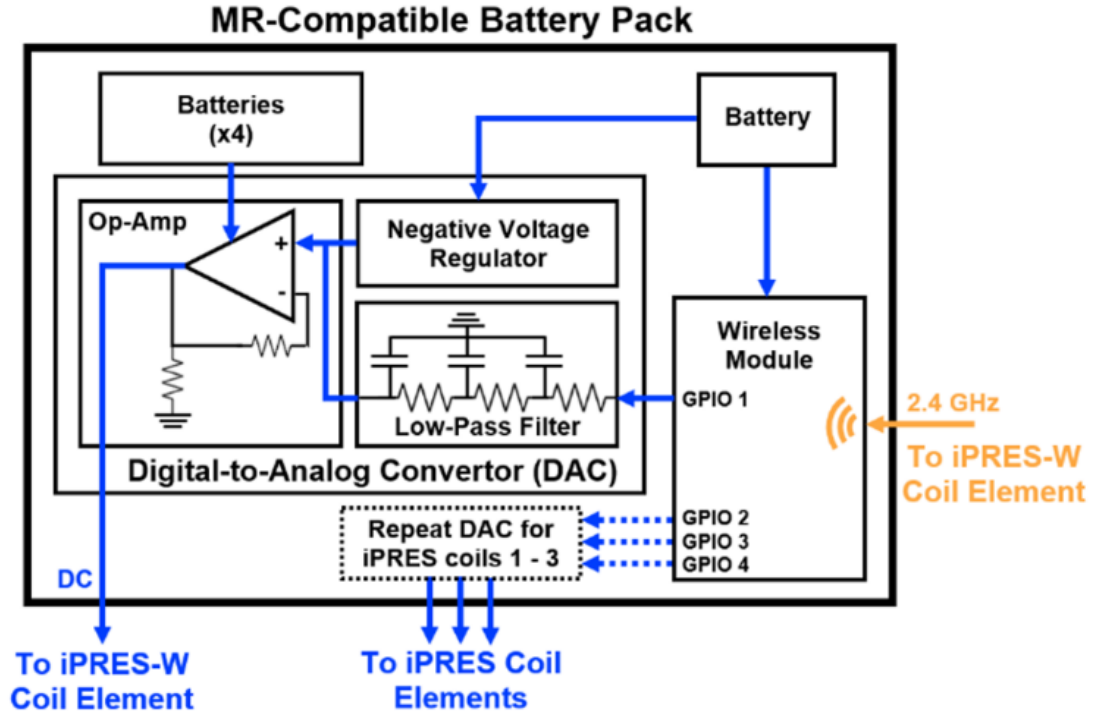


Figure 3.4. Schematic of the wireless battery pack placed within the scanner bore, which supplied and wirelessly controlled (orange) the DC currents (blue) in the iPRES and iPRES-W coil elements for localized B_0 shimming.

output and a larger bidirectional dynamic range (± 1.3 A), which supplied the currents to the iPRES and iPRES-W coil elements.

The battery pack consisted of five 1800-mAh lithium polymer (LiPo) batteries (GM-NM103450-PCB, PowerStream Technology, Orem, UT), a PCB for signal filter and voltage control, and the wireless module, which were all enclosed within a 3D-printed case. Since the components were non-magnetic, the battery pack was placed next to the iPRES-W coil array within the scanner bore. In this design, one battery powered the wireless module and the other four supplied the adjustable DC currents for shimming. The DC currents were wirelessly controlled using four of the 3.3-V digital general-

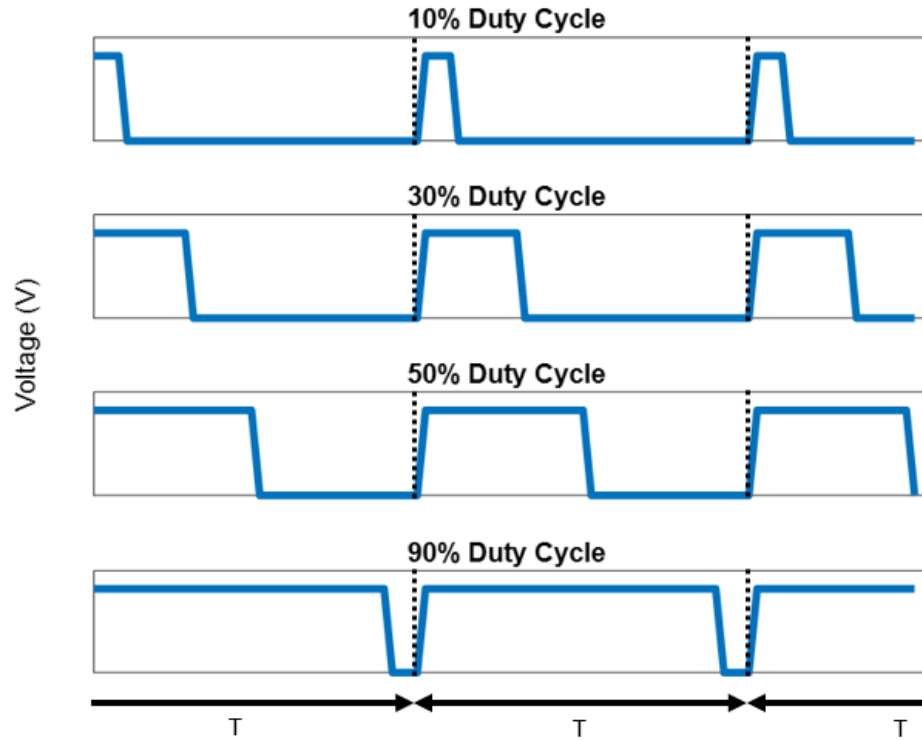


Figure 3.5. The duty cycle of a PWM signal depends on the frequency ($1/T$) of the square wave and the duration that the signal is turned on. As the duty cycle increases, so does the average voltage over time.

purpose input/output (GPIO) pins of the wireless module (programed using the open-source Arduino IDE software), where one GPIO pin was used per coil element (Fig. 3.4). First, each GPIO pin was quickly switched on and off to generate a square-wave or pulse-width-modulated (PWM) signal (PWM frequency = 4 kHz), where the average voltage was determined by the duty cycle (i.e., on-to-off ratio) of the PWM signal (Fig. 3.5). Next, the generated PWM signal was passed through a custom-designed three-stage RF low-pass filter (cutoff frequency = 20 Hz, rise time = 18 ms, ripple < 1 mV), which removed the frequency components (Fig. 3.6) and resulted in a stable and adjustable DC voltage (range = 0 to 3.3 V). This output voltage was then combined with

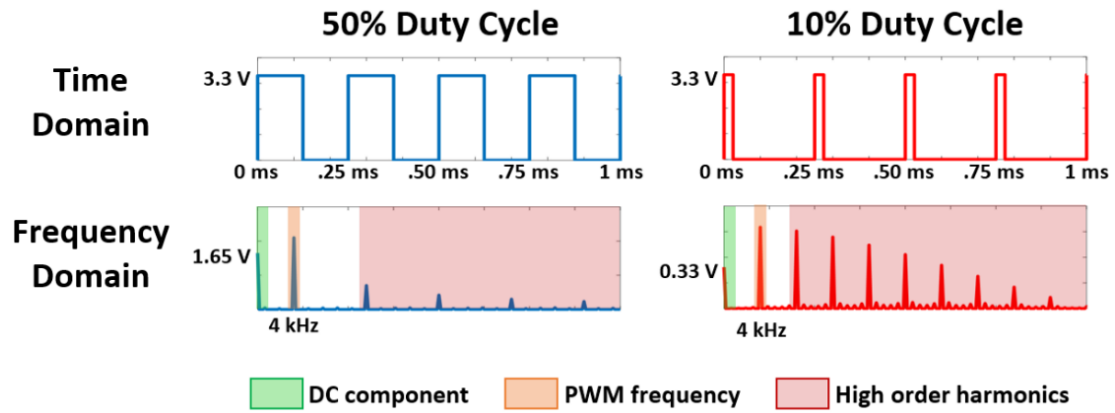


Figure 3.6. Example 4 kHz PWM signals for a 50% and 10% duty cycle (top). Taking the Fourier transform decomposes the PWM signal into its frequency components (bottom), which include the DC component (0 Hz), the main PWM frequency component (4 kHz), and higher order harmonic components (e.g., 8 kHz, 12 kHz, 16 kHz, etc.).

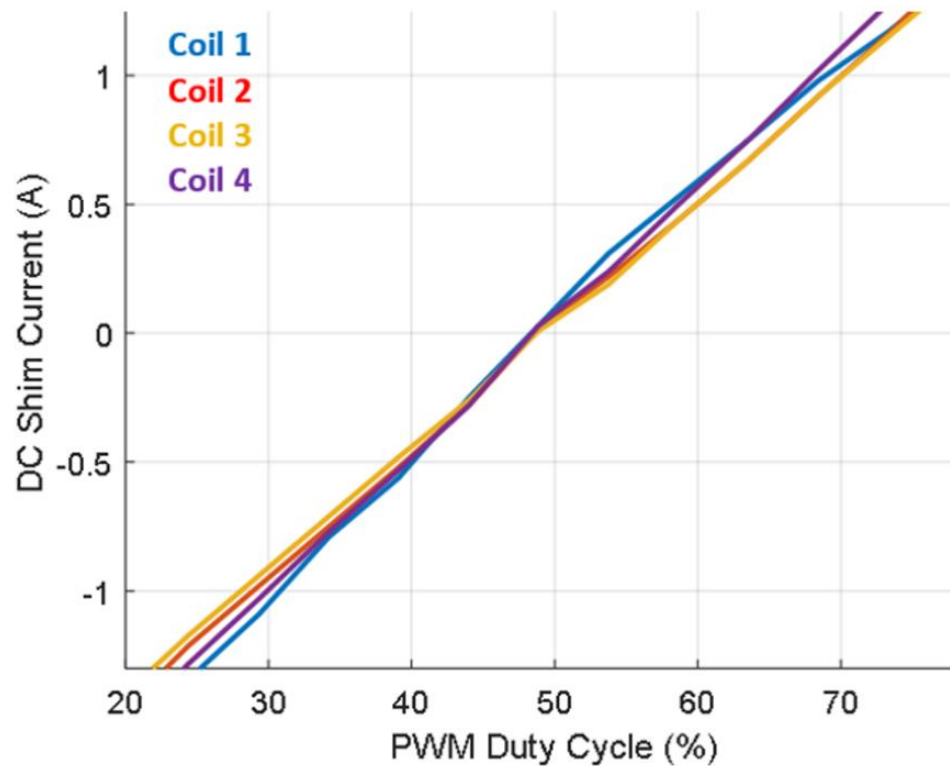


Figure 3.7: Linearity of the DC currents used for B_0 shimming as a function of the PWM duty cycle for each GPIO pin of the wireless module.

the output from a negative voltage regulator (LT1033, -1.65 V output) and applied to the non-inverting input of a linear power operational amplifier (op-amp), where each op-amp gain was adjusted to supply the correct DC voltage range to the iPRES or iPRES-W coil elements, depending on their intrinsic DC resistance. The op-amps were powered by four of the MR-compatible batteries, using two batteries in parallel to provide positive and negative voltage rails, which resulted in a linear filtered DC current for shimming (Fig. 3.7), that had a range of ± 1.3 A, a resolution of 3 mA, and less than 1 mA of noise. Finally, the PWM signals and resulting DC currents for each coil element were wirelessly controlled via transmission control protocol/internet protocol (TCP/IP) and serial commands sent from a computer in the console room to the wireless module using the wireless connection between the iPRES-W coil element and a wireless router access point (AP) mounted on the scanner room wall.

The four batteries in their parallel configuration had a total capacity of 3600 mAh for both the positive and negative voltage rails. For average currents required to shim in vivo, which have both positive and negative values, the expected runtime is ~ 2 hours. The batteries were recharged in the same amount of time, making it possible to interchange two battery packs with minimal interruption in clinical workflow. The single battery powering the wireless module had a runtime of ~ 12 hours before needing to be recharged.

3.4 Experimental Setup and Tests

3.4.1 Temperature Measurements

The first experiment was to verify that the battery pack and coil elements would not overheat and cause a safety risk to the subject or in-bore electronics during wireless shimming. Temperature measurements were conducted using a data logger (Keysight 34970A, Santa Rosa, CA) and surface adhered thermocouples placed at different locations on the battery pack, specifically, the 3D-printed case, wireless module, op amp, and batteries, and on the iPRES-W coil array, specifically, the 3D-printed structure, iPRES-W coil element, and iPRES-W coil PCB, with the maximum DC current of 1.3 A

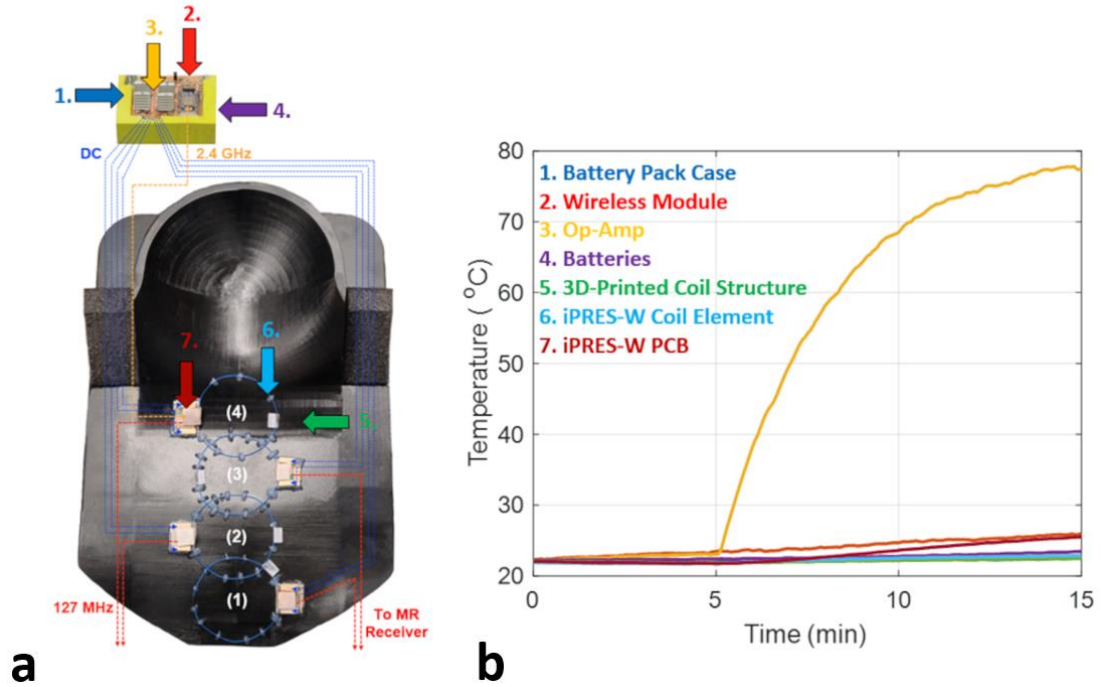


Figure 3.8: Thermocouples were placed on the 3D-printed battery case (a) and measured the temperature change with the wireless module powered on but no DC currents applied to the coil elements (0-5 min) and with the maximum DC current of 1.3 A applied to all four coil elements for 10 min (5-15 min) (b).

continuously applied to all coil elements for a duration of 10 minutes to reach a steady state thermal equilibrium on the battery pack components (Fig. 3.8).

3.4.2 SNR Measurements

To demonstrate that the coil modifications required to enable localized B_0 shimming and wireless data transfer did not degrade image quality, SNR maps were acquired in a water phantom with an AIR™ coil element in the three different configurations; baseline, iPRES, and iPRES-W. The SNR maps were acquired with a gradient echo (GRE) pulse sequence (TR = 200 ms, TE = 1.4 ms, FOV = 25.6 x 12.8 cm, matrix size = 64 x 32, slice thickness = 4 mm) and were computed as described in section 2.2.2. All MRI experiments were performed on a 3T Premier Ultra-High Performance MRI scanner (GE Healthcare, Milwaukee, WI) and the data analysis was performed in MATLAB (The MathWorks, Natick, MA).

3.4.3 DTI of the Cervical Spinal Cord and Wireless Localized Shimming

In a third experiment, DTI images were acquired in the cervical spinal cord in vivo with the iPRES-W coil array to demonstrate that it could perform simultaneous MR image acquisition and wireless localized B_0 shimming to improve the image quality. First, a one-time calibration was performed by acquiring four ΔB_0 maps in a water phantom with a DC current of 1 A successively applied to each of the four coil elements.

A ΔB_0 map was also acquired with no DC currents and was then subtracted from each of these ΔB_0 maps, resulting in a set of four basis ΔB_0 maps, which represented the magnetic field per unit current generated by each coil element. All ΔB_0 maps were acquired with a multi-echo GRE pulse sequence (TR = 200 ms, TE = 1.4 ms, ... 10 ms, echo train length = 8, FOV = 25.6 x 12.8 cm, matrix size = 64 x 32, slice thickness = 4 mm).

The ability to provide wireless B_0 shimming of the cervical spinal cord using the iPRES-W coil array was demonstrated on four healthy volunteers (2 males, 2 females). First, 1st-order shimming from the scanner was applied to the entire FOV and a sagittal baseline ΔB_0 map and DTI images of the cervical spinal cord were acquired with no DC currents applied to the coil elements. Next, the optimal DC currents to shim an ROI around the cervical spinal cord of each subject were calculated by minimizing the RMSE between the baseline ΔB_0 map and a linear combination of the basis ΔB_0 maps acquired in the phantom, which was performed in MATLAB (*fmincon* function) and constrained the DC currents within a range of ± 1.3 A (i.e., maximum output of the battery box). Slice-optimized shimming was performed in a thin slab consisting of the midsagittal slice and the two adjacent slices to take the through-plane B_0 gradient into account (Juchem (2011b), Truong (2014), and Aghaeifar (2018)). Finally, a ΔB_0 map and DTI images were acquired after applying the optimal DC currents to the coil elements to shim the B_0 inhomogeneities and to correct for the corresponding distortions. For better visualization of these distortions, contour lines derived from undistorted anatomical images were overlaid onto the baseline and shimmed isoDWI images (i.e., mean of all

diffusion-weighted images), mean diffusivity (MD) maps, and fractional anisotropy (FA) maps derived from the DTI images. The DTI and anatomical images were acquired with a spin-echo single-shot EPI pulse sequence (TR = 2.1 s, TE = 45 ms, FOV = 25.6 x 12.8 cm, matrix size = 128 x 64, frequency-encoding direction = superior/inferior, slice thickness = 4 mm, b = 600 s/mm², 25 diffusion-weighting direction) and a single-shot fast spin-echo (FSE) pulse sequence (TR = 1.4 s, TE = 80 ms, FOV = 25.6 x 12.8 cm, matrix size = 256 x 128, slice thickness = 4 mm), respectively.

In addition, to demonstrate the shimming performance of the iPRES-W coil array in comparison to other shim methods, ΔB_0 maps were simulated for: global 2nd-order SH shimming, slice-optimized 2nd-order SH shimming, and a combination of slice-optimized iPRES-W and 2nd-order SH shimming. The nine basis ΔB_0 maps corresponding to the 0th- to 2nd-order SH terms were analytically calculated and their DC currents were not constrained. Slice-optimized shimming was performed in the same ROI and the same slab of 3 slices as in the experiments, whereas global shimming was performed in a larger rectangular volume, which included the whole ROI and spanned 7 slices to cover the spinal cord.

3.4.4 iPRES-W Coil Wireless Antenna Performance

During MR image acquisition, the iPRES-W coil array was placed under the subject and close to the surface of the neck to maximize SNR and wireless shimming performance in the cervical spinal cord. To investigate the impact human tissue would

have on the wireless performance of the iPRES-W coil element, an anechoic chamber (section 2.2.3) was used to measure the radiated power emitted by the coil with and without a 250-mL saline phantom (i.e., human tissue equivalent) placed directly on the loop. Each radiated power measurement was performed by recording the isolation (S_{21}) between two ports of a calibrated VNA (section 2.2.1), which was connected to the iPRES-W coil and a receive patch antenna placed within the calibrated chamber (Fig. 3.9a).

The wireless performance of the coil, which is determined by its radiation efficiency and radiation pattern, was characterized by performing a set of radiated power measurements in the chamber over the entire solid angle of a sphere using 10-degree steps for both the polar and azimuthal directions (θ, φ). First, the WiFi radiation efficiency was calculated by performing a numerical integration over the sphere of the ratio between the radiated power from the coil received by the patch antenna and the

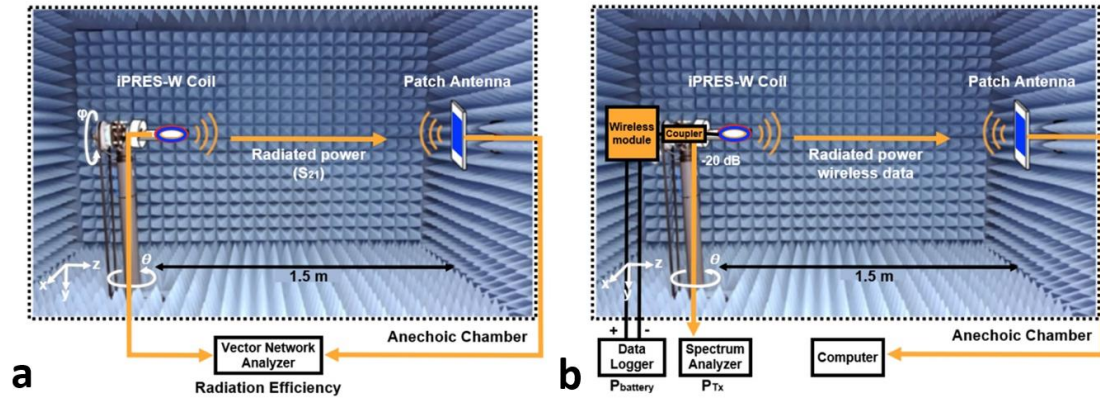


Figure 3.9: Radiation efficiency and radiation pattern measurements of an iPRES-W coil in an anechoic chamber using a VNA (a). Wireless transmit power and battery consumption measurements during wireless data transfer to a computer outside the chamber using a spectrum analyzer and a data logger (b).

input power to the coil provided by the VNA. Second, the radiation pattern was generated by plotting the radiated power for each angle to show its spatial distribution relative to the coil. These measurements were repeated with and without (i.e., free-space measurement) the phantom placed on the coil to determine its impact on the radiation efficiency and pattern.

These measurements were made in an anechoic chamber to remove any external influences and are not possible while the iPRES-W coil array is within the scanner. However, an additional radiated S_{21} measurement of the iPRES-W coil element was acquired in the scanner bore, with and without a subject laying on the coil array and with the receive antenna placed in the same position relative to the iPRES-W coil element as it was in the anechoic chamber, to determine any impact that a subject would have on the wireless radiation efficiency and to validate the chamber measurements.

3.4.5 iPRES-W Coil Battery Power Consumption

The presence of a subject close to the iPRES-W coil element or in between the coil and AP can potentially attenuate the radiated power coupled between the two antennas. If this occurs, the wireless module will compensate for the loss by increasing the transmit power (ΔP_{Tx}) and thus increasing the power drawn from the battery ($\Delta P_{battery}$). The battery power consumption of an iPRES-W coil was therefore measured to evaluate the attenuation of the radiated power from the coil in the WiFi frequency band caused by the introduction of a saline phantom (Fayad (2005) and O’Keefe (2007)). ΔP_{Tx} and

$\Delta P_{\text{battery}}$ were measured simultaneously in the anechoic chamber with a spectrum analyzer and a data logger, respectively, while wirelessly transferring data using IEEE 802.11b and a rate of 6 Mbps to a computer located outside the chamber (Fig. 3.9b). For the ΔP_{Tx} measurement, a directional coupler was added between the wireless module and the coil to direct only -20 dB of conducted power from the module to the spectrum analyzer and therefore not attenuate the wireless power transferred. For the $\Delta P_{\text{battery}}$ measurement, the data logger was used to measure both the average and standard deviation of the battery current and voltage from the wireless module. These measurements were conducted with the coil positioned at the polar and azimuthal angles determined by the aforementioned antenna measurements with the highest ($\theta = 190^\circ$, $\varphi = 30^\circ$) and lowest ($\theta = 130^\circ$, $\varphi = 0^\circ$) amount of radiated power emitted from the coil. ΔP_{Tx} and $\Delta P_{\text{battery}}$ were measured with and without the saline phantom on the iPRES-W coil to determine its impact. Finally, P_{battery} was measured on the benchtop for P_{Tx} values ranging from 0 to 25 dBm in 1-dB increments to determine their baseline relationship with no iPRES-W coil connected.

3.5 Results

3.5.1 Temperature Measurements

After the maximum DC current of 1.3 A was continuously applied to all four coil elements for 10 minutes, the increase in temperature for each component from room temperature (22.2°C) was: 1) 22.9°C for the 3D-printed battery case, 2) 25.9°C for the

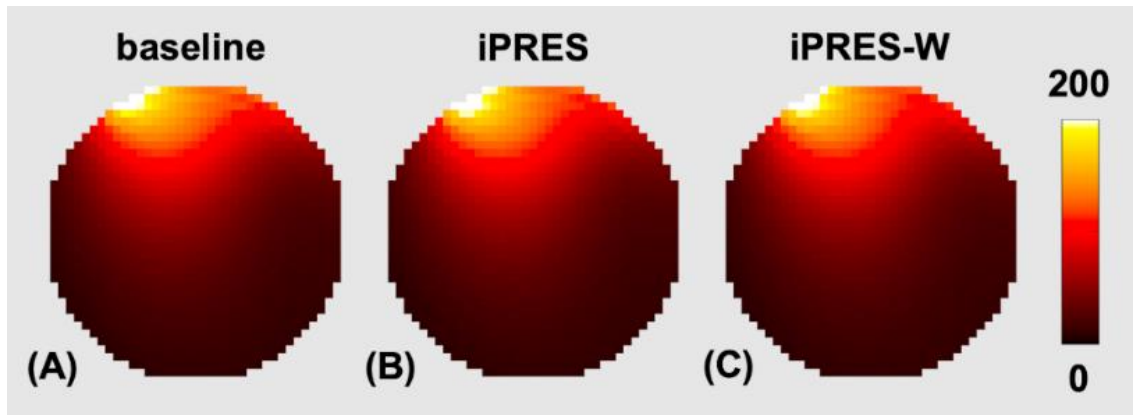


Figure 3.10: The acquired SNR maps in a water phantom using a single AIR™ coil element show no SNR degradation from the baseline coil configuration (a) to the iPRES (b) and iPRES-W (c) coil configurations.

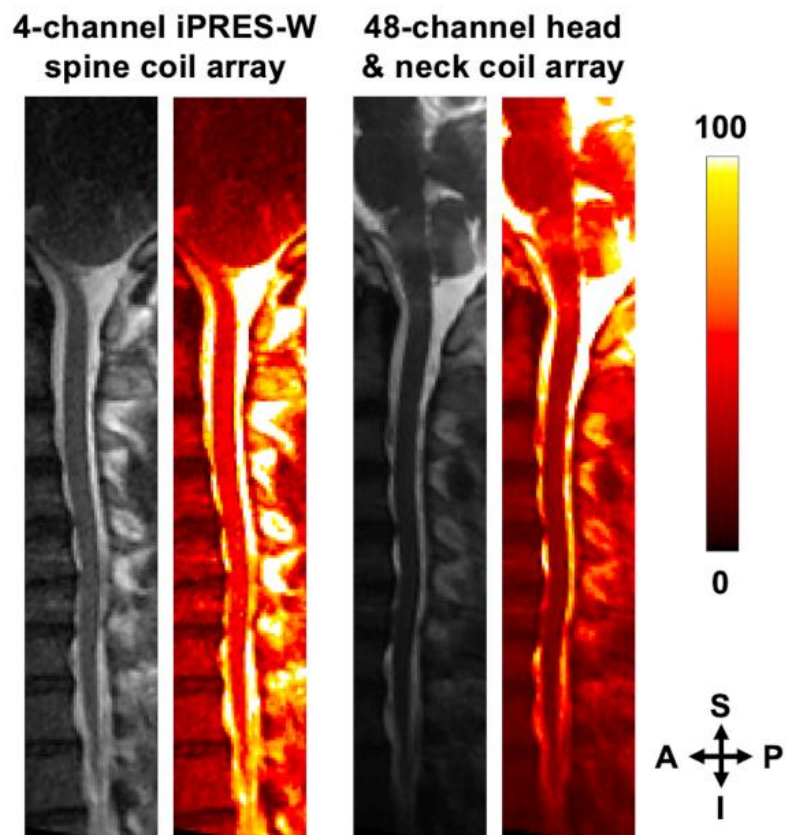


Figure 3.11: Sagittal anatomical images and SNR maps of the cervical spinal cord with the 4-channel iPRES-W spine coil array or the 48-channel head and neck coil array, show a comparable SNR in the spinal cord and brainstem/cerebellum, respectively.

wireless module, 3) 78.2 °C for the op-amp, 4) 23.4 °C for the batteries, 5) 22.9 °C for the 3D-printed coil structure, 6) 23.4 °C for the iPRES-W coil element, and 7) 26.0 °C for the iPRES-W PCB (Fig. 3.8b). The op-amp was the only component which had a significant increase in temperature; however, there was no safety risk to the subject or electronics as 1) the heat increase was dissipated via heat sinks and did not spread to the nearby batteries, wireless module, or battery case, 2) the battery pack was placed away from the subject, and 3) the final temperature stayed well below the maximum operating temperature for the op-amp (125 °C).

3.5.2 SNR Measurements

The acquired SNR maps in the phantom for a single AIR™ coil element show minimal difference after the coil element was modified from the baseline coil configuration (Fig. 3.10a) to the iPRES (Fig. 3.10b) and iPRES-W (Fig. 3.10c) coil configurations, which had SNR values averaged over the entire phantom of 118.7, 119.3, and 118.2, respectively. Additionally, SNR maps acquired in the cervical spinal cord using the 4-channel iPRES-W spine coil array or a 48-channel head and neck coil array show comparable SNR in the regions for which each coil array is designed to image (Fig. 3.11).

3.5.3 DTI of the Cervical Spinal Cord with Wireless Localized Shimming

The four basis ΔB_0 maps acquired in the phantom show the localized magnetic field generated by each iPRES or iPRES-W coil element at different locations along the cervical spinal cord (Fig. 3.12). The maximum DC current of 1.3 A can generate a maximum ΔB_0 field offset of 134 Hz in the spinal cord. After only 1st-order shimming, magnetic susceptibility differences near air/tissue interfaces still induced strong

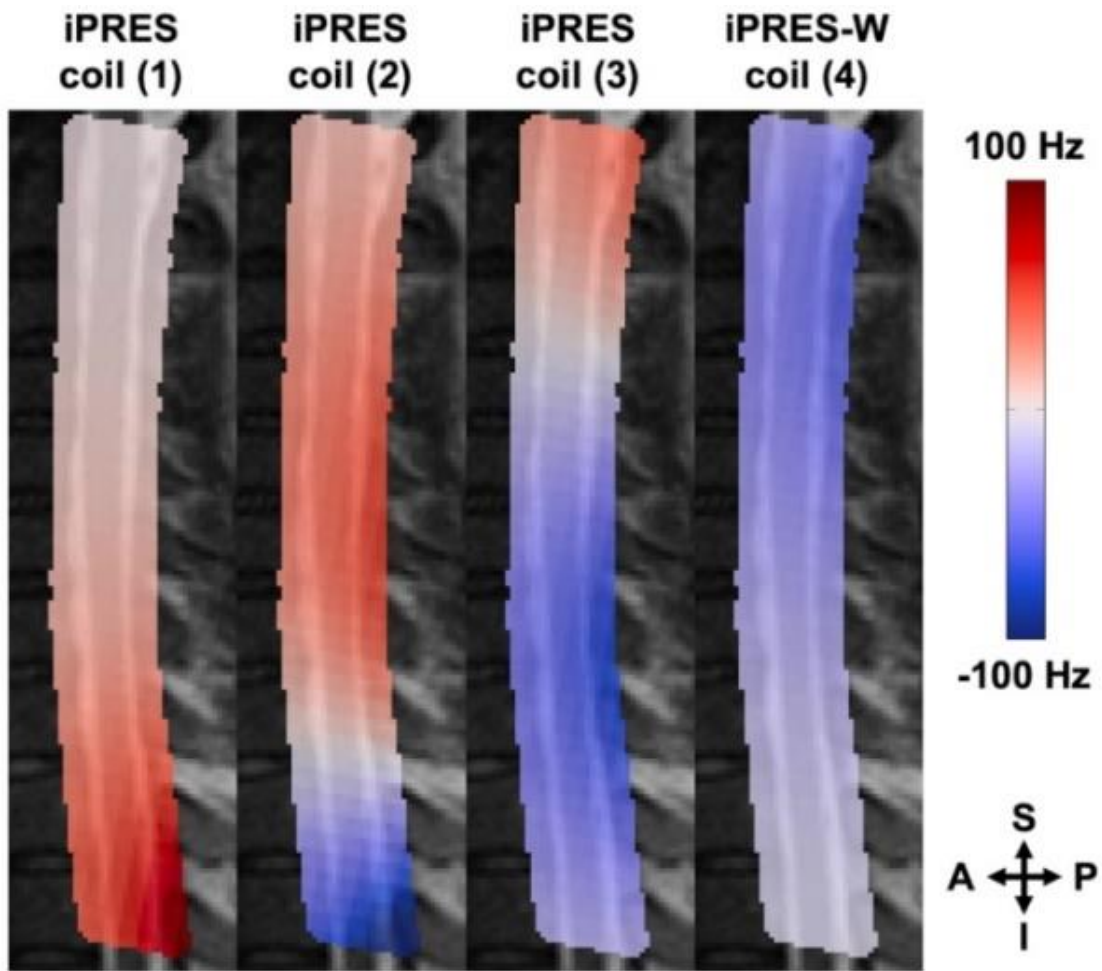


Figure 3.12: Basis ΔB_0 maps acquired in a water phantom with a DC current of 1 A successively applied to each iPRES or iPRES-W coil element, overlaid on a sagittal anatomical image of the cervical spinal cord of subject 1.

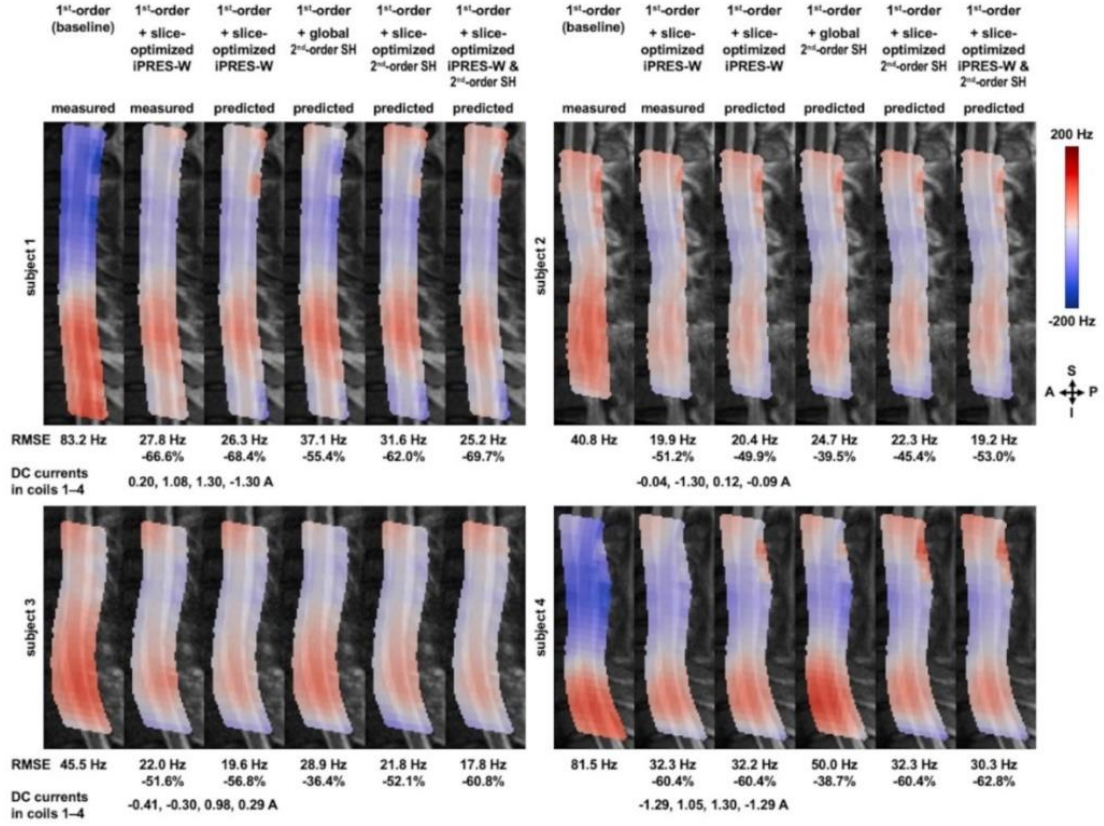


Figure 3.13: Sagittal ΔB_0 maps in an ROI drawn around the cervical spinal cord of each subject, overlaid on an anatomical image, after shimming with the different methods shown at the top. The corresponding B_0 RMSE in the ROI and its reduction relative to the baseline are shown under each map as well as the DC currents applied in coils 1-4 for the iPRES-W shimming.

localized B_0 inhomogeneities throughout the cervical spinal cord (Fig. 3.13, baseline).

After performing wireless localized B_0 shimming with the iPRES-W coil array, the B_0

RMSE in the ROI was drastically reduced (by -57.5% (measured) or -58.9% (predicted)

when averaged across all subjects). The predicted reduction in B_0 RMSE in the ROI

increased from global 2nd-order SH shimming (-42.5%) to slice-optimized 2nd-order SH

shimming (-55.0%), then slice-optimized iPRES-W shimming (-58.9%), and finally slice-

optimized iPRES-W and 2nd-order SH shimming (-61.6%), as expected.

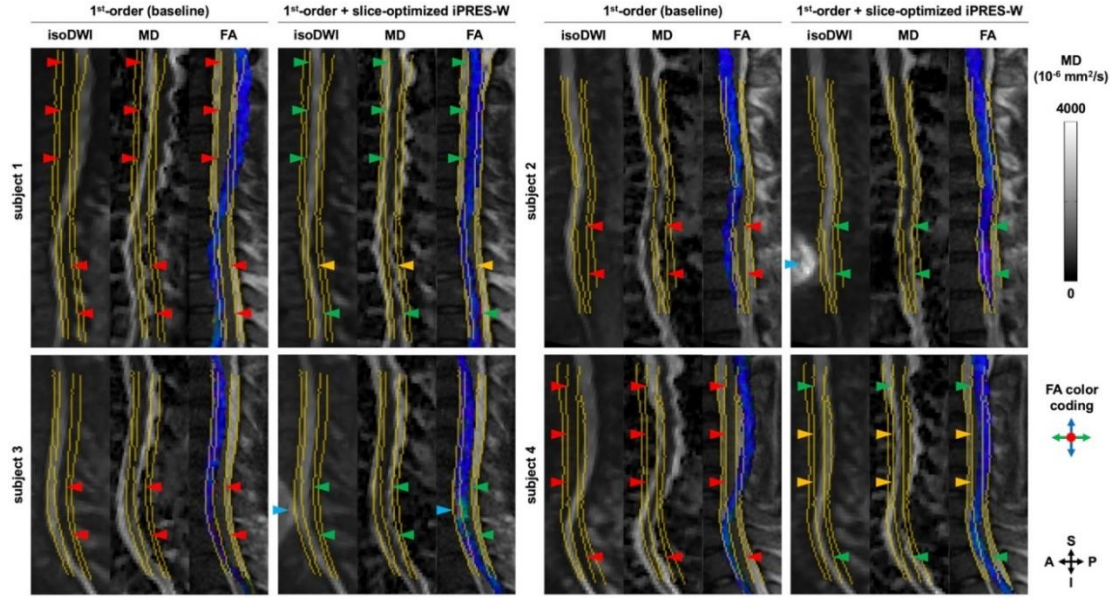


Figure 3.14: Sagittal isoDWI images, MD maps, and FA maps overlaid on an anatomical image of the cervical spinal cord, showing severe distortions induced by localized B_0 inhomogeneities after only 1st-order shimming (as highlighted by the red arrowheads and the misalignment with the overlaid yellow contour lines derived from the anatomical images), but substantially reduced distortions and improved anatomical registration for all subjects after shimming with the iPRES-W coil array (as highlighted by the green arrowheads).

The baseline isoDWI images, MD maps, and FA maps all show severe geometric distortions relative to the contour lines derived from the undistorted anatomical images (Fig. 3.14, red arrowheads). After shimming with the iPRES-W coil array, these distortions were drastically reduced for all subjects (Fig. 3.14, green arrowheads). For subjects 1 and 4, who had more severe B_0 inhomogeneities in their baseline ΔB_0 map, some of the DC currents used for shimming were limited by the maximum DC current amplitude of 1.3 A, so residual distortions remained after shimming (Fig. 3.14, yellow arrowheads), but they were still substantially reduced relative to the baseline. For subjects 2 and 3, the strong localized ΔB_0 field offsets generated by some of the iPRES or

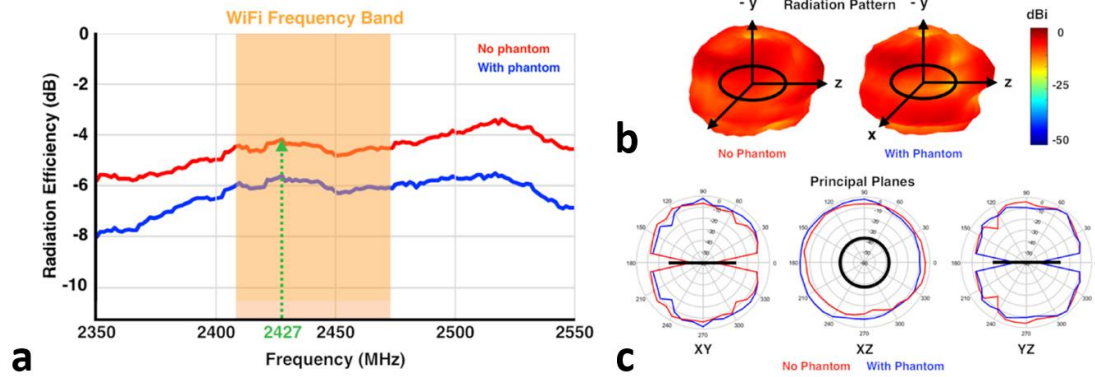


Figure 3.15: Antenna radiation efficiency (a) of the iPRES-W coil, showing a decrease of in-band peak efficiency (green arrow) of only 1.4 dB with the saline phantom placed on the coil (blue line) relative to free space (red line). Radiation patterns (b) and corresponding radiated power in the principal planes (c) of the iPRES-W coil, showing only minimal changes with (blue line) vs. without (red line) the saline phantom placed on its loop.

iPRES-W coil elements caused nearby tissue posterior to the spinal cord to wrap around the FOV (Fig. 3.14, cyan arrowheads) and, for subject 3, to overlap with the spinal cord, resulting in an artifact in the FA map. However, this issue can be addressed by using a slightly wider FOV in the phase-encoding direction.

3.5.4 iPRES-W Coil Wireless Antenna Performance

The antenna radiation efficiency and radiation pattern measurements performed in the anechoic chamber show that the saline phantom only minimally attenuated the amount of radiated power emitted from the iPRES-W coil. The peak radiation efficiency of the coil in the WiFi frequency band was -4.2 dB in free space and only decreased by 1.4 dB with the saline phantom placed on the coil (Fig. 3.15a, green arrow). Additionally, the radiation patterns with and without the phantom were similar in shape (Fig. 3.15b)

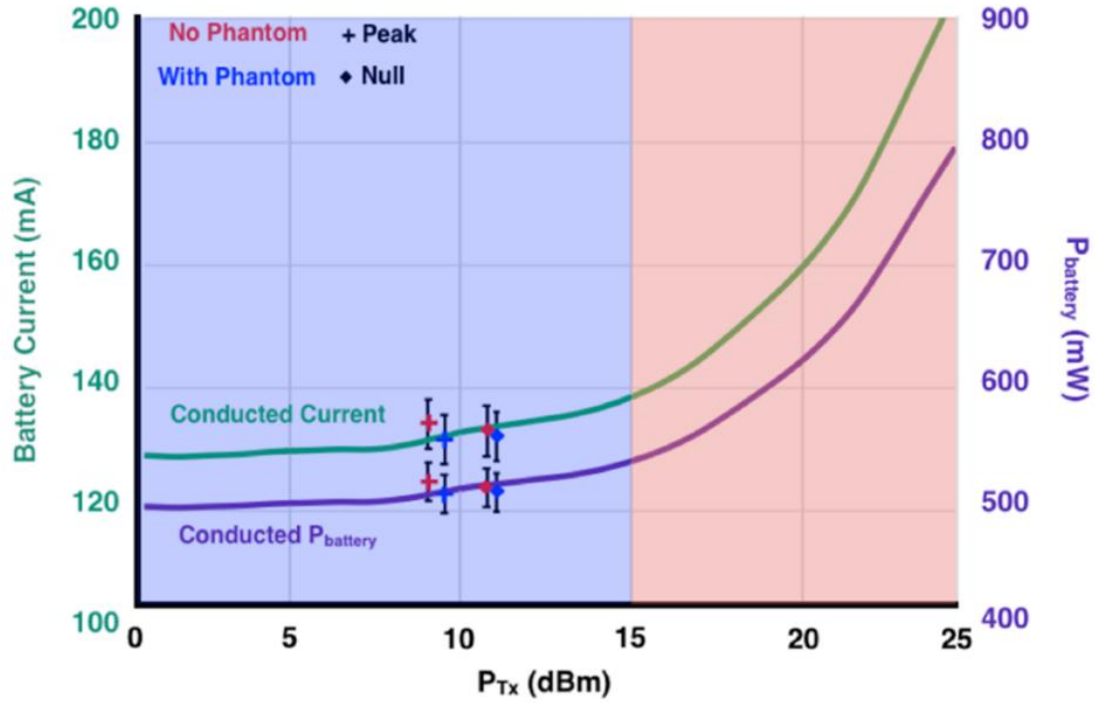


Figure 3.16: $P_{battery}$ and P_{Tx} measurements with the iPRES-W coil, showing only changes of less than 10 mW and 1.8 dB, respectively, with the introduction of the saline phantom (blue data points) for both the null (♦) and peak positions (+). The $P_{battery}$ and corresponding battery current standard deviations of 4 mW and 15 mA show that these measurements performed in the anechoic chamber are in good agreement with the $P_{battery}$ (purple line) and battery current (green line) measurements performed on the benchtop.

and in amplitude in the principal planes (Fig. 3.15c). For example, the radiated power in the XY, XZ, and YZ-planes only decreased by an average of 1.7, 0.5, and 0.4 dB, respectively, with the phantom placed on the coil. Finally, the radiated S_{21} measurement of the iPRES-W coil element performed within the MRI scanner bore also only showed a small decrease of 3.1 dB with the subject laying on the iPRES-W coil array.

3.5.5 iPRES-W Coil Battery Power Consumption

The power measurements performed in the anechoic chamber with the iPRES-W coil placed at either the null or peak position show that the saline phantom only caused an average battery current and P_{battery} increase of less than 3 mA and 10 mW, respectively, which corresponded to a P_{Tx} increase of only 1.8 dB (Fig. 3.16). Altogether, Figures 3.15 and 3.16 show that the introduction of a saline phantom onto the iPRES-W coil did not significantly change the antenna radiation efficiency, radiation pattern, or P_{battery} .

3.6 Discussion

In this work, we proposed a novel 4-channel iPRES-W coil array for simultaneous imaging and wireless localized B_0 shimming of the cervical spinal cord. The temperature measurements showed that there was no safety risk to the subject or electronics. Additionally, the SNR measurements showed that the modifications made to implement the iPRES and iPRES-W coil elements did not degrade the SNR, as in previous implementations (Truong (2014), Darnell (2017), Darnell (2018), Ma (2018), and Darnell (2019)). The in vivo B_0 shimming experiments showed that the 4-channel iPRES-W coil array could perform wireless localized B_0 shimming and substantially reduce the B_0 inhomogeneities and geometric distortions in the DTI images of the cervical spinal cord of all subjects, without requiring any scanner modifications or additional antenna systems within the scanner bore. Lastly, the antenna and power measurements showed

that the radiated power emitted from the iPRES-W coil, and hence its wireless performance and battery power consumption, were all minimally impacted when a saline phantom representing tissue was placed on it.

Previous in vivo studies at 3T using a 24-channel MC shim array covering the whole spinal cord (Topfer (2016)) or an 8-channel iPRES coil array (also referred to as an integrated $\Delta B_0/R_x$ coil array) covering the neck region (Topfer (2018a)) reported an average reduction in B_0 RMSE in the spinal cord from 85.8 to 29.1 Hz (-66.1%) or from 53.3 to 30.4 Hz (-43.0%), respectively. In the work presented here, the 4-channel iPRES-W coil array was able to reduce the B_0 RMSE in the cervical spinal cord from 62.8 to 25.5 Hz (-57.5%) when average across all subjects but, using a wirelessly controlled battery pack rather than a wired DC power supply. However, these results are not directly comparable, since the B_0 shimming performance depends not only on the coil geometry, but also on other factors such as the subject's anatomy and breathing pattern or the ROI used for shimming, which were all different across these studies.

One of these previous studies (Topfer (2016)) further reported that the B_0 inhomogeneity in the spinal cord was reduced to 36.1 Hz (-57.9%) on average with global 2nd-order SH shimming of the spinal cord, which is somewhat worse than when shimming with the 24-channel MC shim array. In the present work, the predicted B_0 RMSE in the cervical spinal cord was reduced to 35.2 Hz (-42.5%) or 27.0 Hz (-55.0%) on average with global or slice-optimized 2nd-order SH shimming, respectively, which is also somewhat worse than the predicted B_0 RMSE of 24.6 Hz (-58.9%) achieved when

shimming with the iPRES-W coil array. The predicted B_0 RMSE in the cervical spinal cord was further reduced to 23.1 Hz (-61.6%) on average with slice-optimized iPRES-W and 2nd-order SH shimming, providing better results than either iPRES-W or 2nd-order SH shimming alone, as expected.

A notable difference between these studies is that our proof-of-concept iPRES-W coil array with 4 coil elements covering the neck was only used to shim the cervical spinal cord, whereas the 24-channel MC shim array was used to shim the larger thoracic portion of the spinal cord, which contains more extensive B_0 inhomogeneities. In future work, however, the shimming performance of the iPRES-W coil array could be further improved by 1) increasing the number, reducing the size, and/or extending the coverage of the coil elements, 2) modifying the battery pack design to increase the range of DC currents for shimming, or 3) dynamically shimming the respiration-induced ΔB_0 fluctuations (in addition to the static B_0 inhomogeneities shimmed in this work), which has been done with a 24-channel MC shim array (Topfer (2018a)) and an 8-channel iPRES coil array (Topfer (2019)), but using a wired DC power supply rather than a wirelessly-controlled battery pack. In the later case, the iPRES-W coil array could be used to wirelessly transmit data from a respiratory belt (Cuthbertson (2020)) to a computer in the console room to dynamically update the optimal DC currents for shimming (e.g., depending on whether the subject is inspiring or expiring), which would then be wirelessly transmitted back to the iPRES-W coil array to adjust the DC currents applied to the coil elements.

The saline phantom placed on the iPRES-W coil used in this work represents a worst-case radiated power attenuation scenario, because saline has a dielectric loss factor that is approximately twice that of human tissue in the WiFi frequency band (Vallejo (2013), Haukalid (2016), and Gu (2017)). Additionally, the radiated power attenuation occurs largely near the phantom/coil interface for these frequencies (Vallejo (2013)), because the 3-cm thick phantom behaves as an electrically homogenous dielectric medium for penetration depths greater than ~2 cm. Finally, even with the introduction of the phantom and with the iPRES-W coil placed at either the null or peak position, the P_{battery} from the wireless module remained in the linear P_{Tx} region of the module (Fig. 3.16, blue region). In contrast, P_{Tx} values in the non-linear region (Fig. 3.16, pink region) would have substantially increased P_{battery} , which would have in turn drastically reduced the wireless module battery life. As such, since the saline phantom used in this work only had minimal impact on the iPRES-W coil radiation efficiency, radiation pattern, and P_{battery} , these results are still expected to hold for a human subject.

4. Aim 2: The Dual-Stream iPRES-W Head Coil Array

4.1 Introduction

The second aim of this dissertation is to remove the cables required to transfer data for the peripheral devices (e.g., physiological monitors and motion tracking systems). To fully eliminate the conventional cable assemblies required for data transfer in MRI, the implemented wireless antenna system must be able to transfer multiple independent data streams both into and out of the scanner bore. The previously proposed wireless systems for MRI (section 1.3.1), cannot easily provide multiple independent data stream as each device would require additional hardware and transmit/receive antennas to be added within the scanner bore (Bulumulla (2015) and Aggarwal (2017)). In this work, these limitations are addressed by implementing two iPRES-W coil elements into a 48-channel head coil array, which will enable multiple independent wireless data streams for two separate applications, specifically, to wirelessly 1) control the DC currents used for localized B_0 shimming and 2) perform respiratory tracking with a respiratory belt.

As mentioned in section 1.3.2, susceptibility differences lead to local B_0 inhomogeneities, which if not corrected for, have adverse effects on image quality and limit the usefulness of several MR imaging techniques. For example, EPI imaging allows for very fast image acquisition compared to conventional MR imaging, which reduces motion artifacts and allows for capture of rapid physiological processes in the human body, such as the evaluation of a stroke (Meshkar (2014)) or the blood oxygenation level-

dependent (BOLD) signal in the brain used in fMRI (Kirilina (2016)). However, magnetic susceptibility differences, primarily at the air/tissue interface near the frontal sinus cavity, cause localized B_0 inhomogeneities in the inferior frontal brain region, which can result in geometric distortions and/or signal loss (Willey (2021)). Similar to the localized B_0 inhomogeneities in the spinal cord (section 3.1), these cannot be corrected for using traditional whole-body 2nd-order SH shim coils. Previously investigated alternative methods to shim highly localized inhomogeneities in the brain using MC shimming have shown promising results but require separate RF and shim coils, which take up space within the scanner bore and can degrade either SNR or shimming performance (Juchem (2011b)). The iPRES coil design addresses this limitation by combining both functions onto a single coil element (Willey (2021)), however, both MC and iPRES coil arrays require additional DC wires, RF filters, and cable traps for shimming, which take up space within the bore and increase the cost and complexity of the system. In this work, we address these limitations and reduce the number of wired connections by integrating the iPRES-W coil design into a 48-channel head coil array for wireless localized B_0 shimming of the brain in vivo. To demonstrate that the dual-stream iPRES-W head coil array has the ability to perform simultaneous MR image acquisition and wireless data transfer for multiple independent data streams, EPI images are acquired during wireless localized B_0 shimming and wireless respiratory tracking. Preliminary results have been presented in abstract form (Cuthbertson (2020)).

4.2 RF Coil Modifications

4.2.1 iPRES Coil Design Implementation

The 48-channel head coil array was divided into two halves, with 16 anterior coils elements and 32 posterior coil elements. First, the 16 anterior coil elements of a 48-channel head coil array (Fig. 4.1) were modified into iPRES coil elements by adding inductive chokes ($L_{\text{choke}}^{127 \text{ MHz}} = 820 \text{ nH}$, $R_{\text{DC}} = 0.02 \Omega$) between each coil element and an MR-compatible battery pack (section 3.3) placed inside the scanner bore, which provided the adjustable DC currents for localized B_0 shimming (Fig. 4.2, blue). Similar to the iPRES-W spine coil array (section 3), these chokes prevented the RF currents at 127 MHz from flowing into the battery pack ($S_{21}^{127 \text{ MHz}} = -25 \text{ dB}$), which would reduce the MR signal amplitude and SNR. Unlike the previous 4-channel iPRES-W spine implementation, which used AIR coil elements and had no capacitors around the coil perimeter, the 48-channel head coil array used conventional coil elements. As such, additional inductors ($L_{\text{bypass}} = 820 \text{ nH}$, $R_{\text{DC}} = 0.02 \Omega$) were added to each coil element to bypass the capacitors located around the coil perimeter (Fig 4.2, C), which enabled the DC current for shimming to flow on the coil structure.

Next, simulations were performed to determine the optimal number and location of anterior iPRES coil elements to achieve an optimal trade-off between the localized B_0 shimming performance in the brain and number of individual shim currents provided by the wireless battery pack, which was limited to four in this initial proof-of-concept implementation. First, ΔB_0 maps were acquired in a water phantom with a DC current

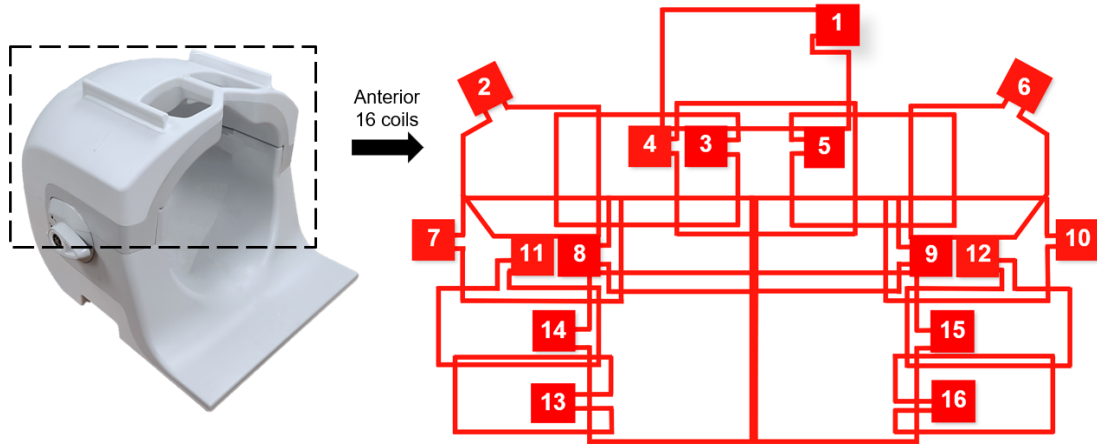


Figure 4.1: Modifications were implemented onto the anterior 16 coil elements (black dashed box) of a 48-channel head coil array for a Premier 3T GE scanner (left). A 2D schematic shows the relative placement and coil numbering of the anterior RF coil elements (right).

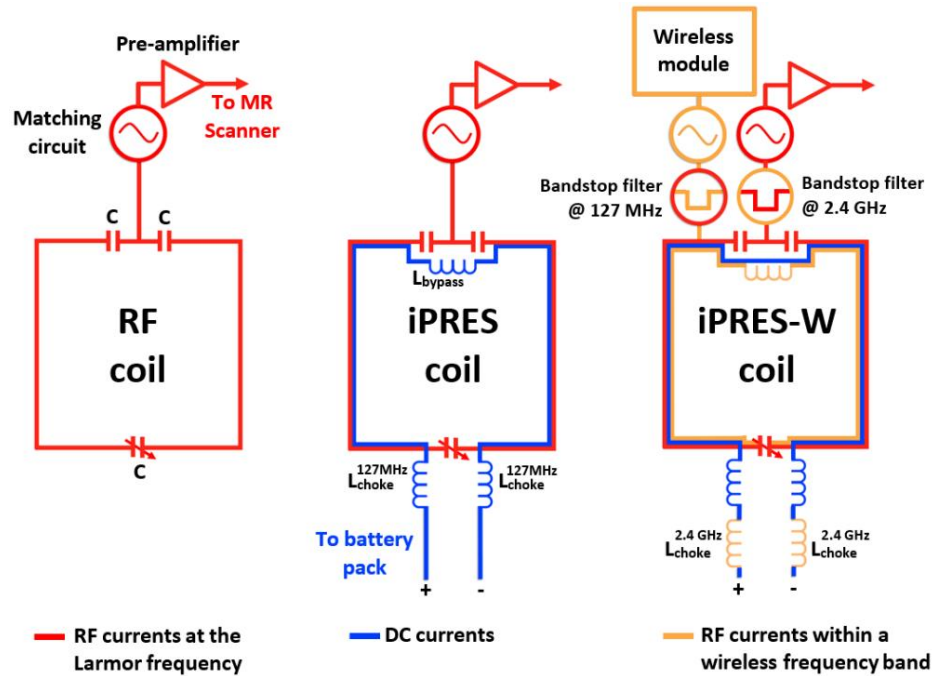


Figure 4.2: Modifications began with a conventional RF coil element (red), which was then modified into an iPRES coil element for simultaneous imaging and localized B_0 shimming by enabling a DC current to flow on the coil element (blue). Next, the iPRES coil element was modified into an iPRES-W coil element for simultaneous imaging, shimming, and wireless data transfer by enabling an RF current within a wireless frequency band to flow on the coil element (orange).

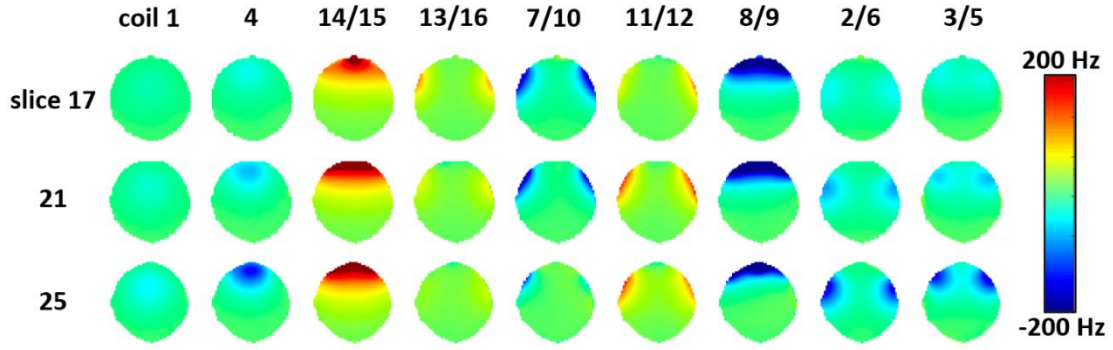


Figure 4.3: Basis ΔB_0 maps for the symmetrical and non-symmetrical iPRES coil elements acquired on a water phantom for three slices (17, 21, and 25).

of 1 A applied to each of the sixteen iPRES coil elements using a multi-echo GRE sequence (section 3.4.3) after applying 1st-order shimming from the scanner. A ΔB_0 map was also acquired with no DC currents and was then subtracted from each of these ΔB_0 maps, which resulted in a set of sixteen basis ΔB_0 maps representing the magnetic field per unit current generated by each iPRES coil element. Since the B_0 inhomogeneities in the brain are mostly symmetrical in the right/left direction, pairs of symmetrical coil elements (e.g., Fig. 4.1 coils 13/16 or coils 2/6) were connected in series and their individual basis ΔB_0 maps combined, which resulted in a set of nine basis ΔB_0 maps for the seven pairs of symmetrical coil elements (coils 2/6, 3/5, 7/10, 8/9, 11/12, 14/15, and 13/16) and the two non-symmetrical coil elements (coils 1 and 4) (Fig. 4.3). Given the limited number of DC current outputs from the battery pack, applying the same DC currents to symmetrical coil elements enabled a larger number of coil elements to be used for shimming, resulting in an improved shimming performance. Next, a ΔB_0 map was acquired in the brain of a healthy volunteer and the optimal DC currents to shim the brain as well as the residual B_0 RMSE after shimming were calculated for each of the 126

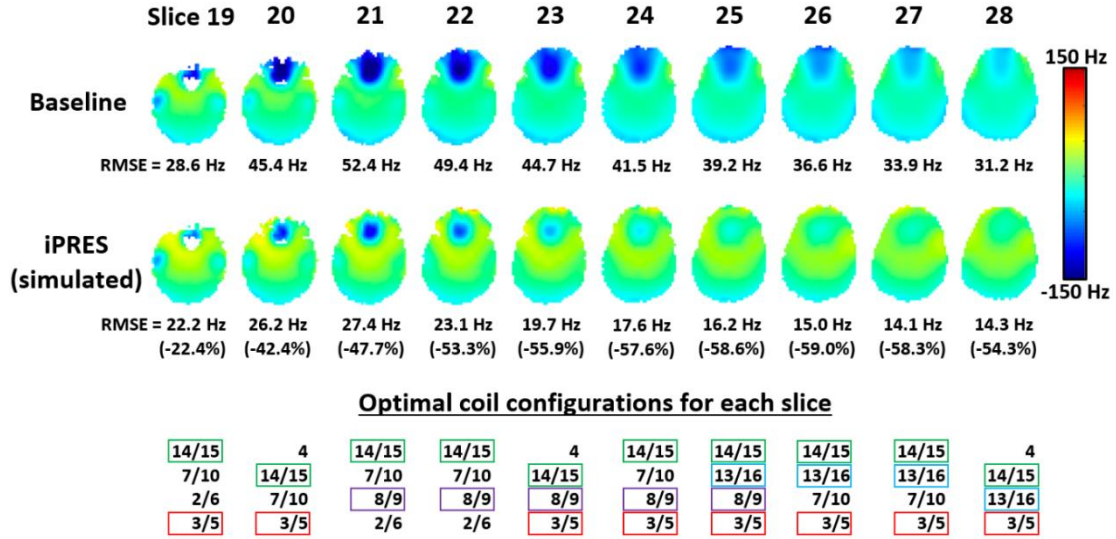


Figure 4.4: While the optimal iPRES coil combinations were different for different slices, there were two combinations that were best for a majority of the slices (coils 14/15; green and coils 3/5; red) and two additional combinations that were best over slices (23-25) with a large RMSE reduction (coils 13/16; blue and coils 8/9; purple).

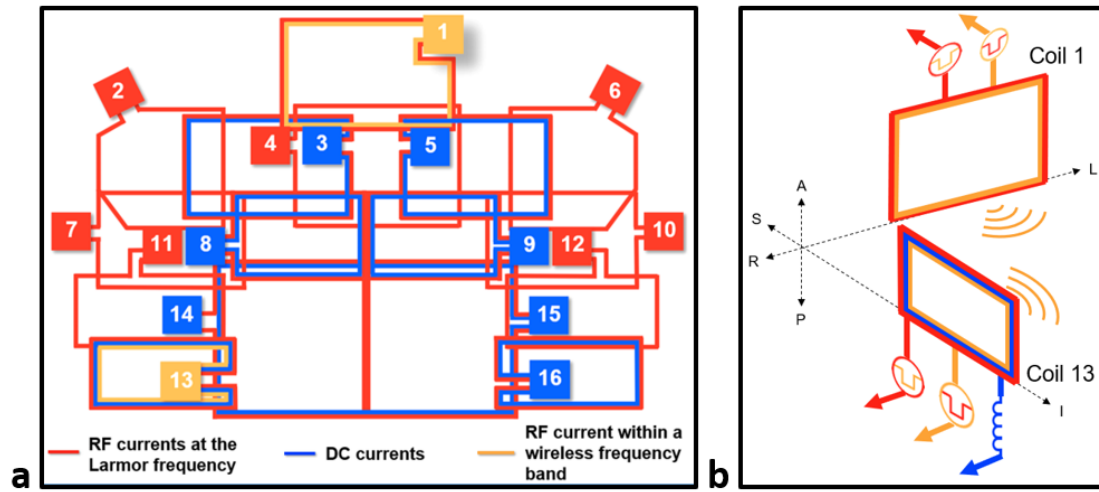


Figure 4.5: Schematic of the modified 16 anterior coil elements (a) showing the placement of the 8 iPRES coil elements connected to the wireless battery pack, which provided the DC shim currents (blue), and the two iPRES-W coil elements (orange) to enable the dual-stream wireless data transfer. The iPRES-W coil elements were chosen to be spatially orthogonal to each other to ensure high signal isolation (b).

possible combinations of 4 out of the 9 basis (i.e., $C(9,4) = \frac{9!}{4!(9-4)!} = 126$). Finally, for each of these 126 combinations and each of the 10 slices acquired through the inferior frontal brain region, the shim optimization was performed by minimizing the B_0 RMSE between the ΔB_0 map acquired in the subject and a linear combination of the basis ΔB_0 maps acquired in the phantom, which was performed in MATLAB (*fmincon* function) and with the DC currents constrained within a range of ± 2 A. Based on the results (Fig. 4.4), the optimal coil elements were determined to be the four coil pairs 3/5, 8/9, 14/15, and 13/16, which were connected to the wireless battery pack (Fig. 4.5a, blue).

4.2.2 iPRES-W Coil Design Implementation

Two of the coil elements, coils 1 and 13, were further modified into iPRES-W coil elements, as described in section 3.2, by inserting a low-loss high impedance bandstop filter tuned to resonate at 127 MHz between each coil element and their respective wireless modules (Fig. 4.6, orange, coils 1 and 13). Additionally, a second low-loss high-impedance bandstop filter tuned to resonate at 2.4 GHz (Fig. 4.6, red, coils 1 and 13) was placed between each coil element and their respective MRI preamplifier. The two iPRES-W coil elements were chosen to be spatially orthogonal to provide a high RF-isolation ($S_{21} \sim -35$ dB) between them and ensure that the wireless signal from the iPRES-W coil elements did not couple to one another, which would cause signal interference, noise, and reduce the amount of power radiated from each coil element in the WiFi frequency band (Fig. 4.5b). Additionally, the 2.4 GHz channel for each wireless module, connected

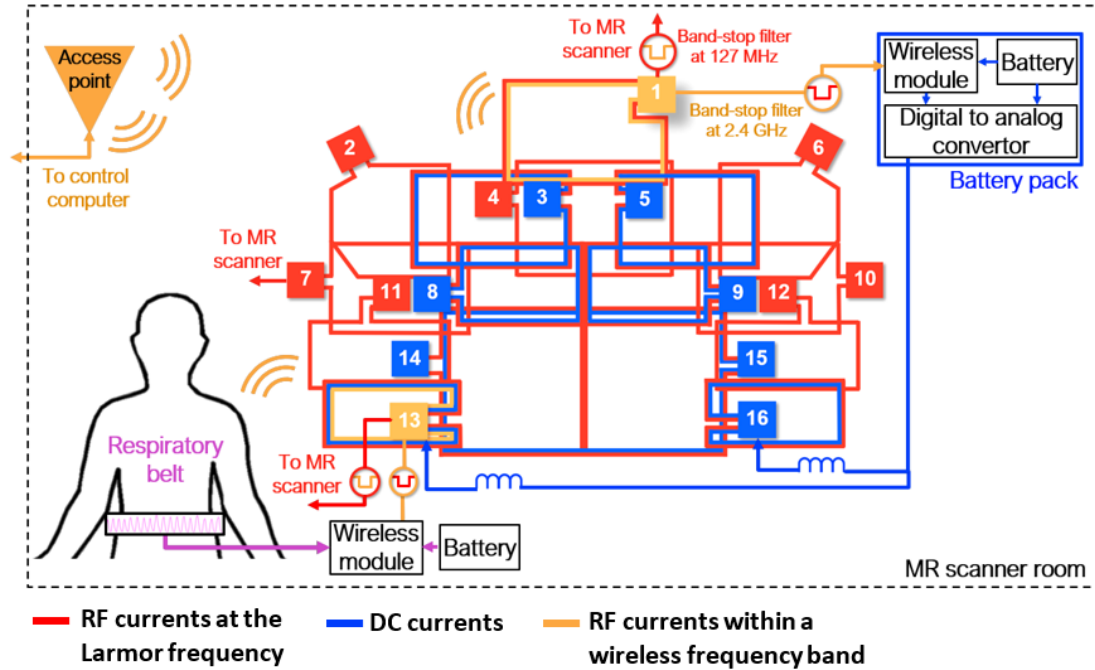


Figure 4.6: Diagram of the dual-stream iPRES-W head coil array for simultaneous MR image acquisition (RF currents at 127 MHz; red) and wireless data transfer (RF currents within a wireless communication band; orange) for two independent applications, specifically, wireless localized B_0 shimming (DC currents; blue) and wireless respiratory tracking with a respiratory belt (analog respiratory signal; purple).

to the two iPRES-W coil elements, were manually set to channels 1 and 11, respectively, to allow for virtually no overlap in the WiFi signal (Fig. 4.7). The first iPRES-W coil element, coil 1, was used to wirelessly control the DC shim currents supplied from the battery pack to the eight iPRES coil elements (i.e., four pairs of symmetrical coil elements). Specifically, TCP/IP and serial commands were sent from a computer in the console room to the wireless module of the first iPRES-W coil element via the wireless connection between that coil element and the AP placed along the scanner room wall (Fig. 4.6, orange triangle). The second iPRES-W coil element, coil 13, was used to perform real-time wireless respiratory tracking during MR image acquisition and

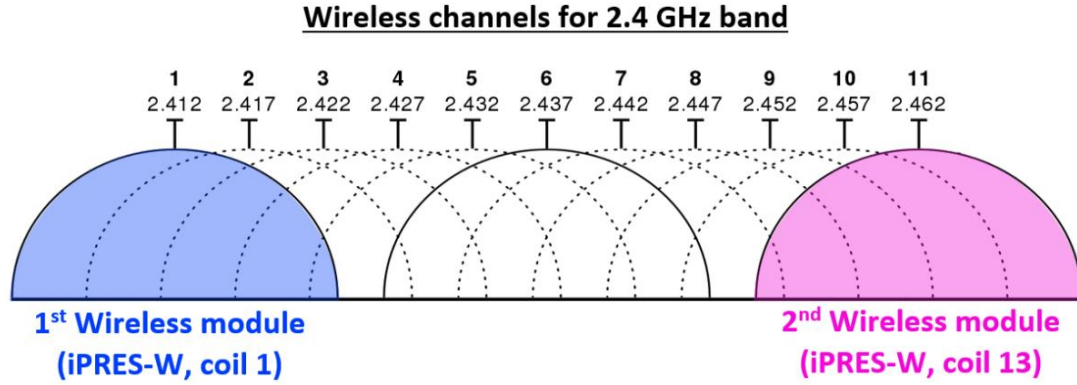


Figure 4.7: The 2.4 GHz WiFi frequency band (2.412-2.472 GHz) consists of 11 different channels, each with a 5 MHz bandwidth. The two wireless modules, connected to the two iPRES-W coil elements, were set to channels 1 and 11 to avoid signal interference.

localized B_0 shimming. Specifically, a force-sensitive respiratory belt was placed around the subject's abdomen and its signal was first digitized by the second iPRES-W coil element's wireless module ADC (Fig. 4.6, purple), then wirelessly transmitted from that coil element to the AP, and finally recorded and displayed on a computer located outside the scanner room.

4.3 Experimental Setup and Tests

4.3.1 SNR Measurements

To demonstrate that the iPRES and iPRES-W coil modifications did not degrade the image quality, SNR maps were acquired in a water phantom with the 48-channel head coil array in four different configurations: 1) baseline, 2) iPRES (16 modified iPRES coil elements with 8 connected to the battery pack), and iPRES-W (coils 1 and 13) 3) without and 4) while providing simultaneous wireless transmission of the respiratory

signal and localized B_0 shim control commands. The SNR maps were acquired with the same GRE pulse sequence used in section 4.4.2.

4.3.2 MR Imaging with Wireless Shimming and Respiratory Tracking

In a second experiment, spin-echo EPI images and ΔB_0 maps were acquired in the brain of a healthy volunteer with the dual-stream iPRES-W head coil array to demonstrate that it could perform simultaneous MR imaging, wireless localized B_0 shimming, and wireless respiratory tracking with a respiratory belt. First, 1st-order shimming from the scanner was applied to the entire FOV and an axial ΔB_0 map and EPI images were acquired through the inferior frontal brain region with no DC currents applied to the coil elements. Next, the optimal DC currents were calculated by minimizing the B_0 RMSE between the baseline ΔB_0 map and a linear combination of the four basis ΔB_0 maps acquired in the phantom. Finally, a ΔB_0 map and EPI images were acquired after applying the optimal DC currents to the eight iPRES coil elements (i.e., four pairs of symmetrical coil elements) to shim the B_0 inhomogeneity in the inferior frontal brain region and to correct for the corresponding EPI distortions. To better visualize the distortions, contour lines derived from undistorted anatomical images were overlaid onto the baseline and shimmed EPI images. In addition, the respiratory signal acquired with a respiratory belt was wirelessly transmitted without or with simultaneous MR image acquisition and wireless localized B_0 shimming to demonstrate

that the dual-stream iPRES-W head coil array could successfully transmit two independent data streams with no loss of information, additional signal noise, or signal dropout.

4.3.3 Simulated B_0 Performance

Additional simulations were performed to assess the localized B_0 shimming performance as a function of the number and configuration of anterior iPRES coil elements used to shim the brain. While similar simulations were initially performed to determine the optimal iPRES coil elements to be connected to the wireless battery pack (section 5.2), these additional simulations were performed to investigate whether the shimming performance could be further improved by: 1) adding additional adjustable DC currents to a larger number of anterior iPRES coil elements than those used in the experiment; and 2) increasing the maximum DC current range of the wireless battery pack. First, baseline ΔB_0 maps were acquired in the brain of three healthy volunteers (two males, one female). The optimal DC currents and residual B_0 RMSE after shimming for each of these three subjects were then calculated for the following coil configurations:

- 4 pairs of symmetrical iPRES coil elements (i.e., 4 adjustable DC currents applied to 8 out of the 16 anterior iPRES coil elements), as used in the experiment

- 7 pairs of symmetrical iPRES coil elements plus the two non-symmetrical coil elements, coils 1 and 4 (i.e., 9 adjustable DC currents applied to all 16 of the anterior iPRES coil elements)
- All 16 anterior iPRES coil elements with individually adjustable DC currents applied to each coil element.

Simulations were performed for these three configurations with the maximum DC shim current limited to either ± 2 A or ± 3 A.

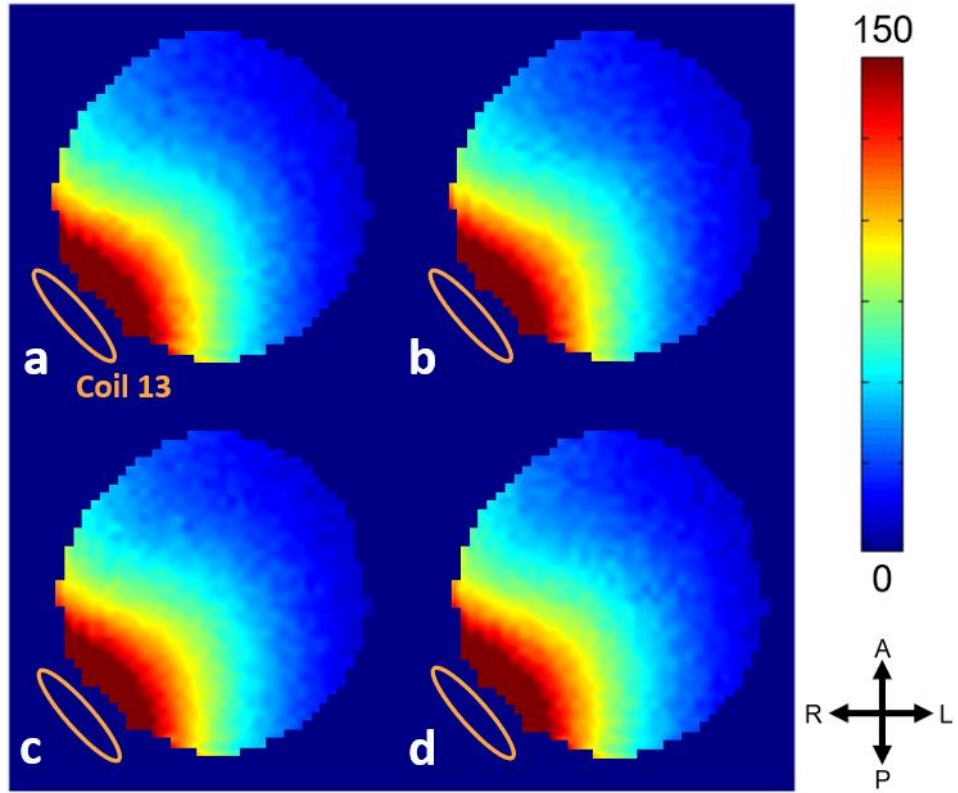


Figure 4.8: The acquired SNR maps in a water phantom for a representative iPRES-W coil element (coil 13) show no SNR degradation from the baseline coil configuration (a) to the iPRES coil configuration (b) and the iPRES-W coil configurations without (c) or while performing wireless localized B_0 shimming and wireless transmission of the respiratory signal (d).

4.4 Results

4.4.1 SNR Measurements

The acquired SNR maps in the phantom for a representative iPRES-W coil element (coil 13) show minimal difference ($< 1\%$) from the baseline coil configuration (Fig. 4.8a) to the iPRES coil configuration (Fig. 4.8b) or the iPRES-W coil configuration without (Fig. 4.8c) or while simultaneously performing wireless localized B_0 shimming and wireless data transfer of the respiratory signal (Fig. 4.8d), with SNR values averaged over the entire phantom of 38.6, 38.4, 38.3, and 38.4, respectively.

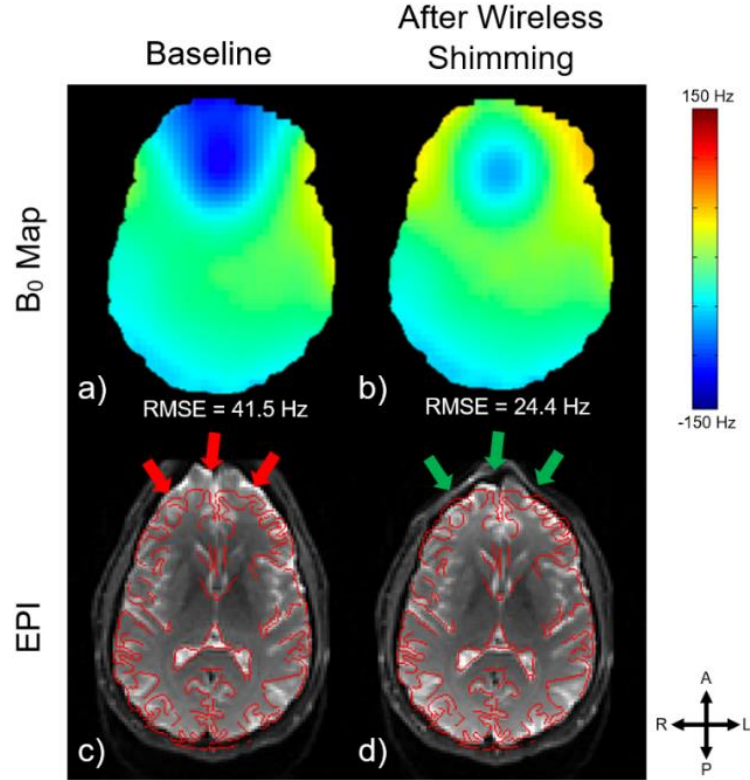


Figure 4.9: ΔB_0 maps and EPI images in a representative axial slice of the brain before (a, c) and after (b, d) performing wireless localized B_0 shimming with the dual-stream iPRES-W head coil array, which showed a significant reduction in B_0 inhomogeneities and geometric distortions relative to an undistorted anatomical image (red contour lines).

4.4.2 MR Imaging with Wireless Shimming and Respiratory Tracking

After performing standard 1st-order shimming with the scanner, a strong localized B_0 inhomogeneity remained in the inferior frontal brain region from magnetic susceptibility differences near the air/tissue interface in the frontal sinus cavity, which caused geometric distortions as highlighted by the red arrows relative to the contour lines from the anatomical images (Fig. 4.9c). After performing wireless localized B_0 shimming with the dual-stream iPRES-W head coil array, the B_0 RMSE in the slice was drastically reduced from 41.5 Hz (Fig. 4.9a) to 24.4 Hz (-41.2%) after shimming (Fig. 4.9b), which corresponded to a reduction in the geometric distortions in the spin-echo EPI images, as highlighted by the green arrows (Fig. 4.9d). Additionally, the respiratory signal wirelessly transmitted by one of the iPRES-W coil elements (coil 13) showed no change in the periodicity or signal integrity of the respiratory waveform with or without simultaneous MR image acquisition and wireless localized B_0 shimming (Fig. 4.10).

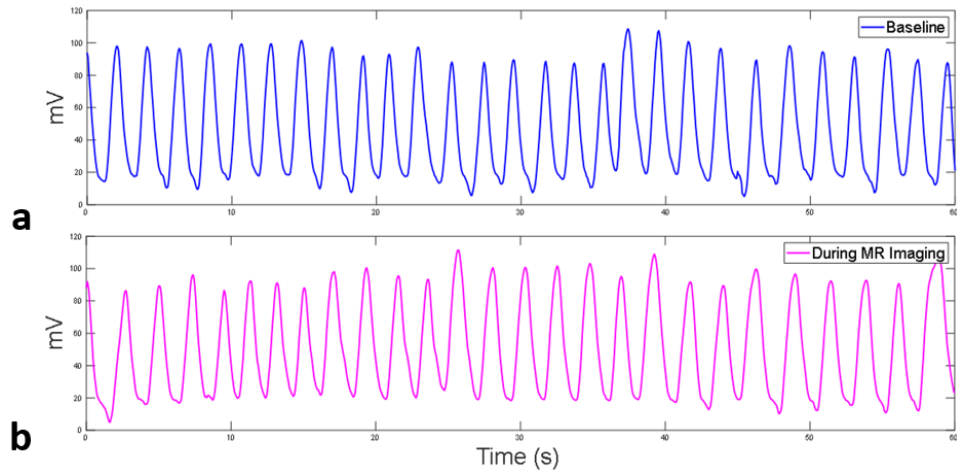


Figure 4.10: Wirelessly transmitted respiratory signal without (a) or with (b) simultaneous MR image acquisition and wireless localized B_0 shimming

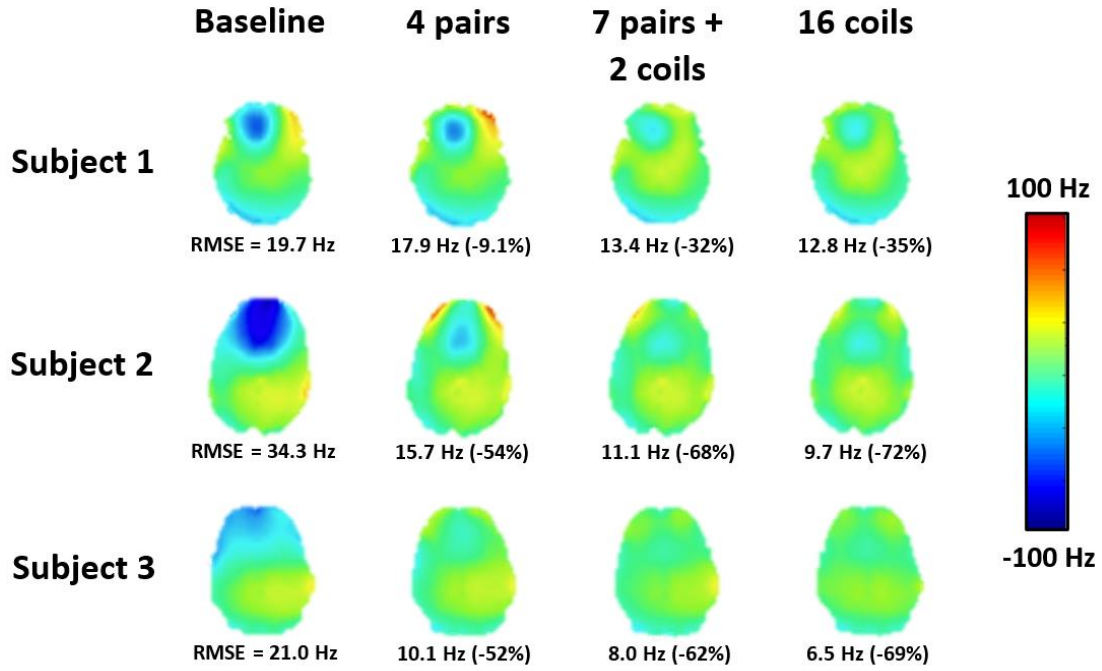


Figure 4.11: Simulated B_0 shimming results for the dual-stream iPRES-W head coil array show improved B_0 RMSE reduction when using additional anterior iPRES coil elements and/or individually adjustable DC currents.

4.4.3 Simulated B_0 Performance

The simulated B_0 shimming performance of the dual-stream iPRES-W head coil array show a greater B_0 RMSE reduction when additional anterior iPRES coil elements are utilized to shim the B_0 inhomogeneities in the inferior frontal brain region (Fig. 4.11, second column to third column). Similarly, the B_0 RMSE is further reduced when going from symmetrical DC currents applied to coil pairs to non-symmetrical DC currents (Fig. 4.11, third column to fourth column), particularly for subjects who have right/left asymmetries in their baseline ΔB_0 map because their head was slightly tilted relative to the iPRES-W coil array. There was generally improvement in RMSE when increasing the

maximum DC shim current range from ± 2 A to ± 3 A (results not shown), as the maximum optimal current for each subject and coil configuration was less than 2 A (subject 1 = 1.8 A, subject 2 = 1.9 A, subject 3 = 0.95 A).

4.5 Discussion

In this work, we proposed a novel dual-stream iPRES-W head coil array for simultaneous MR imaging and wireless data transfer for multiple applications, specifically to transmit commands for wireless localized B_0 shimming in the brain and wireless respiratory tracking with a respiratory belt. The SNR measurements showed that neither the modifications to implement the iPRES and iPRES-W coil designs nor performing simultaneous localized B_0 shimming and wireless data transfer of the respiratory signal had any impact on the image quality. The in vivo B_0 shimming experiments showed that using 8 iPRES coil elements, with pairs of symmetrical coil elements connected in series to one of the four outputs of the wireless battery pack, could perform wireless localized B_0 shimming and substantially reduce the B_0 inhomogeneities and distortions in the EPI images of the inferior frontal brain region, without requiring any scanner modifications or additional antenna systems within the scanner bore. Finally, the acquired respiratory signal with or without simultaneous imaging and localized B_0 shimming showed: 1) that the two wireless data streams were independent, as the wireless data transmitted to control the DC shim currents did not degrade the periodicity or signal integrity of the respiratory waveform, and 2) that MR

image acquisition and localized B_0 shimming did not degrade or impact the wirelessly transmitted signal.

Two previous in vivo studies at 3T using a 32-channel iPRES head coil array reported an average reduction in B_0 RMSE inhomogeneity in the frontal brain region from 67.8 to 15.2 Hz (-77.6%) (Truong (2014)) or from 118.9 to 18.6 Hz (-62%) (Willey (2021)), respectively. In the work presented here, the 48-channel iPRES-W head coil array with 8 anterior coil elements receiving four adjustable DC currents to pairs of symmetrical coil elements was able to reduce the B_0 RMSE from 41.5 Hz to 24.4 Hz (-41.2%). In future work, however, the shimming performance of the dual-stream iPRES-W head coil array could be further improved by 1) increasing the number of anterior iPRES coil elements used for shimming or expanding the battery pack design to allow for more individually adjustable DC shim currents, as shown by the simulated B_0 shimming performance (Fig. 4.11), and 2) modifying the 32 posterior coil elements into iPRES coil elements for additional degrees of freedom.

5. Aim 3: The iRFW Coil Design and Wireless Q-Spoiling

5.1 Introduction

The third aim of this dissertation is to provide wireless transmission of the scanner control signals for the RF coil array. To fully remove the coaxial cable between the RF receive coil array and scanner, control signals (e.g., the Q-spoiling scanner trigger to RF-isolate the preamplifier during the scanner transmit cycle and prevent damage to the LNA) must be transferred from the scanner to the coil array according to the pulse sequence timing. The work presented here further develops the iRFW coil design to enable wireless transmission of the scanner trigger signal, which in contrast to previously proposed designs (Lu (2017) and Lu (2018)), requires no scanner modifications or additional antenna systems within the scanner bore. Specifically, the iRFW coil design connected to an onboard wireless module is used to detune the receive coil element by activating a PIN diode during the scanner transmit cycle, which redirects RF currents on the coil structure to ground (Fig. 5.1). Wireless Q-spoiling is performed by sending a wireless command initiated by the scanner trigger from a computer in the console room to the on-board wireless module attached to the iRFW coil element, which then applies a DC voltage to the PIN diode. While the iRFW coil design has been previously used for simultaneous imaging and wireless control of multiple peripheral systems (e.g., wireless localized B_0 shimming (Cuthbertson (2019) and Cuthbertson (2020)), wireless respiratory tracking (Cuthbertson (2020)), and wireless physiological motion monitoring with an ultrasound probe (Willey (2020))), the wireless transmission

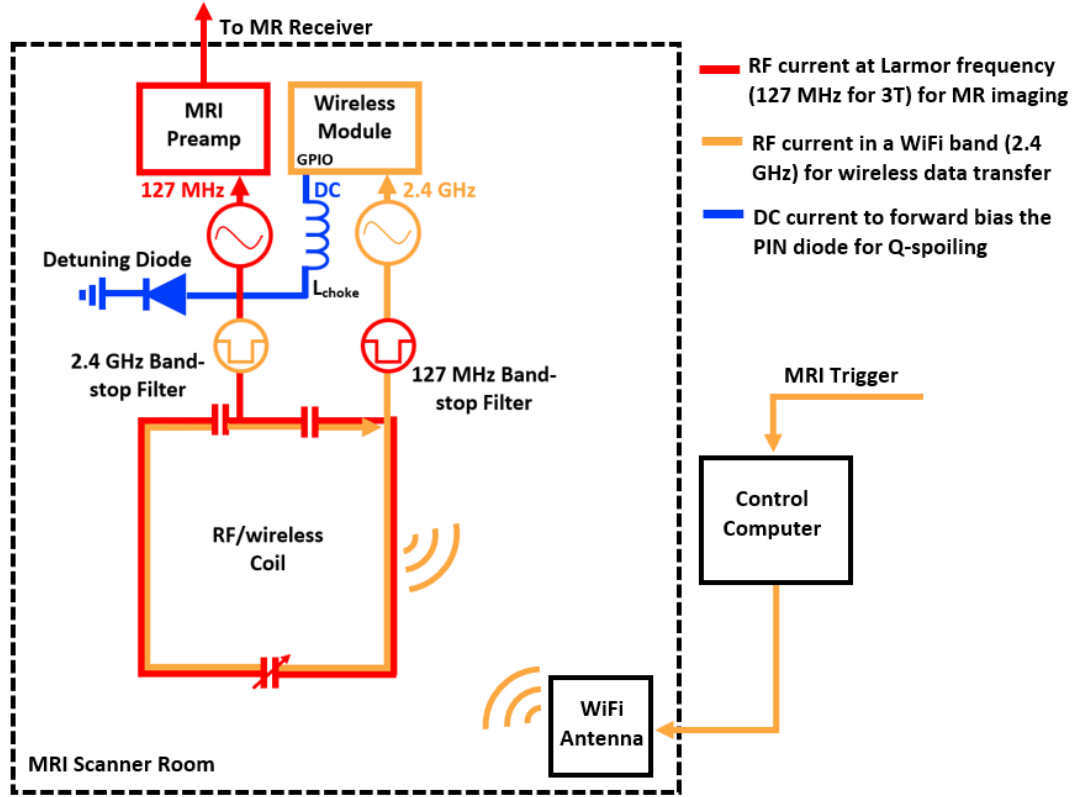


Figure 5.1: RF currents flow on the integrated RF/wireless coil design for simultaneous MR image acquisition (red) and wireless data transfer (orange), which a DC voltage (blue) is applied to the PIN diode from a GPIO pin from the wireless module for Q-spoiling.

of the scanner control signal uniquely requires a very reliable (i.e., no signal dropout) and low-latency wireless data link for real-time control of the on-coil electronics. Preliminary results have been presented in abstract form (Cuthbertson (2021)).

5.2 iRFW Coil Design Implementation

First, a 10-cm diameter RF coil element constructed to be resonant at the Larmor frequency was modified into an iRFW coil element by adding custom 127-MHz (Fig. 5.1, red) and 2.4 GHz (Fig. 5.1, orange) band-stop filters between the coil element and the

wireless module (ESP8266, Adafruit, New York, NY) and MR preamplifier, respectively, to prevent RF losses incurred in both of them in their frequency band (sections 3.2 and 4.2). Next, the coil element was further modified for wireless Q-spoiling by placing a positive-intrinsic-negative (PIN) diode between the 2.4-GHz band-stop filter and the MR preamplifier (Fig. 5.1, blue). This PIN diode is wirelessly activated by applying a DC voltage from the RF-isolated wireless module during the scanner transmit cycle, which detunes the coil element to protect the preamplifier from damage.

5.3 Experimental Setup and Tests

5.3.1 Wireless Q-Spoiling and SNR Measurements

In a first proof-of-concept experiment, to verify that wireless Q-spoiling with the iRFW coil element did not degrade its image quality, a time series of 76 gradient-echo EPI images (as used in fMRI experiments) were acquired with the iRFW coil on a water phantom using either wired or wireless Q-spoiling, which was achieved by applying an activation voltage to the PIN diode with either the conventional wired connection from the scanner or the wireless module GPIO pin, respectively. The SNR of the mean image and the temporal SNR (TSNR) of the image time series were then calculated for both Q-spoiling methods to evaluate their image quality. During this experiment, the PIN diode activation and scanner trigger voltage signals were measured simultaneously with an oscilloscope (RTE-1024, Rhode & Schwarz, Munich, Germany) to verify that the wireless module could provide an accurate and similar voltage signal as the scanner for Q-

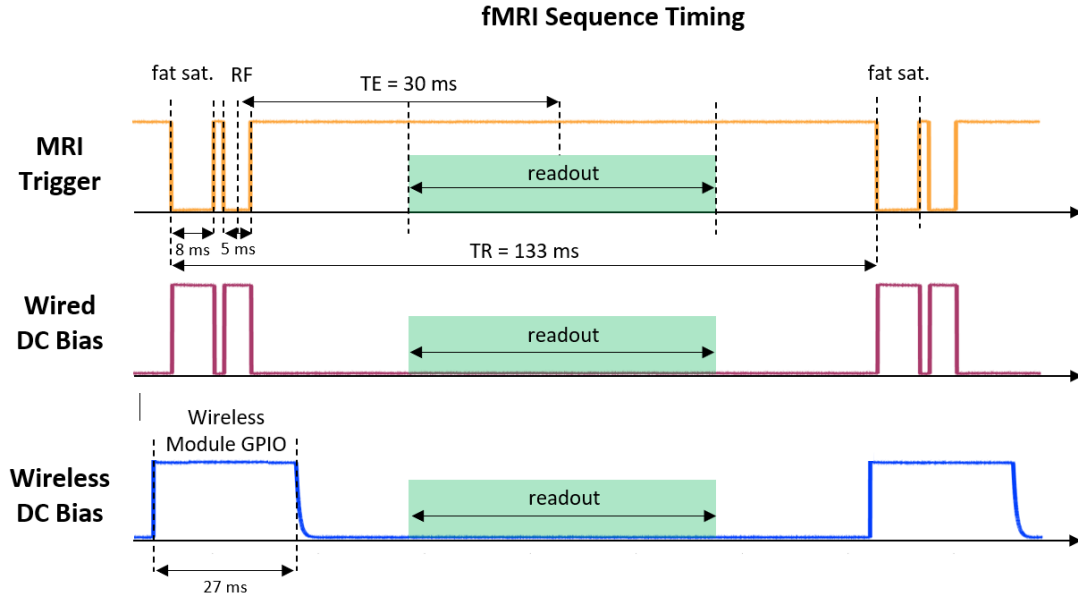


Figure 5.2: Diagram of the fMRI pulse sequence showing the timing of the MRI scanner trigger (orange), which was used for detuning the iRFW coil, either by conventional wired connections (purple) or by wirelessly transmitting a digital signal corresponding to the scanner trigger for wireless Q-spoiling (blue).

spoiling. The MR data was acquired on a 3T Premier Ultra-High Performance MRI scanner (GE Healthcare, Milwaukee, WI) and was transferred from the coil element to the scanner using the conventional wired connection. The data analysis was performed in MATLAB (The MathWorks, Natick, MA).

5.3.2 Wireless Performance During Q-Spoiling

In a second proof-of-concept experiment, to verify that the wireless performance did not degrade during activation of the PIN diode for wireless Q-spoiling, the Wi-Fi radiated power pattern was measured in a fully anechoic chamber (section 3.2.3) with and without an activation voltage applied to the PIN diode.

5.4 Results

5.4.1 Wireless Q-Spoiling and SNR Measurements

The iRFW coil element was able to reliably apply an activation voltage to the PIN diode for wireless Q-spoiling (Fig. 5.2, blue) that was similar to the voltage applied by

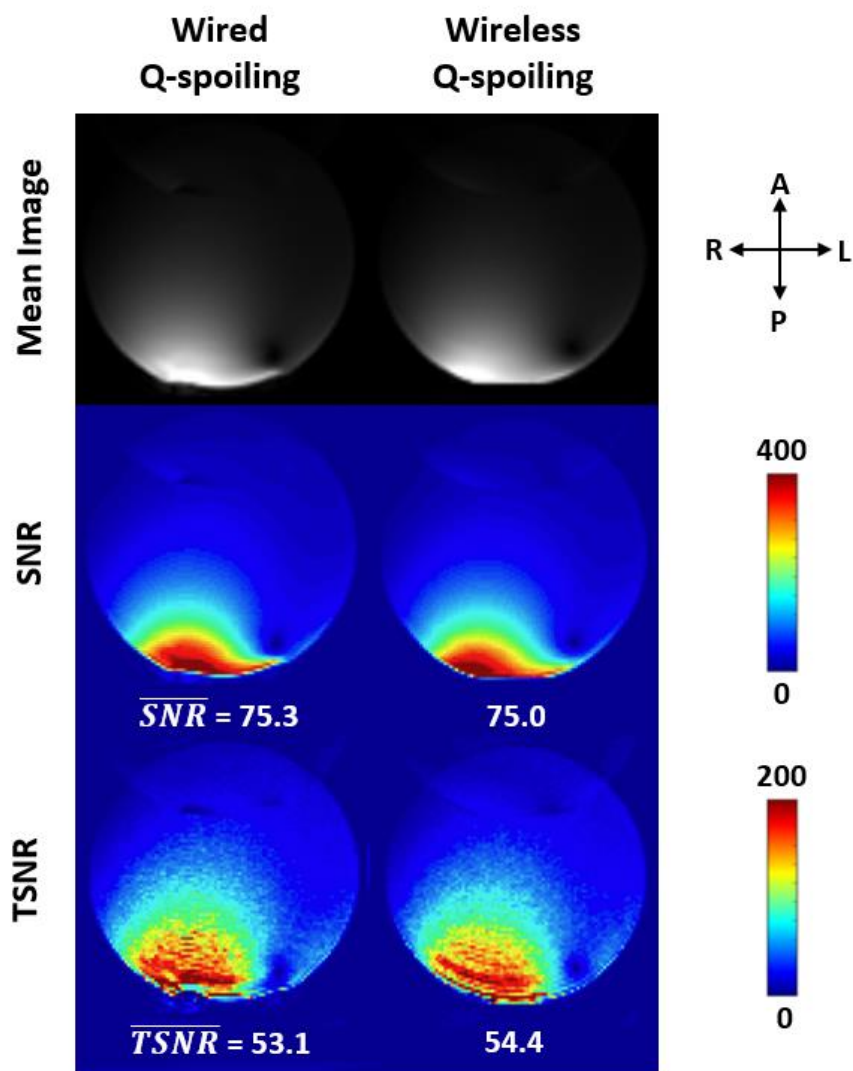


Figure 5.3: Gradient-echo EPI mean images, SNR maps of the mean image, and TSNR maps of the image time series acquired in a water phantom, showing no degradation in image quality for wireless Q-spoiling using the iRFW coil compared to conventional wired Q-spoiling.

the scanner during conventional wired Q-spoiling (Fig. 5.2, purple). Additionally, the SNR and TSNR of the coil averaged over the phantom were similar for wired Q-spoiling (75.3 and 53.1) and wireless Q-spoiling (75.0 and 54.4) (Fig. 5.3).

5.4.2 Wireless Performance During Q-Spoiling

Wireless Q-spoiling with the iRFW coil showed no impact on the Wi-Fi center frequency 3D (Fig. 5.4a) or principal plane (Fig. 5.4b) radiated power gain patterns

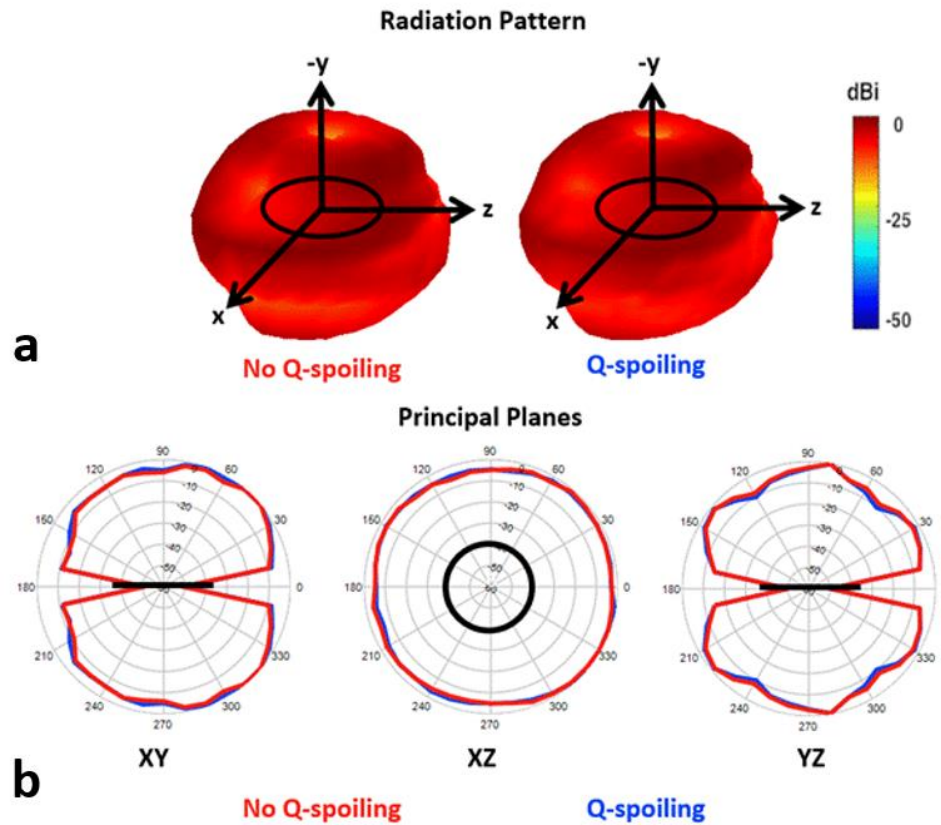


Figure 5.4: The iRFW coil's 3D radiated power (a) and the radiated power in the principal planes (b) show minimal change when the PIN diode is not activated (during the receive cycle; red line) versus activated for Q-spoiling (during the transmit cycle; blue line).

(section 3.4.4), which determine its wireless performance. Further, the radiated power of the coil across the entire Wi-Fi frequency band changed by <1% when a voltage was applied to the PIN diode for Q-spoiling relative to the same unbiased PIN diode measurement.

5.5 Discussion

This work demonstrates that the integrated RF/wireless coil design can reliably perform wireless Q-spoiling for MR image acquisition without degrading image quality relative to the conventional Q-spoiling method. Additionally, the wireless performance of the coil is maintained throughout the MRI scan, which is critical to protect the MR preamplifier during the scanner transmit cycle. These results can be expanded upon for additional on-coil triggering or data synchronization, for example, to improve the syncing of fMRI stimuli and subject responses with the timing of the MR image acquisition.

6. Aim 4: The 4-Channel Power Harvesting Coil Array

6.1 Introduction

The fourth aim of this dissertation is to provide wireless on-coil power for wireless devices. As the number of wireless devices within the scanner bore increases, the electrical power required on-coil is a major limitation for future applications and wireless development. For example, a conventional wired RF coil array only needs power delivered to the LNA and Q-spoiling electronics; however, to enable wireless RF coil arrays, the power requirements drastically increase as power must be delivered to the on-board ADCs, potential signal mixers, and wireless transceivers. Additionally, in-bore wireless power requirements also scale with the number of individual RF coil elements and peripheral devices. While previous work has investigated WPT (Byron (2017) and Byron (2019a)) or WPH (Höfflin (2013), Bryon (2019a), and Venkateswaran (2020)) systems for delivering the wireless power, these preliminary designs require major scanner modifications or are limited to specific scan types and parameters, respectively. In this work, these limitations are addressed by using an array of harvesting coils to wirelessly recharge an in-bore battery during image acquisition via unsmoothed regulated DC pulses. The proposed design maximizes efficiency by ensuring all harvested energy is applied to the battery, while also providing a buffer between the acquired voltage pulses and the wireless device. Additionally, the ability to charge the batteries during image acquisition would 1) reduce the number of batteries required for high-power applications and 2) extend the battery runtime and require

fewer interruptions in the clinical workflow to swap out battery packs. While previous work has investigated the ability to pulse-charge Li-ion batteries and the impact it has on charge rate (Majid (2017)), battery cycle lifetime (Amanor-Boadu (2018)), and durability (Li (2019)), the experiments here demonstrate that it is a novel and promising charging technique within the MR scanner bore and allows for high-efficiency battery charging regardless of the pulse sequence or scan parameters. Preliminary results have been presented in abstract form (Cuthbertson (2022a)).

6.2: Harvesting Coil Array: Construction and Implementation

First, four 10-cm diameter harvesting RF coil elements were constructed from copper clad (1.6 mm) FR-1 PCB to be resonant at the Larmor frequency and arranged into a 1x4 array (Fig. 6.1a), where the coil overlap was optimized using a VNA to minimize the mutual coupling between coil elements. The coil outputs were connected either in series (Fig. 6.1b), parallel (Fig. 6.1c), or a series/parallel combination (Fig. 6.1d) to achieve higher induced RF voltages due to the series voltages adding together during low B_1 field scans (e.g., flip angles $< 20^\circ$), a more balanced power delivery to multiple in-bore batteries during high B_1 field scans (e.g., flip angles $> 50^\circ$), or a combination of both, respectively. Second, a full-wave AC-DC Greinacher voltage converter (Venkateswaran (2020)) was added to each output to rectify the induced RF voltages from the coils, which consisted of two Schottky diodes (SMS3924-079LF, Skyworks Solutions Inc., Irvine, CA) and two 0.1 μF capacitors (Fig. 6.1, purple). For this preliminary

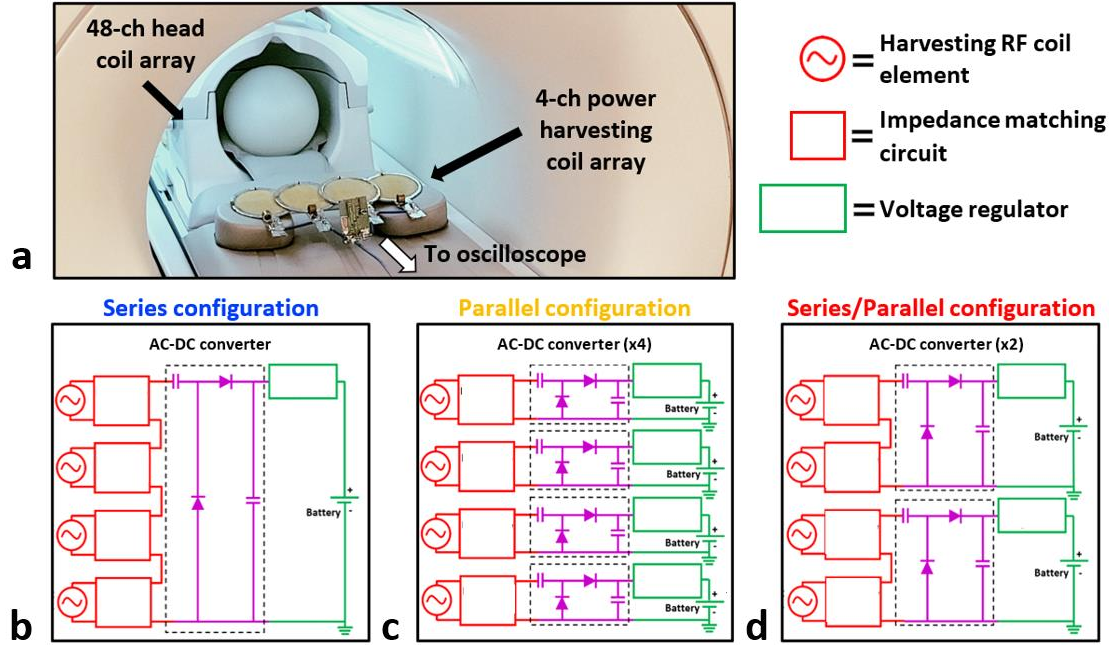


Figure 6.1: The 4-channel harvesting coil array and electronics were placed in the scanner bore in a coronal plane to maximize efficiency (a), with the coil outputs connected in series (b), parallel (c), or a combination of series and parallel (d). The harvested RF energy (red) was first rectified using an AC-DC converter (purple) before being regulated and applied to the battery (green).

implementation, the wireless harvested power through each AC-DC converter was limited to 420 mW to prevent damage to the rectifier diodes, which only had a maximum power rating of 500 mW. Finally, the acquired signal was passed through a linear voltage regulator (LM317T, STMicroelectronics, Geneva, Switzerland) placed in series with a rechargeable 1800-mAh LiPo MR-compatible battery (GM-NM103450-PCB, PowerStream Technology, Orem, UT) (Fig. 6.1, green) to prevent the unsmoothed DC voltage pulses from exceeding 3.9 V, which could otherwise damage the battery ($V_{\text{battery}}^{\text{max}} = 4.2\text{V}$).

6.3 Experimental Setup and Tests

6.3.1 Wireless Power Harvesting for Changing B_1 Transmit Power

In a first experiment, multi-echo GRE images were acquired on a water phantom with an unmodified production 48-channel head coil array using flip angles between 5° and 90° for each of the three coil output configurations to demonstrate that the 4-channel harvesting coil array could pulse-charge a battery regardless of the B_1 transmit power from the scanner. The harvesting coil array was placed 30 cm inferior to the water phantom (Fig. 6.1a) to prevent banding artifacts in the MR image, which occur due to the induced RF currents in the harvesting coil at the Larmor frequency (Byron (2019b) and (Venkateswaran (2020))). All proof-of-concept experiments were performed on a 3T Premier Ultra-High Performance MRI scanner (GE Healthcare, Milwaukee, WI) and the unsmoothed DC pulses applied to the battery were measured using an oscilloscope (RTE-1024, Rhode & Schwarz, Munich, Germany).

6.3.2 Wireless Power Harvesting for Various MR Pulse Sequences

In a second experiment, images were acquired over a 10-minute duration using various pulse sequences: GRE, GRE echo-planar imaging (GRE-EPI) typically used in fMRI, DTI, and T_1 -weighted MPRAGE, with the harvesting coils in the series configuration, to demonstrate the ability to harvest power regardless of the pulse sequence and apply the harvested energy to recharge the battery. During these

experiments, the input RF voltages, AC-DC converted pulses, and DC power delivered to the battery were measured using the oscilloscope.

6.4 Results

6.4.1 Wireless Power Harvesting for Changing Scan Parameters

The 4-channel harvesting coil array was able to provide unsmoothed regulated DC pulses (0.57 to 0.95 ms pulse width range) to charge the MR-compatible battery for various flip angles and corresponding B_1 transmit powers during GRE image acquisition (Fig. 6.2a) for each of the three coil output configurations (Fig. 6.2b). To achieve small ($>20^\circ$) or large ($>60^\circ$) flip angles, the MR scanner automatically adjusted the RF pulse shape and width to achieve the desired B_1 field amplitude, as seen in Figure 6.2a, which ensured the correct received MR signal amplitude when applied to the LNA for image acquisition. This change in pulse width results in a region where the wireless power harvested (i.e., Watt or Joule/second) does not change for increased flip angles (Fig. 6.2b, green), however, it is important to note that total acquired energy (in Joules) continues to linearly increase. The maximum wireless power harvested for the series, series/parallel, and parallel configurations were 420, 500, and 340 mW, respectively. Since the series configuration utilizes only a single AC-DC converter, the maximum power through the circuit was limited to 420 mW to prevent damage to the diodes, which resulted in a loss of efficiency between the ideal (Fig. 6.2b, dashed blue line) and actual (Fig. 6.2b, solid blue line) total power harvested. Alternatively, the

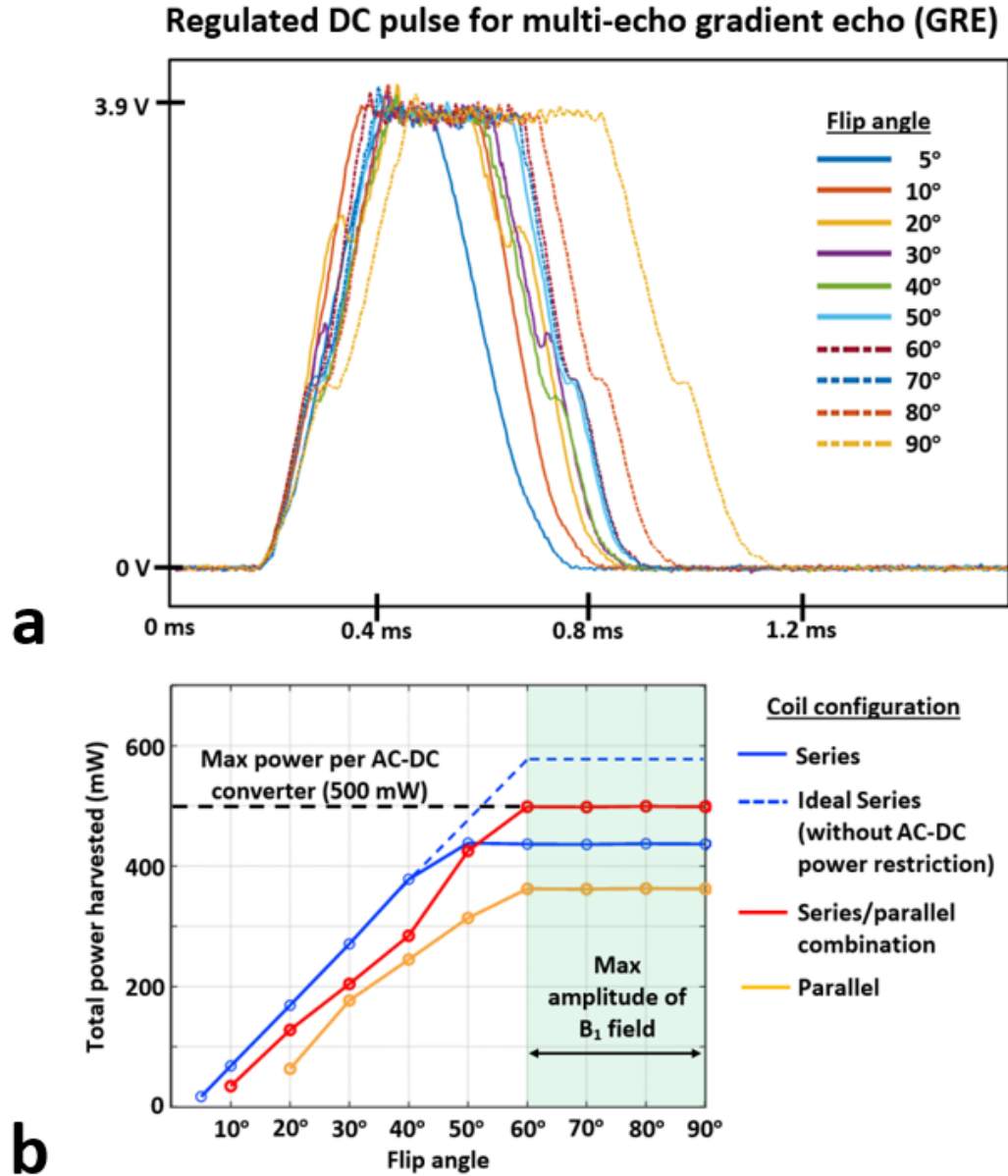


Figure 6.2: Unsmoothed DC pulses were applied to the battery for various flip angles during GRE image acquisition (a) with the power delivered to the battery calculated for each coil configuration (b).

harvested power through the series/parallel and parallel configurations were divided between two or four AC-DC converters, respectively, where the max power though each converter was either 250 mW or 85 mW.

6.4.2 Wireless Power Harvesting for Various MR Pulse Sequences

The 4-channel harvesting coil array was able to provide energy to recharge the battery for various MR pulse sequences with differing parameters, specifically, GRE, GRE-EPI, DTI, and MPRAGE pulse sequences (Fig. 6.3), with a total applied energy after 10 minutes of 0.7, 6.6, 9.0, and 2.5 mJ, respectively (Fig. 6.4).

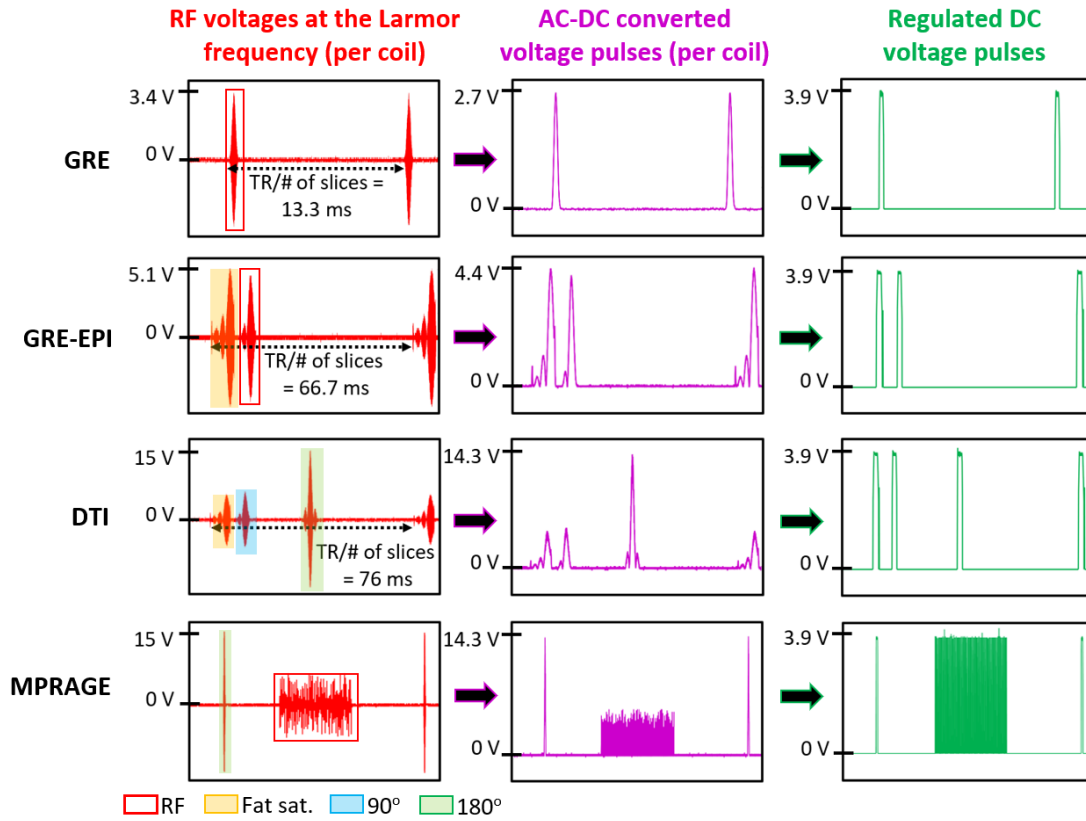


Figure 6.3: RF energy (red) was harvested during GRE, GRE-EPI, DTI, and MPRAGE image acquisitions and rectified (purple) using an AC-DC converter before being regulated (green) and applied to the battery.

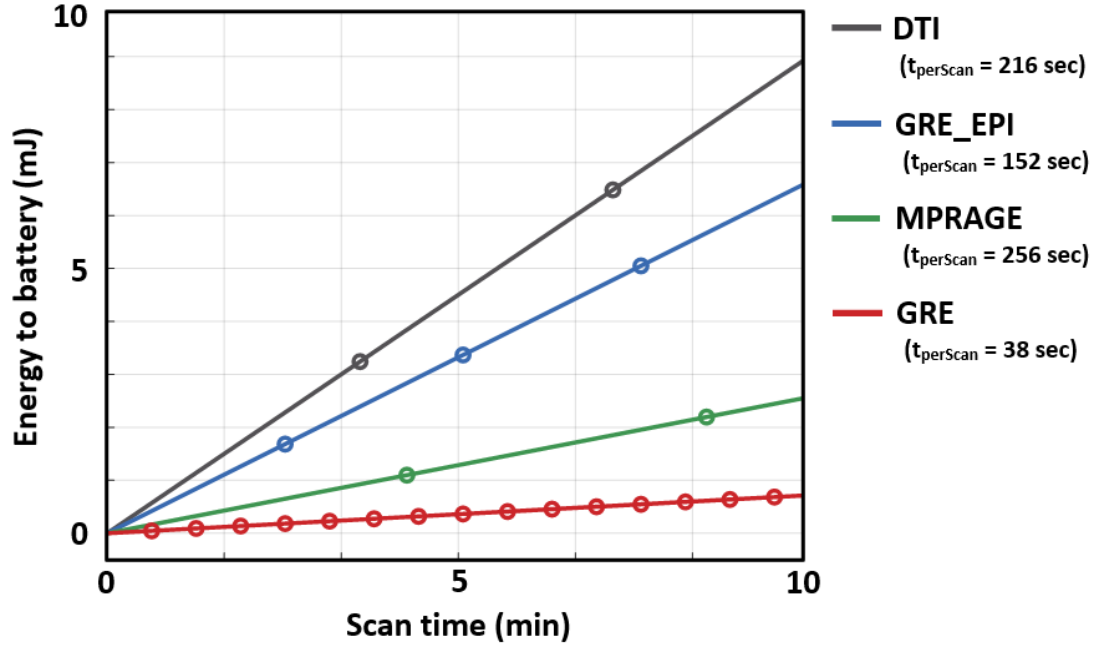


Figure 6.4: Energy applied to the battery over a duration of 10 minutes during GRE, GRE-EPI, DTI and MPRAGE image acquisitions.

6.5 Discussion

This work demonstrates that the 4-channel harvesting coil array can reliably harvest power during image acquisition regardless of the pulse sequence or scan parameters. When the B_1 transmit power is low (for flip angles $< 20^\circ$), a series configuration is required, otherwise the induced voltage is too low to be applied to the battery for charging. When the B_1 transmit power is high (for flip angles $> 50^\circ$), a series/parallel configuration with multiple batteries can be used to avoid power loss to currently available components required for harvesting. For very large flip angles ($> 60^\circ$, green region in Fig. 6.2b), the B_1 transmit power is limited by the scanner to prevent damaging the RF receive coil array electronics and instead the RF pulse duration is

increased. Since the DC pulses applied to the battery are unsmoothed, there is no impact in power harvested when changing the TR or number of slices, in contrast to a previously proposed power harvesting method (Byron (2019) and Venkateswaran (2020)). Expanding upon these preliminary results, we envision adding a wireless module and voltage-controlled switches that could wirelessly change the coil configuration depending on the flip angle or RF pulse type (e.g., fat saturation) to optimize efficiency via control signals from the MRI scanner trigger (Cuthbertson (2021)).

7. Conclusion

This dissertation further developed the iPRES-W coil design, along with new supporting electronics, and demonstrated its ability to enable wireless data transmission for the B_0 shimming, peripheral device, scanner control signals, and on-coil power subsystems. This novel integrated wireless antenna design is the first in MRI with the ability to wirelessly transmit data for numerous applications such as the localized B_0 shimming with integrated RF/shim coil arrays, peripheral devices such as physiological monitoring with a respiratory belt, and scanner control signals for Q-spoiling.

First, the results from section 3 (**Aim 1**) show that the iPRES-W spine coil array can perform simultaneous imaging and wireless localized B_0 shimming of the cervical spinal cord in vivo, with no degradation in SNR, minimal change in wireless performance, and, in its current proof-of-concept implementation with only 4 coil elements, a slightly better shimming performance than 2nd-order SH shimming. This novel coil design and wireless battery pack represents the first implemented wireless shimming system in MRI and could be used for numerous other localized B_0 shimming applications (e.g., functional MRI or MR spectroscopy).

Second, the results from section 4 (**Aim 2**) show that the dual-stream iPRES-W head coil array can perform simultaneous MR imaging and wireless data transfer for multiple independent data streams and bidirectional wireless data transfer, specifically, for wireless localized B_0 shimming of the brain in vivo and wireless respiratory tracking with a respiratory belt, with no degradation in SNR or additional antenna systems

within the scanner bore. This novel iPRES-W implementation, with isolated wireless data streams, could be integrated into other RF coil array structures to wirelessly transmit other types of data (e.g., for motion detection with a camera and field monitoring with NMR probes).

Third, the preliminary results from section 5 (**Aim 3**) demonstrate that the iRFW coil design was able to reliably apply an activation voltage to the PIN diode for wireless Q-spoiling that was similar in amplitude and duration to the voltage applied by the scanner during conventional wired Q-spoiling, without requiring any additional antenna systems or scanner modifications. Since the wireless data link provided by the iRFW coil element showed no signal dropout and low-latency, this coil design could be used in future work to additionally wirelessly transmit the MR signal data for imaging.

Finally, the results from section 6 (**Aim 4**) show that the 4-channel harvesting coil array can reliably harvest power during MR image acquisition regardless of the pulse sequence or scan parameters. This novel implementation and coil array represents the first wireless power harvesting system for MRI that can reliably recharge a battery regardless of the scan parameters. Future work could expand upon these preliminary results to build an iPRES-W power harvesting coil array to recharge several on-board batteries, where wireless switches and voltage level sensors automatically detect low-voltage batteries and redirect the harvested power for recharging.

References

- Aggarwal, K., Joshi, K., Rajavi, Y., Taghivand, M., Pauly, J., Poon, A., Scott, G. (2017). A millimeter-wave digital link for wireless MRI. *IEEE Transactions on Medical Imaging*, 36(2), 574-83.
- Aghaeifar, A., Mirkes, C., Bause, J., Steffen, T., Avdievitch, N., Henning, A., Scheffler, K. (2018). Dynamic B_0 shimming of the human brain at 9.4 T with a 16-channel multi-coil shim setup. *Magnetic Resonance in Medicine*, 80(4), 1714-25.
- Amanor-Boadu, J., Guiseppi-Elie, A., Sanchez-Sinencio, E. (2018). The impact of pulse charging parameters on the life cycle of lithium-ion polymer batteries. *Energies*, 11(8), 2162.
- Armenean, C., Perrin, E., Armenean, M., Beuf, O., Pilleul, F., Saint-James H. (2004). RF-induced temperature elevation along metallic wires in clinical magnetic resonance imaging: influences of diameter and length. *Magnetic Resonance in Medicine*, 52:1200-6.
- Avadhani, A., Ilayaraja, V., Shetty A., Rajasekaran, S. (2010). Diffusion tensor imaging in horizontal gaze palsy with progressive scoliosis. *Magnetic Resonance in Medicine*, 28(2), 212-16.
- Beaujoin, J., Palomero-Gallagher, N., Boumezbeur, F., Axer, M., Bernard, J., Poupon, F., Schmitz, D., Mangin J., Poupon, C. (2018). Post-mortem inference of the human hippocampal connectivity and microstructure using ultra-high field diffusion MRI at 11.7 T. *Brain Structure & Function*, 223(5), 2157-79.
- Behin, R., Bishop, J., Henkelman, M. (2005). Dynamic range requirements for MRI. *Magnetic Resonance Part B: Magnetic Resonance Engineering*, 26B(1), 28-35.
- Biber, S., Wohlfarth, K., Kirsch, J., Schmidt, A. (2012). Design of a local shim coil to improve B_0 homogeneity in the cervical spine region. *Proceedings of the ISMRM 20th Annual Meeting*, May 2012, Melbourne, Australia: pg. no. 2746.
- Boadie, D.W., Mayberg, H.S. (2017). Neuroimaging Advances for Depression. *Cerebrum*, 2017, cer-16-17.
- Bulumulla, S., Fivelan, E., Park, K., Foo, T., Hardy, C. (2015). Inductively coupled wireless RF coil arrays. *Magnetic Resonance Imaging*, 33(3), 351-57.

- Byron, K., Robb, F., Stang, P., Vasanaawala, S., Pauly, J., Scott, G. (2017). An RF-gated wireless power transfer system for wireless MRI receive arrays. *Concepts in Magnetic Resonance Part B: Magnetic Resonance Engineering*, 47B(4), e21360
- Byron, K., Robb, F., Vasanaawala, S., Pauly, J., Scott, G. (2018). A wireless power transfer system for MRI scanners. *IEEE Wireless Power Transfer Conference*, June 2018, Montréal, QC: pg. no. 1-4.
- Byron, K., Winkler, S., Robb, F., Vasanaawala, S., Pauly, J., Scott, G. (2019a). An MRI compatible RF MEMs controlled wireless power transfer system. *IEEE Transactions on Microwave Theory and Techniques*, 67(5), 1717-26.
- Byron, K., Robb, F., Vasanaawala, S., Pauly, J., Scott, G. (2019b). Harvesting power wirelessly from MRI scanners. *Proceedings of the ISMRM 27th Annual Meeting*, May 2019, Montréal, QC: pg. no. 1535.
- Chen, B., Weber, N., Odille, F., Large-Dessale, C., Delmas, A., Bonnemains, L., Felblinger, J. (2017). Design and validation of a novel MR-compatible sensor for respiratory motion modeling and correction. *IEEE Transactions on Biomedical Engineering*, 64(1), 123-33.
- Cogswell, P., Trzasko, J., Gray, E., Campeau, N., Rossman, P., et al., (2021). Application of adaptive image receive coil technology for whole-brain imaging. *American Journal of Roentgenology*, 216(2), 552-9.
- Collick, B., Behzadnezhad, B., Hurley, S., Mathew, N., Behdad, N., Lindsay, S., Robb, F., Stormont, R., McMillan, A. (2020). Rapid development of application-specific flexible MRI receive coils. *Physics in Medicine & Biology*, 65(19), 19NT01.
- Corea, J., Flynn, A., Lechene, B., Scott, G., Reed, G., Shin, P., Lustig, M., Arias, A. (2016). Scree-printed flexible MRI receive coils. *Nature Communications*, 7:10839.
- Cuthbertson, J., Darnell, D., Bresticker, J., Stormont, R., Robb, F., Song, A., Truong, TK. (2018). The iPRES-W AIR coil: A flexible RF coil for simultaneous MR image acquisition, wireless communication, and localized B_0 shimming. *Proceedings of the ISMRM 26th Annual Meeting*, June 2018, Paris, France: pg. no. 0016.
- Cuthbertson, J., Darnell, D., Stormont, R., Robb, F., Song, A.W., Truong, TK. (2019). A 4-channel iPRES-W AIR coil array for simultaneous MR image acquisition and wirelessly-controlled localized B_0 shimming of the spinal cord. *Proceedings of the ISMRM 27th Annual Meeting*, May 2019, Montreal, Canada: pg. no. 1489.

Cuthbertson, J., Truong, TK., Yadav, V., Robb, F., Song, A.W., Darnell, D. (2020). Dual-stream iPRES-W head coil array for MR imaging, wireless respiratory tracking, and wireless localized B_0 shimming. *Proceedings of the ISMRM 28th Annual Meeting*, August 2020, Virtual: pg. no. 1262.

Cuthbertson, J., Truong, TK., Chen, J., Robb, F., Song, A., Darnell, D. (2021). An integrated radio-frequency/wireless (iRFW) coil design for wireless Q-spoiling during MR imaging. *Proceedings of the ISMRM 29th Annual Meeting*, May 2021, Virtual: pg. no. 1605.

Cuthbertson, J., Truong, TK., Robb, F., Song, A., Darnell, D. (2022a). Wireless power harvesting of the B_1 field during MR image acquisition for pulse charging of MR-compatible batteries. *Proceedings of the ISMRM 30th Annual Meeting*, May 2021, London, England.

Cuthbertson, J., Truong, TK., Stormont, R., Robb, F., Song, A., Darnell, D. (2022b). An iPRES-W coil array for simultaneous imaging and wireless localized B_0 shimming of the cervical spinal cord. *Magnetic Resonance in Medicine*. DOI: 10.1002/mrm.29257

Darnell, D., Truong, TK., Song, A.W., (2017). Integrated parallel reception, excitation, and shimming (iPRES) with multiple shim loops per radio-frequency coil element for improved B_0 shimming. *Magnetic Resonance in Medicine*, 77(5), 2077-86.

Darnell, D., Ma, Y., Wang, H., Rodd, F., Song, A.W., Truong, TK. (2018). Adaptive integrated parallel reception, excitation, and shimming (iPRES-A) with microelectromechanical systems switches. *Magnetic Resonance in Medicine*, 80(1), 371-79.

Darnell, D., Cuthbertson, J., Robb, F., Song, A.W., Truong, TK. (2019). Integrated radio-frequency/wireless coil design for simultaneous MR image acquisition and wireless communication. *Magnetic Resonance in Medicine*, 81(3), 2176-83.

Dietrich, B., Brunner, D., Wilm, B., Barmet, C., Preussmann, K. (2016). Continuous magnetic field monitoring using rapid re-excitation of NMR probe sets. *IEEE Transactions on Medical Imaging*, 35(6), 1452-62.

Dietrich, S., Aigner, C., Mayer, J., Kolbitsch, C., Schulz-Menger, J., Schaeffter, T., Schmitter, S. (2022). Motion-compensated fat-water imaging for 3D cardiac MRI at ultra-high fields. *Magnetic Resonance in Medicine*, 00:1-16. doi:10.1002/mrm.29144.

Delfino, J., Krainak, D., Flesher, S., Miller D. (2019). MRI-related FDA adverse event reports: A 10-yr review. *American Association of Physicists in Medicine*, 46(12), 5562-71.

de Graaf, R.A., Brown, P., McIntyre, S., Rothman, D., Nixon, T. (2003). Dynamic shim updating (DSU) for multislice signal acquisition. *Magnetic Resonance in Medicine*, 49(3), 409-16.

Dichter, G.S. (2012). Functional magnetic resonance imaging of autism spectrum disorders. *Dialogues in Clinical Neuroscience*, 14(3), 319-51.

Fayad, H., Record, P. (2005). Wideband saline-water antenna. *IEEE Wideband and Multi-band Antennas and Arrays*, pp. 197-201.

Frass-Kriegl, R., Isabel, L., Pichler, M., Sieg, J., Moser, E., Windischberger, C., Laistler, E. (2018). Flexible 23-channel coil array for high-resolution magnetic resonance imaging at 3 Tesla. *PLoS ONE*, 13(11), e0206963.

Fuentes, R., Petersson, P., Siesser, W., Caron, M., Nicolelis, M. Spinal cord stimulation restores locomotion in animal models of Parkinson's disease. *Science*, 323(5921), 1578-82.

Golay, M.J. (1958). Field homogenizing coils for nuclear spin resonance instrumentation. *Review of scientific instruments*, 29(4), 313-15.

Han, H., Song, A.W., Truong, TK. (2013). Integrated parallel reception, excitation, and shimming (iPRES). *Magnetic Resonance in Medicine*, 70(1), 241-47.

Höfflin, J., Fischer, E., Hennig, J., Korvink, J. (2013). Energy harvesting with a figure-8 coil – towards energy autonomous MRI detection. *Proceedings of the Experimental Nuclear Magnetic Resonance Conference*, April 2013, Asilomar, USA, pg. no. 728.

Juchem, C., Nixon, T., McIntyre, S., Rothman, D., de Graaf R.A., (2010). Magnetic field modeling with a set of individual localized coils. *Journal of Magnetic Resonance*, 204(2), 281-89.

Juchem, C., Brown, P., Nixon T., McIntyre, S., Rothman, D., de Graaf, A. (2011a). Multicoil shimming of the mouse brain. *Magnetic Resonance in Medicine*, 66(3), 893-900.

Juchem, C., Nixon, T., McIntyre, S., Boer, V., Rothman, D., de Graaf, R. (2011b). Dynamic multi-coil shimming of the human brain at 7T. *Journal of Magnetic Resonance*, 212(2), 280-88,

- Juchem, C., Rudrapatna, S., Nixon, T., de Graff R.A., (2015). Dynamic multi-coil technique (DYNAMITE) shimming for echo-planar imaging of the human brain at 7 Tesla. *NeuroImage*, 105(), 462-72.
- Kim, D., Adalsteinsson, E., Glover, G., Spielman, D. (2002). Regularized higher-order in vivo shimming. *Magnetic Resonance in Medicine*, 48(4), 715-22.
- Kirilina, E., Lutti, A., Poser, B., Blankenburg, F., Weiskopf, N. (2016). The quest for the best: The impact of different EPI sequences on the sensitivity of random effect fMRI group analyses. *NeuroImage*, 126(1), 49-59.
- Ko, Y., Bi, W., Felder, J., Shah, NJ., (2019). Wireless digital data transfer based on WiGig/IEEE 802.11ad with self-shielded antenna gain enhancement for MRI. *Proceedings of the ISMRM 27th Annual Meeting*, May 2019, Montréal, QC: pg. no. 1537.
- Li, S., Wu, Q., Zhang, D., Liu, Z., He, Y., Wang, Z., Sun, C. (2019). Effects of pulse charging on the performance of lithium-ion batteries. *Nano Energy*, 56(), 555-62.
- Lu, J., Robb, F., Pauly, J., Scott, G. (2017). Wireless Q-spoiling of receive coils at 1.5T MRI. *Proceedings of the ISMRM 25th Annual Meeting*, April 2017, Honolulu, HI: pg. no. 4297.
- Lu, J., Grafendorfer, T., Vasanawala, S., Robb, F., Pauly, J., Scott, G. (2018). Antenna design for wireless clock syncing and Q-spoiling in MRI. *Proceedings of the ISMRM 26th Annual Meeting*, June 2018, Paris, France: pg. no. 0028.
- Ma, Y., Darnell, D., Zhang, H., Robb, F., Song, A.W., Truong, TK. (2018). Integrated parallel reception, excitation, and shimming (iPRES) breast coil array for simultaneous MR image acquisition and localized B_0 shimming. *Proceedings of the ISMRM 26th Annual Meeting*, June 2018, Paris, France: pg. no. 842.
- Majid, N., Hafiz, S., Arianto, S., Yuono, RY, Astuti, E., Prihandoko, B. (2017). Analysis of effective pulse current charging method for lithium-ion battery. *Journal of Physics: Conference Series*, 817(), 012008.
- McGee, K., Stormont, R., Lindsay, S., Taracilla, V., Savitskij, D., et al. (2018). Characterization and evaluation of a flexible MRI receive coil array for radiation therapy MR treatment planning using highly decoupled RF circuits. *Physics in Medicine & Biology*, 63(8), 08NT02.

- Mehmann, A., Varga M., Vogt, C., Port, A., Reber, J., Marjanovic J., Pruessmann K., Tröster G. (2019). On the bending and stretching of liquid metal receive coils for magnetic resonance imaging. *IEEE Transactions on Biomedical Engineering*, 66(6), 1542-48.
- Meshksar, A., Villablanca, J., Khan, R., Carmody, R., Coull, B., Nael, K. (2014). Role of EPI-FLAIR in patients with acute stroke: A comparative analysis with FLAIR. *American Journal of Neuroradiology*, 35(5), 878-83.
- Mochcovitch, M.D., Christophe, R., Garcia, R., Nardi, A. (2014). A systematic review of fMRI studies in generalized anxiety disorder: evaluating its neural and cognitive basis. *Journal of Affective Disorders*, 167(), 336-42.
- Moser, E., Laistler E., Schmitt F., Kontaxis G. (2017). Ultra-high field NMR and MRI – The role of magnet technology to increase sensitivity and specificity. *Frontiers in Physics*, 5:33.
- Niekerk, A., Berglund, J., Sprenger, T., Norbeck, O., Avventi, E., Ryden, H., Skare, S. (2022). Control of a wireless sensor using the pulse sequence for prospective motion correction in brain MRI. *Magnetic Resonance in Medicine*, 87(2), 1046-61.
- Nowogrodzki, A. (2018). The Strongest Scanners: Researchers are pushing non-invasive brain imaging to new limits. *Nature*, 563(), 24-26.
- O’Keefe, S., Kingsley, S. (2007). Tunability of liquid dielectric resonator antennas. *IEEE Antennas and Wireless Propagation Letters*, 6(), 533-36.
- Paloyelis, Y., Mehta, M.A., Kuntsi J. Asherson P. (2007). Functional magnetic resonance imaging in attention deficit hyperactivity disorder (ADHD): a systematic literature review. *Expert Review of Neurotherapeutics*, 7(10), 1337-56.
- Pruessmann, K., Weiger, M., Scheidegger, M., Boesinger, P. (1999). SENSE: sensitivity encoding for fast MRI. *Magnetic Resonance in Medicine*, 42(5), 952-62.
- Rajasekaran, S., Kanna, R., Shetty, A. (2006). Diffusion tensor imaging of the spinal cord and its clinical applications. *The Journal of Bone and Joint Surgery*, 94(8), 1024-31.
- Rios, N., Topfer, R., Foias, A., Guittonneau, A., Gilbert, K., Menon, R., Wald, L., Stockmann, J., Cohen-Adad, J. (2019) Integrated AC/DC coil and dipole Tx array for 7T MRI of the spinal cord. *Proceedings of the ISMRM 27th Annual Meeting*, May 2019, Montréal, QC: pg. no. 220.

Roemer, P., Edelstein, W., Hayes, C., Souza, S., Mueller, O. (1990). The NMR phased array. *Magnetic Resonance in Medicine*, 16(2), 192-225.

Schulz, J., Siegert, T., Reimer, E., Labadie, C., Maclaren, J., Herbst, M., Zaitsev, M., Turner, R. (2012). An embedded optical tracking system for motion-corrected magnetic resonance imaging at 7T. *Magnetic Resonance Materials in Physics, Biology and Medicine*, 25(6), 443-53.

Smith, K., Lury, K., Castillo, M., (2006). Imaging of spinal and spinal cord tumors. *Seminars in Roentgenology*, 41(4), 274-93.

Sodickson, D., Manning, W. (1997). Simultaneous acquisition of spatial harmonics (SMASH): fast imaging with radiofrequency coil arrays. *Magnetic Resonance in Medicine*, 38(4), 591-603.

Souza, C.P., Hamani, C., Souza C.O., Contreras, W., Ghilardi, M., Cury, R., Barbosa, E., Teixeira, M., Fonoff, E. (2017). Spinal cord stimulation improves gait in patients with Parkinson's disease previously treated with deep brain stimulation. *Movement Disorders*, 32(2), 278-82.

Stockmann, J., Witzel, T., Keil, B., Polimeni, J., Mareyam, A., LaPierre, C., Setsompop, K., Wald, L. (2016). A 32-channel combined RF and B₀ shim array for 3T brain imaging. *Magnetic Resonance in Medicine*, 75(1), 441-51.

Stockmann, J., Wald, L. (2018). In vivo B₀ field shimming methods for MRI at 7T. *NeuroImage*, 168(), 71-87.

Stormont, R. (2017). Reimagining flexible coil technology. *GE Healthcare. GE Signa Pulse*, May 2017, www.gesignapulse.com.

Thurnher, M., Bammer, R. (2006). Diffusion-weighted MR imaging (DWI) in spinal cord ischemia. *Diagnostic Neuroradiology*, 48(11), 795-801.

Topfer, R., Starewicz, P., Lo, K., Metzemaekers, K., Jette, D., Hetherington, H., Stikov, N., Cohen-Adad, J. (2016). A 24-channel shim array for the human spinal cord: Design, evaluation, and application. *Magnetic Resonance in Medicine*, 76(5), 1604-11.

Topfer, R., Foias, A., Rios, N., Chauffray, A., Germain, G., Arango, N., Wald, L., Stockmann, J., Cohen-Adad, J. (2018a). Integrated $\Delta B_0/R_x$ coil array for improved spinal cord imaging at 3T. *Proceedings of the ISMRM 26th Annual Meeting*, June 2018, Paris, France: pg. no. 834.

Topfer, R., Foias, A., Stikov, N., Cohen-Adad, J. (2018b). Real-time correction of respiration-induced distortions in the human spinal cord using a 24-channel shim array. *Magnetic Resonance in Medicine*, 80(3), 935-46.

Topfer, R., Rios, N., Foias, A., Arango, N., Wald, L., Stockmann, J., Cohen-Adad, J. (2019). Real-time shimming in the cervical spinal cord using an 8-channel AC/DC array and a capacitive respiratory sensor. *Proceedings of the ISMRM 27th Annual Meeting*, May 2019, Montréal, QC: pg. no. 925.

Truong, TK., Darnell, D., Song, A.W. (2014). Integrated RF/shim coil array for parallel reception and localized B₀ shimming in the human brain. *NeuroImage*, 103(), 235-40.

Vassos, C., Robb, F., Vasanawala, S., Pauly, J., Scott, G. (2019). Characterization of in-bore 802.11ac Wi-Fi performance. *Proceedings of the ISMRM 27th Annual Meeting*, May 2019, Montréal, QC: pg. no. 1543.

Venkateswaran, M., Kurpad, K., Brown, J., Fain, S., van der Weide, D. (2020). Wireless power harvesting during MRI. *Annual International Conference of the IEEE Engineering in Medicine and Biology Society*, July 2020: pg. no. 1469-72.

Walter, S., Perl, R., Notohamiprodjo, M., Nikolaou, K., Gatidis, S. (2019). Improvement of EPI-based DWI of the head/neck region using additional local shim coils at 3 Tesla. *Proceedings of the ISMRM 27th Annual Meeting*, May 2019, Montréal, QC: pg. no. 3521.

Willey, D., Bresticker, J., Truong, TK., Song, A., Madore, B., Darnell, D. (2020). Integrated RF/wireless coil and ultrasound-based sensors to enable wireless physiological motion monitoring in MRI. *Proceedings of the ISMRM 28th Annual Meeting*, August 2020, Virtual: pg. no. 1282.

Willey, D., Darnell, D., Song, A.W., Truong TK. (2021). Application of an integrated radio-frequency/shim coil technology for signal recovery in fMRI. *Magnetic Resonance in Medicine*, 86: 3067-81.

Xiao, L., Pan, H., Zhenfei, S. (2019). The antenna measurements using the three-antenna extrapolation range. *International Symposium on Antennas and Propagation (ISAP)*, pg. no. 1-3.

Zaitsev, M., Dold, C., Sakas, G., Speck, O. (2006). Magnetic resonance imaging of freely moving objects: prospective real-time motion correction using an external optical motion tracking system. *Neuroimage*, 31(3), 1038-50.

Zhang, B., Sodickson, D., Cloos, M. (2018). A high-impedance detector-array glove for magnetic resonance imaging of the hand. *Nature Biomedical Engineering*, 2(), 570-77.